# Modified horn-type antennas for SKA RFI Monitoring

by

Jackline C. Koech

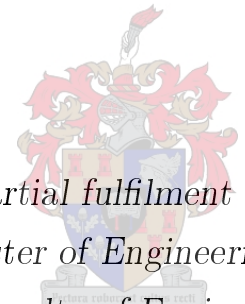

*Thesis presented in partial fulfilment of the requirements for the degree of Master of Engineering (Electrical and Electronic) in the Faculty of Engineering at Stellenbosch University*

Supervisor: Dr. P. Gideon Wiid

Co-supervisor: Prof. D.I.L de Villiers

December 2019

The financial assistance of the Square Kilometre Array (SKA) towards this research is hereby acknowledged. Opinions expressed and conclusions arrived at, are those of the author and are not necessarily to be attributed to SKA.

# Declaration

I have read and understand the Stellenbosch University Policy on Plagiarism and the definitions of plagiarism and self-plagiarism contained in the Policy [Plagiarism: The use of the ideas or material of others without acknowledgment, or the re-use of one's own previously evaluated or published material without acknowledgment or indication thereof (self-plagiarism or text-recycling)].

I also understand that direct translations are plagiarism, unless accompanied by an appropriate acknowledgment of the source. I also know that verbatim copy that has not been explicitly indicated as such, is plagiarism.

I know that plagiarism is a punishable offence and may be referred to the University's Central Disciplinary Committee (CDC) who has the authority to expel me for such an offense.

I know that plagiarism is harmful for the academic environment and that it has a negative impact on any profession.

Accordingly all quotations and contributions from any source whatsoever (including the Internet) have been cited fully (acknowledged); further, all verbatim copies have been expressly indicated as such (e.g. through quotation marks) and the sources are cited fully.

I declare that, except where a source has been cited, the work contained in this assignment is my own work and that I have not previously (in its entirety or in part) submitted it for grading in this module/assignment or another module/assignment.

Jackline Koech Date: September 2019

# Abstract


## Modified horn-type antennas for SKA RFI Monitoring

J. Koech

*Department of Electrical and Eletronic Engineering,*
*University of Stellenbosch,*
*Private Bag X1, Matieland 7602, South Africa.*

Thesis: MEng (EE)

December 2019

Maintaining a site free of radio frequency interference (RFI) is an essential aspect in the performance of the Square Kilometre Array (SKA) radio telescope. Regular on-site RFI measurements have to be done to identify unwanted sources of RFI and to verify RFI-compliance of equipment within the operating frequencies of the telescope. To perform these measurements requires hyperband directional antennas that cover all the frequencies of the first phase of SKA-MID are required, ideally 200 MHz - 4 GHz, a bandwidth ratio of 20:1. In addition, they need to be mechanically robust and portable, since they often need to be mounted at a height for testing.

For this application, we investigate three types of modified horn antennas: a double-ridged guide-horn (DRGH), a transverse electromagnetic (TEM) horn, and a Valentine antenna. These antennas are chosen because of their bandwidth and gain. A wideband coaxial to parallel-plate transition is also designed for feeding the Valentine and TEM horn antennas because of their symmetry. The three antennas are modelled, simulated in Dassault Systémes' CST Studio Suite and prototyped to analyse the complexity of construction and to compare measurement results with those simulated. The measured return loss, radiation patterns and gain results are a good replication of the simulated results. A surrogate-based optimization (SBO) scheme that uses Kriging model and Expected Improvement (EI) was used to optimize the antennas for return loss. Designing these structures using the normal supervised parametric sweeps is impractical due to the lengthy simulation times involved because of the wide bandwidth and large geometry. An SBO only requires a few full wave simulations of the structure to support the Kriging model, while each new simulation requested by the iterative process is selected at a

position in the design space where the optimum solution is most likely, given the current estimation of the response. Using this technique, the return loss of the three antennas has been optimized and bandwidth ratio improved from 10 to 16.

An analysis of the three antennas is done by comparing the fabrication process, the size, robustness and weight of the antennas, the ease of characterization and the performance of the antenna. Based on this analysis, the DRGH is recommended for RFI testing at the SKA radio telescope site.

# Uittreksel


## Gewysigde horing-tipe antennas vir SKA RFS Monitering

*("Modified horn-type antennas for SKA RFI Monitoring")*

J. Koech

*Departement Elektriese en Elektroniese Ingenieurswese,*
*Universiteit van Stellenbosch,*
*Privaatsak X1, Matieland 7602, Suid Afrika.*

Tesis: MIng (Elek)

Desember 2019

Die instandhouding van 'n terrein vry van radiofrekwensie-steurings (RFS) is 'n wesenlike aspek in die uitvoering van die Vierkante Kilometer Reeks (SKA). Gereëlde RFS-metings moet op die terrein gedoen word om ongewenste bronne van RFS te identifiseer en om die RFS-nakoming van toerusting binne die gebruiksfrekwensies van die teleskoop te verifieer. Om hierdie metings uit te voer, verg dit hiperband gerigte antennas wat al die frekwensies van die eerste fase van SKA-MID dek, verkieslik 200 MHz - 4 GHz, 'n bandwydteverhouding van 20:1. Daarbenewens moet hulle meganies robuust en draagbaar wees, aangesien hulle dikwels op 'n hoogte gemonteer moet word vir toetse.

Vir hierdie toepassing ondersoek ons drie soorte aangepaste horingantennas: 'n dubbelrygidshoring (DRGH), 'n transversale elektromagnetiese (TEM) horing en 'n Valentine-antenna. Hierdie antennas word gekies as gevolg van hul bandwydte en wins. 'n Breëband koaksiale-na-parallelplaatoorgang is ook ontwerp vir die voer van die Valentine- en TEM-horingantennas vanweë hul simmetrie. Die drie antennas is gemodelleer, gesimuleer in Dassault Systemes CST Studio Suite en vervaardig om die kompleksiteit van konstruksie te ontleed en om die meetresultate met die gesimuleerde te vergelyk. Die gemete terugkeerverlies, stralingspatrone en aanwinsresultate is 'n goeie weerspieëling van die gesimuleerde resultate. 'n Surrogaat-gebaseerde optimisering (SBO)-skema met Kriging-model en "Expected Improvement"(EI), is gebruik om die antennas se terugkeerverlies te optimiseer. Die ontwerp van hierdie strukture met behulp van die normaal bestuurde parametriese veeg is onprakties vanweë die lang simulasietye wat betrokke is as gevolg van die breë bandwydte en groot geometrie. 'n SBO benodig slegs 'n paar volledige-golf simu-

lasies van die struktuur om die Kriging-model te ondersteun, terwyl elke nuwe simulasie wat deur die iteratiewe proses gevra word, gekies word op 'n plek in die ontwerpruimte waar die optimale oplossing waarskynlik is, gegewe die huidige beraming van die reaksie. Met behulp van hierdie tegniek is die terugkeerverlies van die drie antennas geoptimiseer en het die bandwydteverhouding van 10 tot 16 verbeter.

'n Analise van die drie antennas word gedoen deur die vervaardigings-proses, die grootte, robuustheid en gewig van die antennas, die gemak van karakterisering en die werkverrigting van die antenna te vergelyk. Op grond van hierdie ontleding word die DRGH aanbeveel vir RFS-toetsing op die SKA-radioteleskoopterrein.

# Acknowledgements

I would like to express my sincere gratitude first to my supervisors: Dr. Gideon Wiid and Prof. Dirk de Villiers for their advice, brilliant ideas, support and encouragement throughout this program. I wouldn't have asked for better supervisors!

To Mr. Wessel Croukamp and his team who helped build all the antennas with great detail, otherwise this project wouldn't have been possible.

Thirdly, I would like to thank Anneke Bester who was of great help in performing the antenna measurements with several repetitions. Thank you for your patience!

I would also like to thank Dr. Brandt Klopper and Fahmi Mokhupuki who helped a great deal towards understanding how to use the optimization toolbox.

Many thanks to the EMRIN group in room E212: Stanley, Chris, Millicent and Jérémie for their help in various ways throughout this project.

Finally, I would like to acknowledge the financial assistance of Square Kilometre Array (SKA) and National Research Foundation (NRF). This research was supported by the South African Radio Astronomy Observatory, which is a facility of the National Research Foundation, an agency of the Department of Science and Technology.

# Dedications

*To my parents, Emily and William Koech: Thank you for believing in me.*
*To my husband Wesley: Thank you for your unwavering support.*
*To my daughters, Cheptoo and Cherop: There are endless possibilities!*

# Contents

# List of Figures

# List of Tables

# Nomenclature

### Abbreviations

| | |
|---|---|
| TE | Transverse Electric |
| TM | Transverse Magnetic |
| RF | Radio Frequency |
| SKA | Square Kilometre Array |
| RFI | Radio Frequency Interference |
| TEM | Transverse Electromagnetic |
| CST | Computer Simulation Technology |
| DRGH | Double Ridged Guide Horn |
| E-Plane | Electric Plane |
| H-Plane | Magnetic Plane |
| SBO | Surrogate-Based Optimization |
| EI | Expected Improvement |

# Chapter 1

# Introduction

## 1.1 About SKA

The Square Kilometre Array (SKA) [1] is a large telescope project with antenna arrays planned to cover a total collecting area of one kilometre square (1 $km^2$). This collection of dish antennas will spread over long distances, unlike a traditional telescope. The sky will be monitored in very high detail and at hundreds of times faster than any existing telescopes. This project will shed a lot of light into Astronomy and Physics and will help in unravelling some mysteries about the universe.

The telescope arrays are being built in two phases, as part of the first phase in South Africa and Australia, and expanded to some select African countries and other parts of Australia in the second phase. As part of the mid-frequency component of the first phase of the SKA telescope project, the MeerKAT [2] is being built in Carnarvon, South Africa, as a precursor to the SKA telescope. To date, 64 dishes have been installed with planned addition of 133 more dish antennas later.

## 1.2 Motivation and Technical Requirements

Monitoring levels of on-site Radio Frequency Interference (RFI) is important in the performance of the SKA telescope. RFI measurements are done to ensure that all equipment on-site comply with RFI level guidelines, as well as to detect RFI due to off-site sources. An antenna is required to monitor these RFI levels. This antenna not only needs to be mechanically robust (can be mounted high up) and portable, but it also needs to be directional in order to approximate the direction of unwanted RFI sources. In order to cover all the mid frequencies of the MeerKAT, this antenna should have a wide bandwidth of about 20:1 (ideally in the frequency range of 200 MHz to 4 GHz). A gain greater than 12 dBi at mid-frequency will be desirable as well as matching to a 50 $\Omega$ system.

Directional wideband antennas, which are often horn antennas, are commonly used

in RFI testing. Waveguide horn antennas are often popular due to their relatively large bandwidth ratios, robustness and directivity. A conventional horn antenna, however, is often limited in bandwidth. Three types of modified horn antennas are investigated: a Double-Ridged Guide Horn (DRGH) [3], a Transverse Electromagnetic (TEM) horn [4] and Valentine [5] antennas which have improved bandwidth.

## 1.3 Overview

In order to design an antenna for the desired RFI testing, an in-depth literature review was done and is presented in Chapter 2 where an analysis of regular horn antennas and the three above-mentioned modified horn antennas is done. Comparable sizes of these three antennas are then designed, modelled and simulated in Dassault Systémes' CST Studio Suite [6] to compare the return loss and gain performances as discussed in Chapter 3. The three antennas are then constructed in order to determine fabrication complexity, as outlined in Chapter 4. The measured and simulated results for the fabricated antennas are presented and discussed in Chapter 5. Given the satisfactory preliminary measured results of the fabricated antennas compared to the simulated results, a full numerical optimization of the antenna models using Surrogate-Based Optimization (SBO), is carried out in Chapter 6 in order to improve the bandwidth of the antennas. A conclusion on the analysis of the three antennas is presented in Chapter 8 where a recommendation of an antenna for this application is provided. Finally, Chapter 7 presents recommendations for future work to be done to extend this project.

# Chapter 2

# Literature Review

## 2.1 Horn Antenna

Directional wideband antennas, mostly horn antennas, are often used in RFI testing. A horn antenna is a type of an aperture antenna. Particularly waveguide horn antennas are mostly used because of their directivity, robustness, and relatively large bandwidth ratio. For accurate gain measurements, most antennas are also often compared to the standard gain horn antenna, typically a pyramidal antenna [7].

Horn antennas come in different shapes, with a pyramidal horn antenna being a historically popular type due to the ease of approximate analytical analysis [8]. A pyramidal horn antenna is simply a flared out rectangular waveguide and is therefore easy to fabricate. Figure 2.1 shows a pyramidal horn antenna with its H-plane and E-plane cuts shown in Figure 2.2. The labelled dimensions in these figures can be used to design a pyramidal horn antenna for specific gain using equations presented in [7].

The flare angle of the pyramidal horn antenna, that is, the ratio of aperture dimensions to axial length of the antenna, determines the directivity of the antenna as well the aperture distribution [9]. For a uniform aperture distribution, the flare angle should be kept at a minimum; however, it is also important to have the horn antenna as short as possible to keep the size of the antenna reasonable. An optimum compromise between size and performance should be arrived at.

## 2.2 Double-Ridged Guide Horn Antenna

A conventional horn antenna has limited bandwidth. A double-ridged guide horn (DRGH) antenna is a modified pyramidal horn antenna that has ridges on two opposite walls, in both the waveguide and the horn(flared) parts of the antenna. The ridges in the DRGH reduce the impedance in the waveguide and improves the bandwidth ratio of the antenna by lowering the cutoff frequency of the dominant mode ($TE_{10}$) and increasing the cutoff

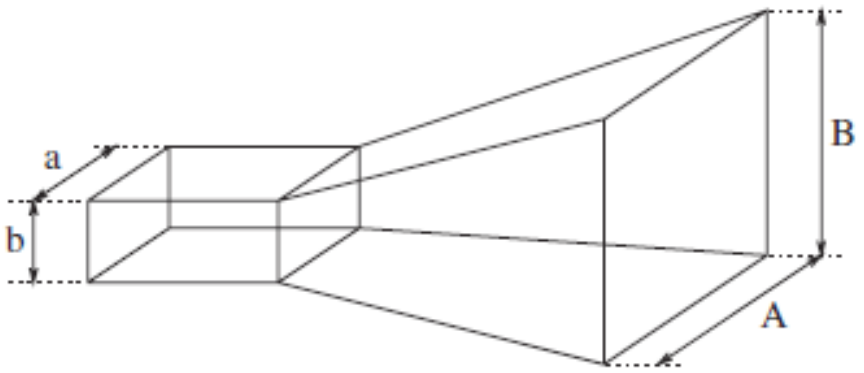


Figure 2.1: Diagram of pyramidal horn antenna showing waveguide and horn aperture dimensions [7]

.

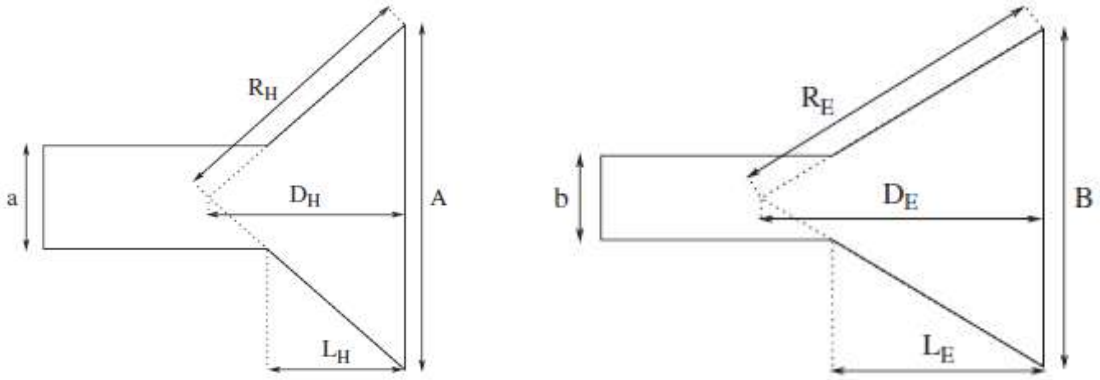


Figure 2.2: H-plane (left) and E-plane (right) cut views of the pyramidal horn antenna of Figure 2.1 [7].

frequency of the next higher mode ($TE_{11}$) [10, 11].

### 2.2.1 Description of Configuration

A DRGH antenna consists of three main parts; a feed, a double-ridged waveguide and a ridged flared section (radiating horn).

1. **Feed**

   The antenna feed is a coaxial cable terminated in a connector. The inner conductor of the coaxial cable goes through a hole on the upper ridge and connects to the bottom ridge [12].

   The characteristic impedance of a coaxial cable is defined by [13]

$$Z = \frac{60}{\sqrt{\epsilon_r}} \ln \frac{R_o}{r_i}, \tag{2.1}$$

   where $\epsilon_r$ is the relative permittivity of the dielectric material between the conductors, $R_o$ is the radius of the outer coaxial conductor and $r_i$ is the radius of the inner coaxial conductor. The dimensions of coaxial feed, that is, the inner and

outer radii can, therefore, be determined given the desired impedance. For this project, we need to match the antenna to a 50 Ω system.

The feed line should also be well designed so that the Transverse Electromagnetic (TEM) mode in the coaxial cable is transformed effectively to the Transverse Electric (TE) mode in the waveguide with minimum reflections.

2. **Waveguide**

Figure 2.3 shows a cross-sectional view of the waveguide part of the double-ridged guide horn antenna, that is, a waveguide with two ridges on the top and bottom walls.

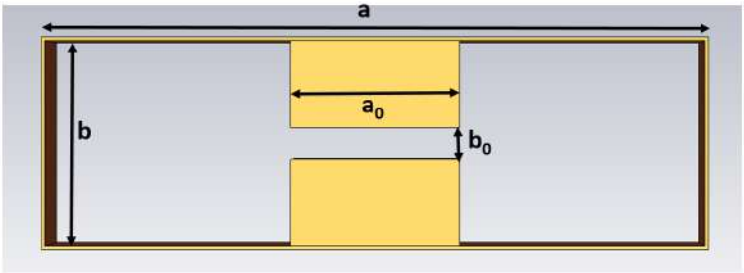


Figure 2.3: Cross-sectional view of the double-ridged waveguide with a width, $a$, height $b$ , width of ridges $a_0$ and separation distance between ridges, $b_0$.

The separation distance between the ridges, $b_0$, and the width of the ridges, $a_0$, of the ridged waveguide can be varied to control the impedance in the waveguide as well as the bandwidth of an antenna.

3. **Ridge Profile**

Similar to the waveguide part of the antenna, dual ridges are also introduced on the horn (flared) part of the antenna. The ridge profile in the flared part is designed to vary the impedance from 50 Ω at the coaxial feed to the free space impedance at the aperture of the antenna. At the horn aperture, the impedance is that of free space (377 Ω). The wave impedance of the ridged waveguide must be matched to that of free space using a matching section, for this case, the ridges. The matching section can be linear, binomial, sinusoidal or exponential as discussed in [13].

In [14], different geometries of the tapered ridges are analysed including exponential, sinusoidal, linear and quadratic. The exponential ridge profile is shown to give a better radiation pattern as well as a better return loss. The impedance of an exponentially tapered matching section is given by [13]

$$Z(z) = Z(0)\exp(kz), (0 \leq z \leq L) \tag{2.2}$$

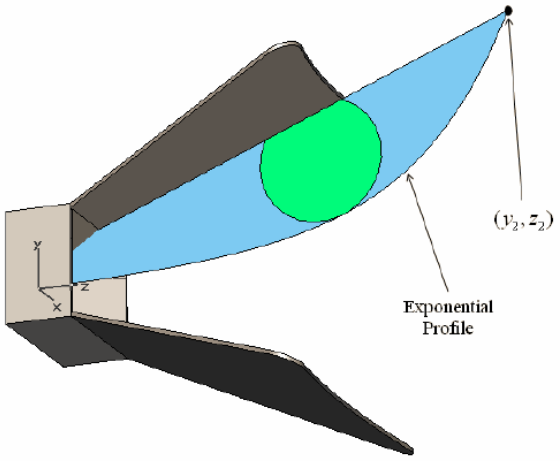


Figure 2.4: An improved exponential ridge profile for the DRGH antenna [16]

where $z$ is the distance from the waveguide aperture, $L$ is the axial length (distance between waveguide aperture and the horn aperture) of the antenna and $Z(0)$ is the wave impedance of the waveguide (impedance at $z = 0$). $Z(z)$ is the impedance at point $z$, and $k$ is defined as

$$k = \frac{1}{L} \ln \left( \frac{Z(L)}{Z(0)} \right) \tag{2.3}$$

where $Z(L)$ is the impedance at the horn aperture, that is, the free space impedance. According to [15], the ridged profile can be designed by dividing the axial length of the horn part of the antenna into a number of sections, N. Each section is then modelled as a ridged waveguide with a varying ridge height. The outer dimensions of each waveguide are calculated from the antenna horn flare parameters. The height of the ridge in each of these small waveguides is varied to achieve the required wave impedance at each section calculated using (2.2). When the optimization of each section is completed, the N ridged waveguides can then be joined together to form the complete double-ridged guide horn antenna.

It has been shown in [16] that conventional exponential ridges, open too fast and do not provide proper impedance matching. A modified ridge profile with a linear, exponential and a circular part is suggested given by (2.4), where the impedance profile is described by

$$z(y) = a \exp(by) + c, (0 \leq y \leq L), \tag{2.4}$$

where $b$ is an independent variable and $a$ and $c$ are determined by initial and end points where the endpoint is not necessarily a point on the antenna horn. This modified ridge profile is illustrated in Figure 2.4.

A linear part, with a gradient of 0.02, superimposed on an exponential ridge profile has also been proved to lower the VSWR at lower frequencies [17, 18, 19]. The

ridge profile can be defined by (2.5) [17]

$$z(y) = 0.02z + z(0)\exp(kz), (0 \leq z \leq L), \tag{2.5}$$

where the parameters are defined above in (2.2).

### 2.2.2 Improving DRGH Performance

In addition to designing the ridge profile in the flared part of the antenna to minimize the reflection coefficient, a back cavity can be introduced at the end of the ridged waveguide to reduce back reflections [20]. Wedges can alternatively be introduced into the waveguide to create a cavity [12] resulting in a similar effect. The dimensions of the back cavity are appropriately chosen as a quarter wavelength at the centre frequency to transform the short circuit at the end of the cavity to an open circuit (infinite impedance) at the coaxial probe position [12]. In addition to the dimensions of the back cavity, the shape has also been proved to affect the return loss of the coaxial to waveguide transition where a pyramidal back cavity offered the best return loss [3]. Moreover, the distance between the waveguide ridges and the location of the coaxial feed along the ridges can be optimized to improve the reflection coefficient.

In a patent [21], a technique of improving VSWR and radiation pattern at low frequencies loads the antenna cavity (back end of the waveguide) with lossy material, ECCOSORB®(0.8-18 GHz). This, however, reduces the antenna gain and radiation efficiency where the radiation efficiency reduced by 5-20 % [17].

The typical gain of double-ridged waveguide horn antennas operating in the range 200 MHz to 2 GHz is presented in [22] as varying from 6-10 dBi as shown in Figure 2.5. However, a sudden drop in gain after 1.9 GHz is observed which is attributed to the main radiation beam splitting at the high frequency due to the excitation of higher order modes in the feed cavity. To resolve this problem, reflective material was introduced in the cavity of the antenna which was observed to increase the gain by 6 dB at 2 GHz [22]. In [3], the feed position of the coaxial probe along the ridges was also shown to affect the radiation pattern of an 8-18 GHz antenna at the high frequencies.

Another technique that has been investigated to reduce the distortion of radiation patterns at high frequencies is the use of a dielectric lens at the horn aperture as discussed in [23]. A spherical shaped dielectric lens at the aperture is shown to improve the gain of a double-ridged horn antenna by 4.5-6 dB in the 20-40 GHz frequency range.

Besides confining the beam-width of the H-plane radiation pattern, the H-plane flares of a DRGH are negligible at high frequencies because most of the electrical energy is concentrated on the ridges [17, 24]. Walls in a double-ridged guide horn antenna can be replaced with metal rods that act as a wall for low frequencies below 4 GHz [17, 25]. These metal rods, however, have a negative effect on the radiation pattern and [17]

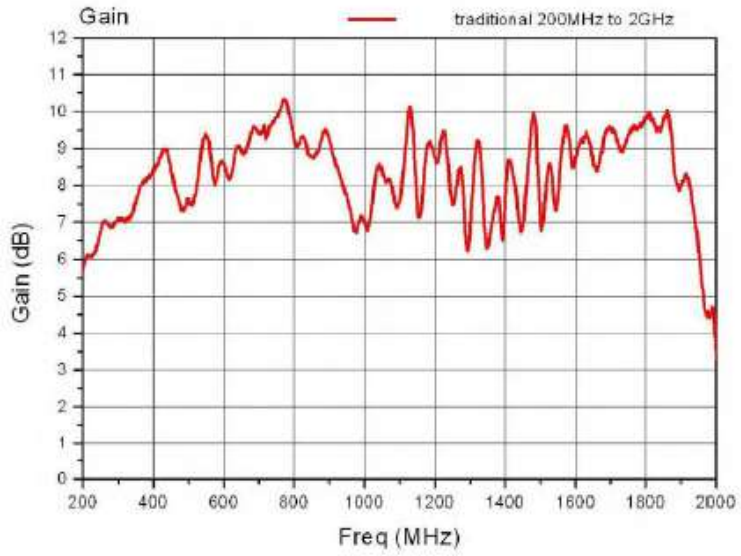


Figure 2.5: Typical gain of a traditional 200-2000 MHz DRGH antenna [22]

proposes removing them to improve the radiation pattern above 12 GHz. A modified DRGH antenna, presented in [17] (Figure 2.6) where the metal rods are removed and the ridges at the aperture rounded with circular profile of radius of a quarter wavelength at the lowest frequency, was shown to improve the radiation pattern at the high frequencies and the gain at low frequencies. The replacement of the H-flare walls with dielectric material with some metal straps which act like a plane reflector only at low frequencies was investigated in [16] but it was also proved to deteriorate the radiation pattern at high frequencies. In this investigation of a 1-18 GHz DRGH antenna, the H-flares helped to raise the hgain at low frequencies but deteriorated the radiation pattern at high frequency. The E-flares were also rounded to reduce diffraction after the removal of the H-flares.

It has been noted that most of the methods designed to eliminate high-frequency problems, such as radiation pattern, deteriorate the performance at low frequency and vice versa. A new design in [26] for the 1-18 GHz DRGH antenna aims to improve gain and VSWR at low frequencies (1-3 GHz) without affecting the radiation pattern at high frequencies. Instead of using the traditional ridge profile given by Kerr [18], a cubic Bezier curve is used to change the ridge profile near the aperture of the horn antenna. Metallic grid sidewalls are also used to restore the low-frequency performance that occurs when H flares are removed. Additionally, the coaxial feed and the coaxial to ridged waveguide transition was redesigned to have minimum gaps which cause higher modes to propagate, thus improving the radiation pattern deterioration that occurs at high frequency.

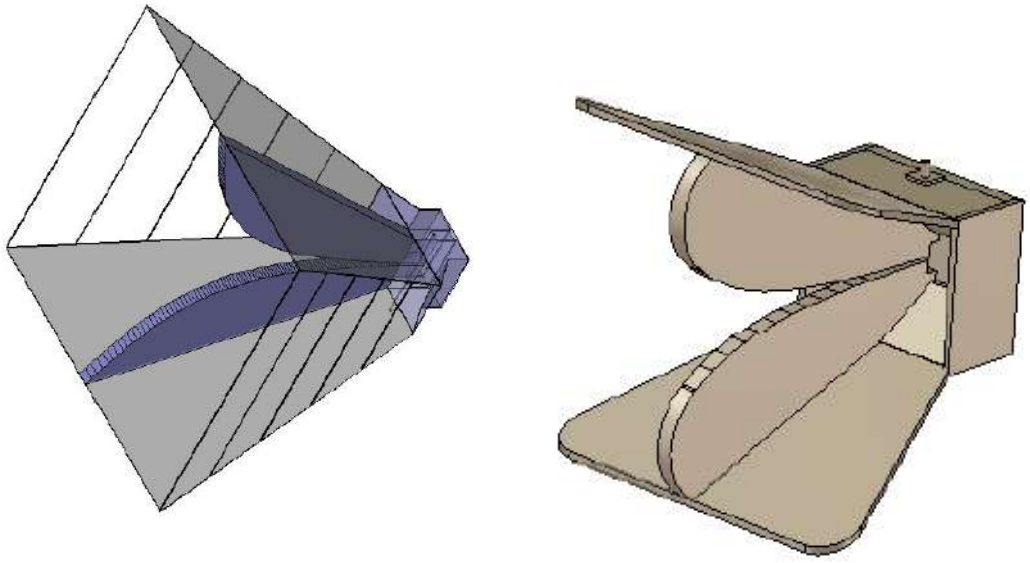

Figure 2.6: (Left) DRGH) antenna [27] with metal rod on the H-plane flares to improve gain at low frequency and (right) improved DRGH design without metal rods on the H-plane flares, with rounded E-plane flare edges and circular ridge ends to improve radiation patterns at high frequency [17].

## 2.3 TEM Horn Antenna

The Transverse ElectroMagnetic (TEM) horn is a type of a travelling wave antenna with two metallic plates. TEM horns are not only easy to construct, but have all the desired features of being unidirectional, having no dispersion and of being wideband. In its simplest form, a TEM horn is made with two linearly tapering plates as shown in Figure 2.7. These plates can also be tapered exponentially or following other profiles. In an exponentially-tapered TEM horn, the width of the plates increases towards the aperture, and the separation distance between the plates also varies according to an exponential profile. An exponentially-tapered TEM horn despite being more complex to construct, significantly reduces reflections and has a wider bandwidth than the linearly tapered TEM horn [4]. Harima [28], computationally analyses four different types of tapers for a TEM horn antenna, namely exponential, triangular, Hecken and Klopfenstein. The highest gain was achieved with an exponentially tapering TEM horn antenna.

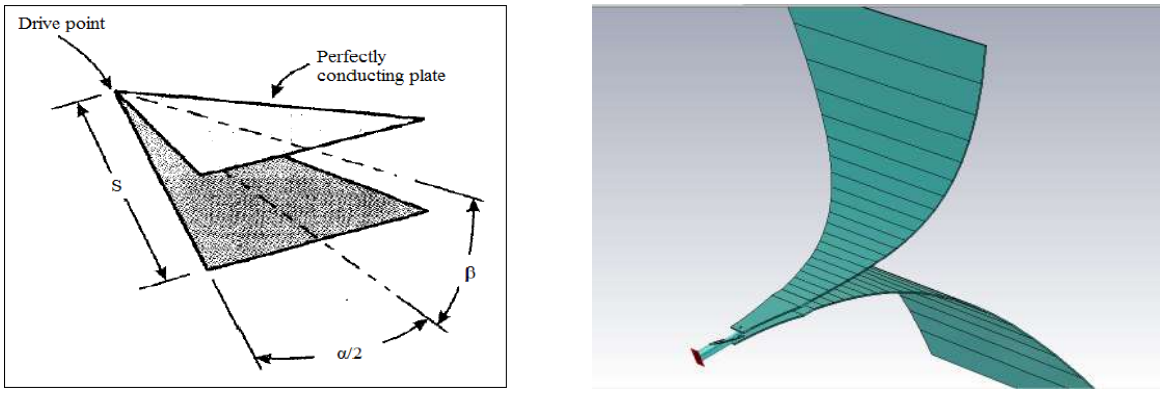


Figure 2.7: Linearly tapering TEM horn antenna (left )[29] and an exponentially tapering TEM horn antenna (right).

Various attempts have been made to improve the performance of the TEM horn antennas. Resistive loading has been used to improve bandwidth but at the expense of efficiency [30]. TEM horns performing at very high frequencies have also been inhibited by the fluctuation of the main lobe of the radiation pattern. In [3] the radiation pattern is improved by trimming edges of the aperture. An arc-shaped cut is made to the end of the exponentially tapered plates to improve radiation patterns at high frequencies [3] as shown in Figure 2.8. This has also been employed to enhance gain at high frequencies in [28].

To further reduce reflections that occur due to the edges of the exponential TEM, elliptical cylinders with rounded corners (Figure 2.8) can be introduced at the edges as discussed in [31]. Ameri, Kompa and Bangert in [32], propose a technique that can greatly reduce the dimensions of a TEM antenna, for example, the height by up to 52%. The antenna is folded cylindrically at the aperture as shown in Figure 2.8. This, however, was observed to reduce the gain of the antenna.

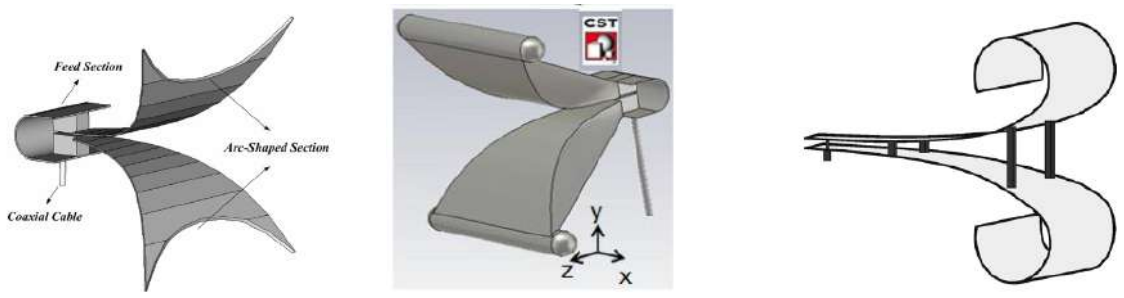


Figure 2.8: (Left) Arc-trimmed TEM horn antenna to improve radiation patterns [3], (middle) TEM with cylindrical edges and spherical corners to reduce reflections [31] and (right) TEM horn antenna with folded edges to reduce antenna size [32].

Because TEM horns are often fed from coaxial lines, a balun (balanced to unbalanced) is required. The balun serves to provide a match between the balanced TEM line (TEM horn plates) to the unbalanced coaxial line. An exponentially tapered TEM horn with a

microstrip balun is designed and manufactured in [4]. The microstrip balun improves the VSWR performance of the TEM horn [4], but the balun is as long as the antenna itself, which doubles the length of the antenna. An alternative balun is therefore investigated for feeding the TEM as discussed in Section 2.5.

## 2.4 Valentine Antenna

The Valentine antenna is a relatively new type of antenna. It is a modified TEM horn with a profile similar to that of a Vivaldi where two metallic strips spread out symmetrically following an exponential profile as shown in Figure 2.9 [33]. The strips are rounded at the edges to reduce current reflections. Similar to the TEM horn antenna, the Valentine antenna is also a type of a travelling-wave antenna. This means that the different frequency components of a signal are radiated at different distances along the antenna. Specific frequency radiations happens at the position along the antenna where the separation distance between the plates is equal to half the wavelength at that frequency [34]. The high-frequency components are therefore radiated first at the point of lower separation distance of the plates while the low-frequency components are radiated further towards the aperture of the antenna. Any un-radiated signals travel back to the feed along the rounded ends of the antenna. The flow of currents along the Valentine antenna are shown in Figure 2.10.

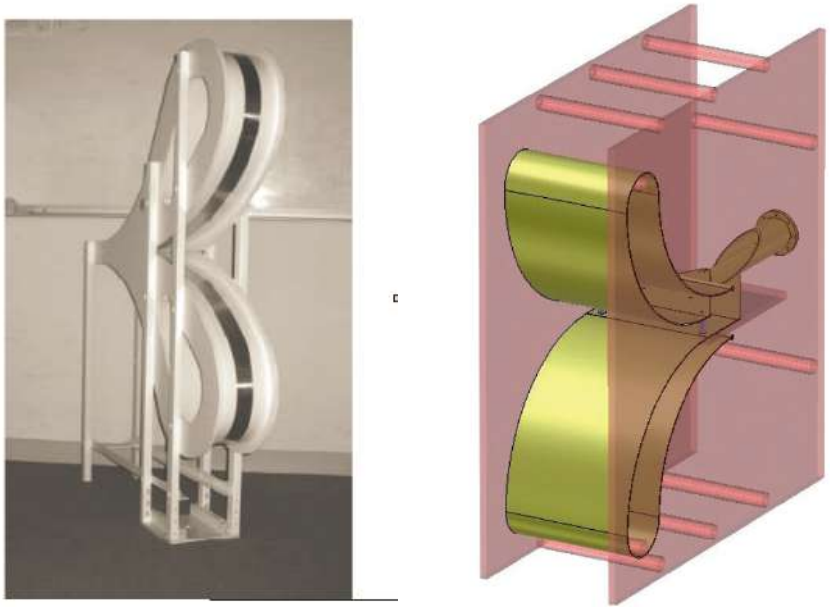

Figure 2.9: (Left) Valentine antenna with rounded aperture [5] and (right) Valentine antenna with narrower rounded edges[34].

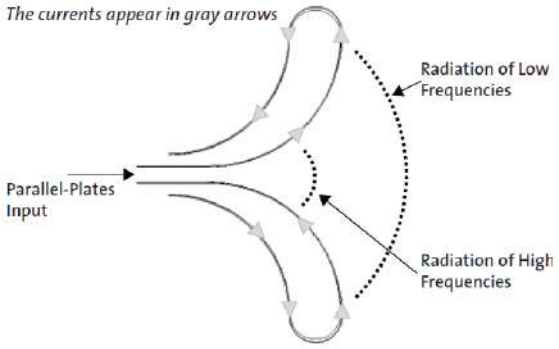


Figure 2.10: Illustration of current-flow in a Valentine antenna [34]

A few Valentine antenna designs are discussed in literature. In [5], a Valentine antenna operating from 300 MHz to 3 GHz has a largest dimension of 111cm as shown in Figure 2.9. Another modified version is discussed in [34] as shown in Figure 2.9. Although dimensions are not presented, this would potentially be a more compact design because the distance between the two plates is less towards the aperture, unlike the rounded separation distance in [5]. This antenna works from 0.3-5 GHz and has a directivity ranging from 9 dBi at 0.5 GHz to 22 dBi at 5 GHz. An even more compact Valentine antenna made out of a metal-coated polyester fabric is presented in [33]. This antenna works from 250 MHz to 2 GHz with an axial gain of 6 dBi to 12 dBi in the 0.3-5 GHz frequency range, is collapsible and can be folded.

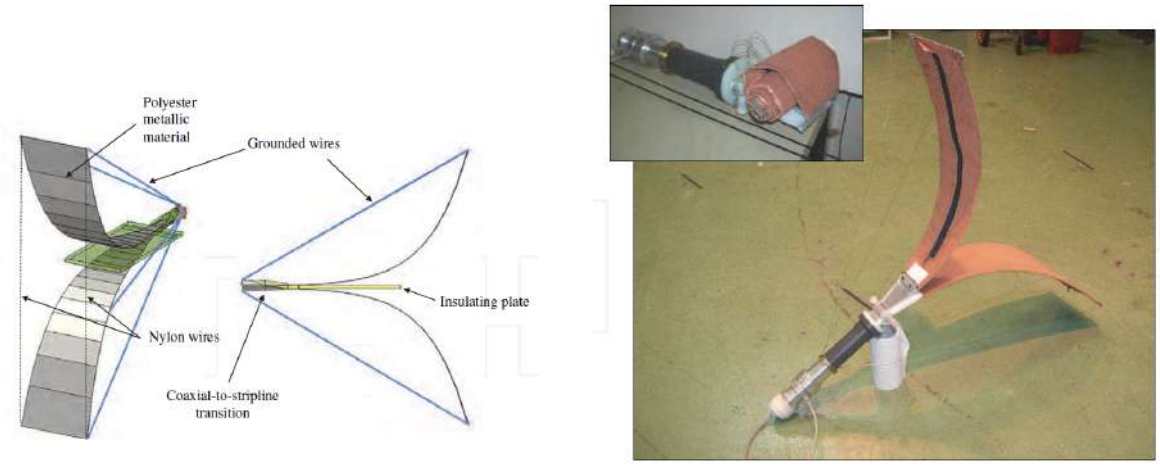


Figure 2.11: A foldable Valentine antenna design [33]

## 2.5 Coaxial to Parallel-plate Transition

The three antennas that are investigated in this thesis have symmetric structures. They, therefore, need a symmetric feeding mechanism. It is an industry norm that antennas are

fed via a coaxial cable and connector which do not provide a symmetric/balanced signal. If a balun is not used, this can lead to distorted radiation patterns due to unbalanced currents on each of the antenna plates. A balun is needed to provide a transition between the TEM mode in a coaxial feed to that of the parallel plates of the TEM horn antenna or the Valentine antenna. Designing a balun can, however, be an equally challenging task as designing the antenna itself.

A balun (balanced to unbalanced transition) design, was initially done by Duncan and Minerva [35] in 1960 where they designed a transition from the unbalanced coaxial line to a two conductor open line (balanced). In [36] and [37] a microstrip balun is used to feed a TEM horn antenna, however, the length of the microstrip balun is 0.478 $\lambda$, about the same length as the antenna itself, making the antenna unnecessarily bulky. In [4], with a 45 cm microstrip balun, a total length of 95 cm antenna is presented. In [38] and [31] a double-ridged waveguide with an elliptical cavity at the end is used as a transition to feed a TEM horn antenna. The elliptical cavity is meant to direct energy towards the front of the antenna.

Another interesting transition, known as a Tulipe transition is presented in [33] as shown in Figure 2.12. The outer conductor of the coaxial cable is trimmed at an angle and eventually into a rectangular plate. The inner conductor is slowly flattened from circular to elliptical and then into to a rectangular shaped flat plate. This Tulipe transition is used as a feed for a Valentine antenna.

A more compact balun is presented in [34] where a coaxial connector transitions into a parallel plate by trimming the outer coaxial conductor at an angle while the inner conductor gradually increases in diameter. The ends of the inner conductor and the trimmed outer conductor are then connected via triangular sections to the parallel plate section as shown in Figure 2.12. A non-standard air filled coaxial connector is used to connect to the transition, with an inner diameter of 7 mm and hence an outer diameter of 1.61 cm, calculated by (2.1), ensuring sufficient distance of separation between the plates of the parallel-plate section of the antenna. This transition section was supported using Plexiglass.

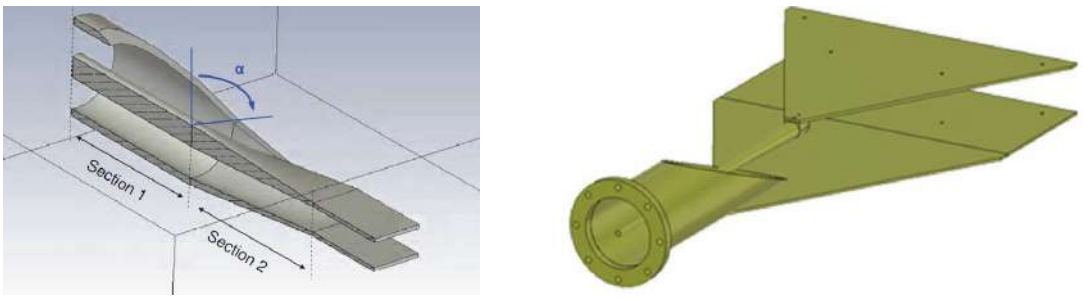


Figure 2.12: The Tulipe coaxial to parallel-plate transition [33] and (right) a triangular-tapering coaxial to parallel-plate transition [34].

## 2.6 Conclusion

Different designs and performance improvement of the three antennas and a coaxial to parallel-plate transition present in literature have been discussed in this Chapter. Specific designs for the antennas and the transition are chosen, based on the requirements of this projet, and their design and modelling will be discussed in the following Chapter.

# Chapter 3

# Design and Modelling

Following the literature review, a design for each of antennas was chosen for modelling and analysis. A double ridged guide horn antenna without side walls was designed, as well as an exponentially tapering TEM horn and the Valentine antenna presented in [5]. This Chapter describes the design of these three antennas and their modelling in CST Studio Suite starting with DRGH antenna, followed by the TEM horn antenna and finally the Valentine antenna. The last section, Section 3.4, describes the design and modelling of the coaxial to parallel-plate transition required for feeding the TEM horn and the Valentine antennas.

## 3.1 DRGH Antenna

As stated earlier, the DRGH antenna is made of two main parts, a waveguide cavity with ridges and the ridged flared horn part. The design of the DRGH antenna is divided into two parts, design for impedance and design for gain. The geometry of the cavity and the ridge profile in the horn part are important in impedance matching of the antenna. The size of the aperture of the horn is a crucial consideration in gain design.

### 3.1.1 Impedance Design of the Double Ridged Waveguide

The impedance of the double ridged guide of the antenna needs to be matched to that of the coaxial feed to avoid reflections. The dimensions shown in Figure 2.3, that is, the width of the ridges, $a_0$, and the separation distance between the two ridges, $b_0$, can be designed carefully to achieve the required impedance. The antenna will be fed by a 50 $\Omega$ source through a coaxial connector. Initially, we chose a waveguide with a width ($a$) of 24.8 cm and a height ($b$) of 12.4 cm which would have a cutoff frequency close to the required lowest frequency of the antenna (200 MHz). The width of this chosen waveguide is bigger than the height, and therefore the dominant mode (mode with the lowest cutoff frequency) is a $TE_{10}$. The cutoff frequency of the fundamental mode, $(f_c)_{10}$,

of the waveguide is given by,

$$(f_c)_{10} = \frac{1}{2a\sqrt{\mu_0\epsilon_0}}, \tag{3.1}$$

where $\mu_0$ is the permeability of free space, $a$ the width of a waveguide, and $\epsilon_0$ is the permittivity of free space [39]. The dimensions of the ridge were determined following the guidelines in [11] to give enough separation between the first two modes in the waveguide. The vertical separation distance between the ridges ($b_0$) was chosen as $0.15b$ and the width of the ridges ($a_0$) as $0.5a$. When these ridges are put into the waveguide, the fundamental mode cutoff frequency, ($f_c$), of the ridged waveguide [39],

$$(f_c) = \frac{1}{2a\sqrt{\mu_0\epsilon_0}}\left[\frac{2}{\pi}\sqrt{\frac{a}{a_0}\frac{b_0}{b}\frac{1}{1-a_0/a}}\right], \tag{3.2}$$

is lowered to 0.298 GHz from 0.6 GHz calculated using 3.1.

The estimated characteristic impedance of the ridged waveguide, at infinite frequency, can also be determined by calculating the power, P, carried by the ridged guide [11] and is given by

$$P = \sqrt{\frac{\epsilon_0}{\mu_0}}\frac{E_0^2}{2\pi}\frac{\beta\lambda_c^2}{k}(C1 + C2 + C3), \tag{3.3}$$

where $\epsilon_0$ is the permittivity of free space, $\mu_0$ is the permeability of free space, $E_0$ is the electric field intensity between the ridges, $\lambda_c$ is the wavelength at the cutoff frequency and

$$\begin{aligned} C1 &= \tfrac{2\beta}{k} cos^2(\tfrac{\pi\gamma}{k}) \ln csc\tfrac{\pi b_0}{2b}, \\ C2 &= \tfrac{\pi\gamma}{2k} + \tfrac{1}{4} sin\tfrac{2\pi\gamma}{k}, \\ C3 &= \tfrac{b_0}{b}\tfrac{cos^2(\frac{\pi\gamma}{k})}{sin^2(\frac{2\pi\delta}{k})}\left[\tfrac{\pi\delta}{k} - \tfrac{1}{4} sin\tfrac{4\pi\delta}{k}\right], \\ &\text{where, } \beta = b_0/a, \gamma = a_0/a, k = \lambda_c/a, \delta = (1 - a_0/a)/2. \end{aligned} \tag{3.4}$$

Using (3.3), the power carried by the ridged guide above is calculated as 0.0682 W. Consequently, the characteristic impedance at infinite frequency can be calculated from the power equation as [11]

$$Z_{0\infty} = \frac{V_0^2}{2P} = \frac{E_0^2 b_0^2}{2P} = 50.7\ \Omega, \tag{3.5}$$

where $V_0$ is the voltage across the ridge separation. The characteristic impedance, $Z_0$, at any other frequencies can be calculated by [10]

$$Z_0(f) = \frac{Z_{0\infty}}{\sqrt{1 - (f_c/f)^2}}, \tag{3.6}$$

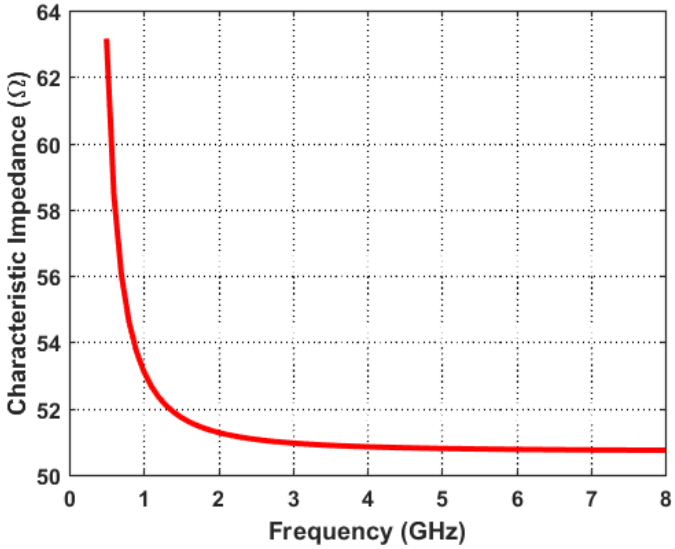


Figure 3.1: Calculated characteristic impedance of the ridged waveguide, with varying frequency

where $f_c$ is the cutoff frequency of the ridged waveguide. Figure 3.1 shows a plot of the calculated characteristic impedance for $f$ of 0 to 8 GHz. The characteristic impedance is real and approaches 50 Ω as frequency increases.

### 3.1.2 Gain Design

The double ridged guide horn antenna will be designed for 16 dBi at centre frequency of the required 200 MHz to 4 GHz band (2.1 GHz). The dimensions of the antenna shown in Figure 2.2 can be calculated using (3.7)-(3.10) [7]. The horn aperture height, $A$, is given by

$$A = 0.099aG^{0.232} + 0.42\lambda_{mid}G^{0.503} - 0.193b, \tag{3.7}$$

where $a$ is the waveguide aperture height, $G$ is the gain, $\lambda_{mid}$ is the wavelength at mid-frequency (2.1 GHz for this design) and $b$ is the waveguide aperture width. The width of horn aperture, $B$, is given by

$$B = \frac{1}{2}b + \sqrt{b^2 + 8L_H\lambda_{mid}}, \tag{3.8}$$

where $L_H$, shown in Figure 2.2, is given by

$$L_H = (A - a)\sqrt{(R_H/A)^2 - 1/4}, \tag{3.9}$$

and $R_H$ (Figure 2.2) is given by

$$R_H = A\sqrt{\frac{1}{4} + (A/(3\lambda_{mid}))^2}. \tag{3.10}$$

For the chosen waveguide dimensions above, waveguide height, $a$ of 12.4 cm and width, $b$, of 24.8 cm, the horn aperture dimensions $A$ (width) and $B$ (height) can be calculated

as 41 cm and 31 cm respectively using equations (3.7)-(3.10) above. For a 16 dBi gain at the mid-frequency, the aperture must at least be 41 cm by 31 cm.

The ridge profile of the flared horn part of the antenna was designed by first using a simple exponential profile. Initial simulations proved that the return loss achieved with this profile did not provide sufficient matching. The exponential profile opened too fast. To improve the matching, another exponential profile was used as shown in Figure 3.2. The improved exponential profile suggested in [16] terminates beyond the antenna and not necessarily at the antenna aperture as shown in Figure 3.2. A circular profile is used to connect the exponential curve with the walls of the antenna which creates rounded edges providing a longer path for signals and thus allowing lower frequency signals to be radiated.

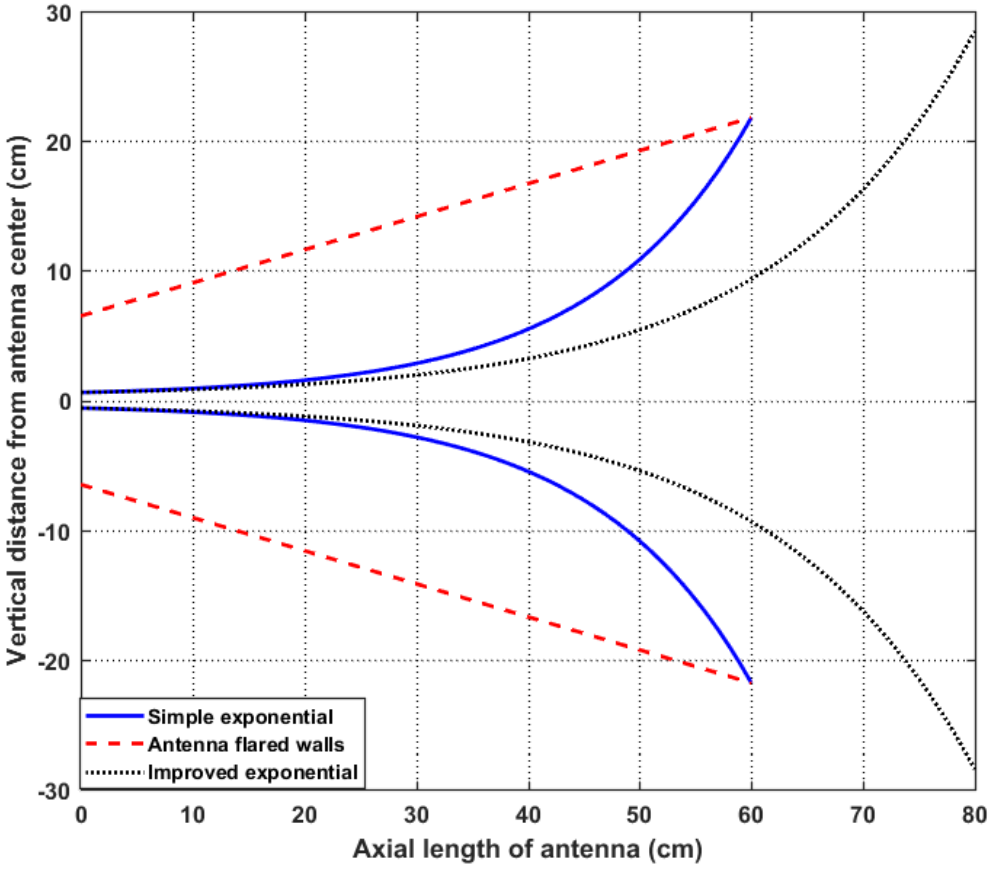


Figure 3.2: Design of ridge profile in the flared section of the DRGH antenna, a comparison of improved exponential curves that end beyond the antenna aperture versus simple exponential curves that end at the aperture. The simple exponential curves open too fast and do not give a good reflection coefficient.

### 3.1.3 Modelling in CST Studio Suite

Further design and modelling of the DRGH antenna was done in CST Studio Suite. The DRGH antenna was modelled in two steps, the back cavity and the flared horn of the antenna. The double-ridged waveguide was first modelled and simulated and the cut-off frequency of the ridged waveguide was confirmed to be 0.268 GHz. The ridged waveguide was then modified to form a cavity as shown in Figure 3.4. Wedges are designed towards the back end of the cavity starting from where the ridges end, which is approximately at the middle of the cavity. The back ends of the ridges were also rounded to minimize reflections. For feeding the antenna, an inner conductor of the coaxial cable goes through the top ridge and stops on the top face of the bottom ridge. The dielectric part of the coaxial cable terminates at the bottom face of the top ridge. The part of the coaxial inner conductor between the two ridges is tapered as shown in Figure 3.4. Tapering the inner conductor greatly improved the reflection coefficient. The diameter of the inner conductor was chosen as 3.07 mm and the diameter of the outer conductor as 10.3 mm to achieve a 50 $\Omega$ coaxial connector. The length of the waveguide cavity was chosen so that the feed is approximately at the centre of the cavity and the distance from the back wall to the centre of the feed-line is approximately $\lambda/4$, at the centre frequency of the design, as suggested by [12]. This $\lambda/4$ will transform the short circuit at the end of the cavity to an open circuit (infinite impedance) at the coaxial probe position. The ridged waveguide modelled in CST Studio Suite is shown in Figures 3.3 and 3.4 with the values of the parameters shown in Table 3.1. The complete model of the DRGH antenna designed in CST Studio Suite is as shown in Figure 3.5.

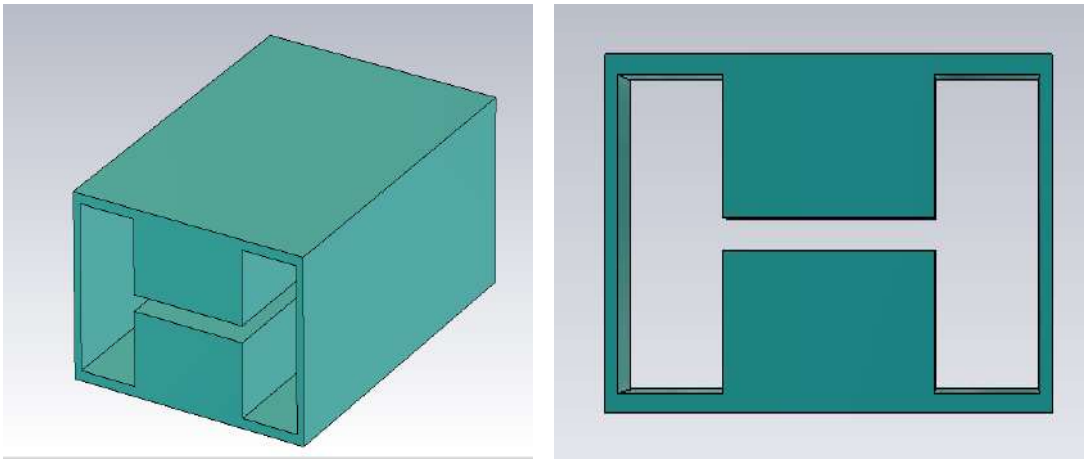

Figure 3.3: Perspective view (left) and side-view (right) of the ridged waveguide modelled in CST Studio Suite.

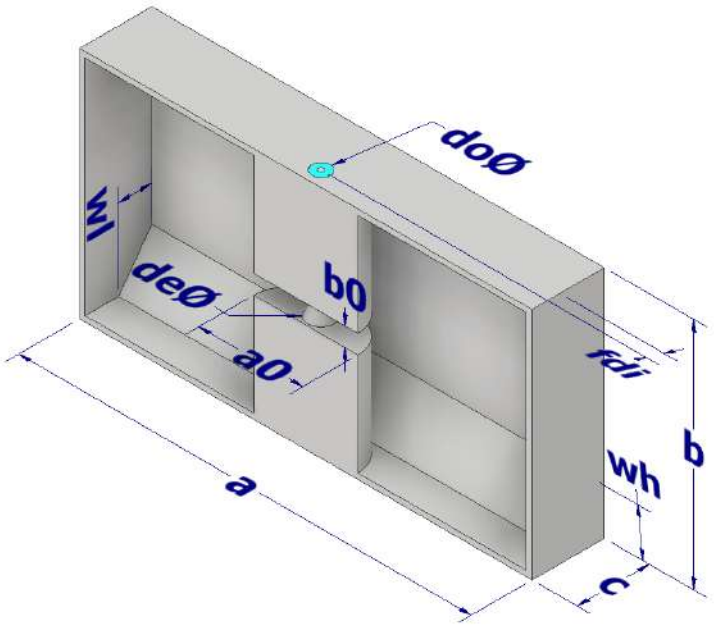


Figure 3.4: Back cavity of the DRGH with dimensions as modelled in CST Studio Suite

Table 3.1: Initial parameters for modeling the double ridged waveguide

| ***Symbol*** | ***Parameter*** | ***Value (cm)*** |
|---|---|---|
| $fdi$ | feed inset | 1.30 |
| $wh$ | wedge height | 3.10 |
| $wl$ | wedge length | 2.20 |
| $de$ | inner coaxial end diameter | 1.00 |
| $br$ | ridge blend radius | 1.85 |
| $b_0$ | ridge separation | 1.86 |
| $a_0$ | ridge width | 12.40 |
| $b$ | waveguide height | 12.40 |
| $c$ | waveguide length | 6.00 |
| $a$ | waveguide width | 24.80 |

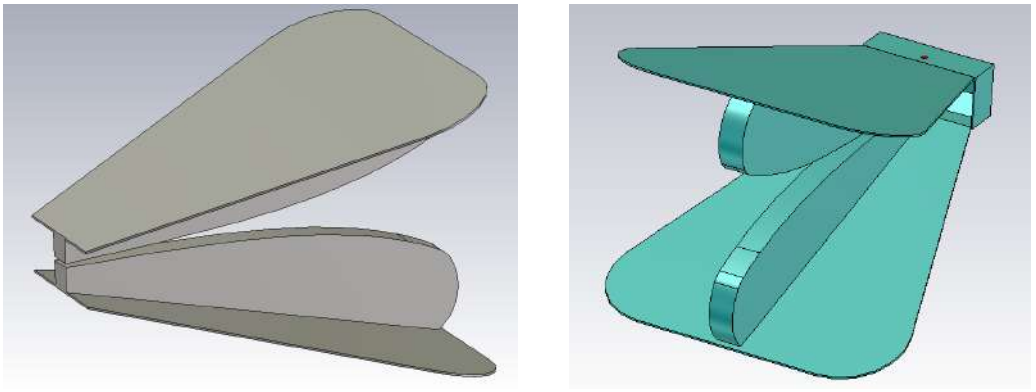

Figure 3.5: Flared section of the DRGH antenna (left) and a complete model of the DRGH antenna in CST Studio Suite (right)

The complete designed DRGH antenna as modelled in CST Studio Suite is shown in Figure 3.5. This model has a back cavity and ridges which are tapered exponentially using an improved exponential profile. The complete antenna has rounded edges both on the ridge and the E-plane walls to reduce reflections.

## 3.2 TEM Horn Antenna

An exponentially-tapering TEM horn antenna was chosen because of the reduced reflections compared to other designs as presented in Section 2.3. This section describes the design of this antenna and its modelling in CST Studio Suite.

### 3.2.1 Design

The design of the TEM horn antenna is done in two parts, that of the flared section of the horn with tapering plates and that of the coaxial to the parallel-plate transition. The latter is presented in Section 3.4.

The design of the TEM horn plates follows the design guidelines outlined in [37]. A careful design of the characteristic impedance variation between the two plates of the TEM horn has to be done to ensure that the antenna radiates properly. The two key parameters that determine the impedance of the two plates is the width of the plates and the separation distance between the plates [13]. An exponential impedance variation was chosen over other profiles because it greatly minimizes reflections along the antenna [4]. The input impedance at the feed needs to be matched to the free space impedance at the aperture of the antenna. A 20-section antenna is used to provide this matching. Each of the 20 sections is a pair of parallel plates, one on the top plate of the antenna, and another on the bottom plate of the antenna. Each of these sections is approximated as a parallel plate waveguide whose characteristic impedance, determined using an exponential matching technique is given by

$$Z(z_i) = Z_0 \exp \alpha z_i, \tag{3.11}$$

where $z_i$ is the axial distance from the feed point, $Z_0$ is the characteristic impedance of the feeding line (50Ω) and $\alpha$ is given by

$$\alpha = \frac{1}{L_{max}} \ln \frac{Z_L}{Z_0}, \tag{3.12}$$

where $L_{max}$ is the total axial length of the antenna and $Z_L$ and $Z_0$ are the free space and feed line impedance respectively. With the tapering profile of the plates, the distance between the plates increases from a minimum value until a maximum value of $d_{max}$ at the aperture. The distance of separation between the top and bottom plate at each section is calculated by

$$d(z_i) = d_{min} \exp(bz_i), 0 \leq z \leq L, \tag{3.13}$$

where b is given by

$$b = \frac{1}{L_{max}} \ln \frac{d_{max}}{d_{min}}, \tag{3.14}$$

where $L_{max}$ is the total axial length of the antenna, $d_{min}$ is the separation distance of the plates at the feed and $d_{max}$ is the separation distance of the plates at the aperture (height of the aperture).

The width of the plates also varies exponentially. A stripline approximation is used to calculate the width. Because of the small distance between the plates compared to the width of the plates, fringing fields can be ignored and the impedance of the line is given by [13]

$$Z_0 = V/I = \frac{\eta d}{w}, \tag{3.15}$$

where $\eta$ is the free space impedance, $d$ is the separation distance between the plates and $w$ is the width of the plates. The width of the plates at each section can therefore be calculated by

$$w(z_i) = \frac{\eta d(z_i)}{Z_0}. \tag{3.16}$$

The design parameters for the TEM horn antenna were calculated using (3.11)−(3.16) for an antenna whose lowest operating frequency is 200 MHz. The initial length of the horn antenna was approximated as $0.4\lambda$ (60 cm), where $\lambda$ is the wavelength at 200 MHz. The widths, separation distances of each parallel plate section, as well as the resulting impedances were then calculated using the minimum plate separation, $d_{min}$, of 1.655 cm (obtained from the transition design) and the square aperture width, $d_{max}$, of 80 cm. The calculated values are presented in Table 3.2.

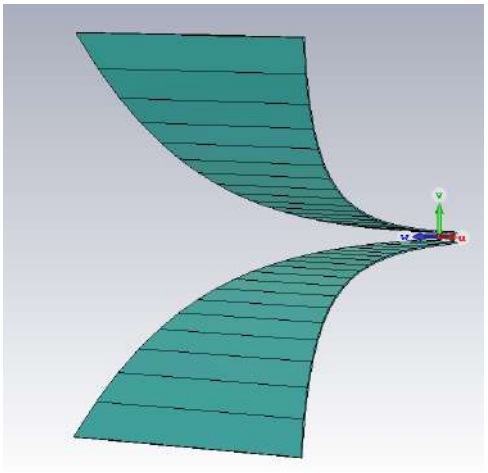

Figure 3.6: Top and bottom plates of the TEM antenna as modelled in CST Studio Suite

Table 3.2: Design parameters of the 20-section TEM Horn antenna, $z_i$ is the axial distance of each section from antenna feed, $Z(z_i)$ is the impedance of each section, $d(z_i)$ is the plate separation distance at the beginning of each section and $w(z_i)$ is the width of the plates at the beginning of each section

| **Section(i)** | $z_i$ (cm) | $Z(z_i)$ (Ohm) | $d(z_i)$ cm | $w(z_i)$ cm |
|---|---|---|---|---|
| | 0 | 50 | 1.655 | 12.48 |
| 1 | 3 | 55.3 | 2.01 | 13.70 |
| 2 | 6 | 61.2 | 2.44 | 15.03 |
| 3 | 9 | 67.7 | 2.96 | 16.49 |
| 4 | 12 | 74.9 | 3.59 | 18.10 |
| 5 | 15 | 82.9 | 4.36 | 19.85 |
| 6 | 18 | 91.7 | 5.30 | 21.79 |
| 7 | 21 | 101.4 | 6.43 | 23.91 |
| 8 | 24 | 112.2 | 7.81 | 26.24 |
| 9 | 27 | 124.1 | 9.48 | 28.80 |
| 10 | 30 | 137.3 | 11.51 | 31.60 |
| 11 | 33 | 151.9 | 13.97 | 34.67 |
| 12 | 36 | 168.0 | 16.96 | 38.05 |
| 13 | 39 | 185.9 | 20.59 | 41.75 |
| 14 | 42 | 205.7 | 24.99 | 45.82 |
| 15 | 45 | 227.5 | 30.34 | 50.28 |
| 16 | 48 | 251.7 | 36.83 | 55.17 |
| 17 | 51 | 278.4 | 44.71 | 60.54 |
| 18 | 54 | 308.0 | 54.28 | 66.44 |
| 19 | 57 | 340.8 | 65.90 | 72.90 |
| 20 | 60 | 377 | 80 | 80.00 |

### 3.2.2 Modeling in CST Studio Suite

The parameters shown in Table 3.2 were used to model the antenna in CST Studio Suite. In CST Studio Suite, all the dimensions were entered parametrically to ensure that the model could be optimized easily. Twenty polygons were carefully modelled using the dimensions in Table 3.2. The polygons were then combined to form the plates of the antenna as shown in Figure 3.6.

## 3.3 Valentine Antenna

This section describes the design and modelling of a Valentine antenna. The design presented in [5] is used because of the ease of fabrication, the rounded edges that minimize reflections and the narrow width of the plates which reduces the weight of the antenna.

The design in [5] was scaled down to meet the design requirements of this project, a low frequency of 200 MHz. Like the TEM horn antenna, the length of the Valentine antenna was determined to be 60 cm, which is $0.4\lambda$ at the lowest design frequency of 200 MHz. Each of the two parts of the antenna was modelled using two exponential profiles and thus providing an exponential matching system. The exponential curves are connected using semicircle profiles that also provide gradual rounded return path for unradiated signals. The Valentine antenna modelled in CST Studio Suite is as shown in Figure 3.7 with the modelling parameters shown in Table 3.3.

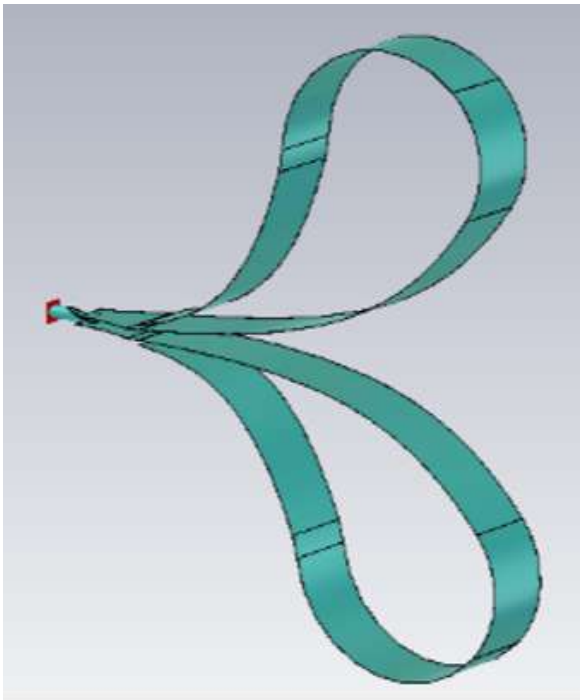

Figure 3.7: Valentine antenna modelled in CST Studio Suite

Table 3.3: Design parameters of a Valentine antenna

| **Symbol** | **Parameter** | **Value** (cm) |
|---|---|---|
| $L_{max}$ | axial length | 70 |
| $d_{max}$(inner) | aperture height (inner) | 60 |
| $d_{max}$(outer) | aperture height (outer) | 100 |
| $d$ | semicircle diameter | 40 |
| $d_{min}$ | plate separation distance at feed | 1.655 |

## 3.4 Coaxial to Parallel-plate Transition

From the literature review analysis of Section 2.5, a coaxial to parallel-plate transition similar to the triangular-tapering transition presented in [34], was designed. The initial dimensions of the transition were chosen to make the length of the transition approximately equal to $\lambda/8$ at the lowest frequency (200 MHz) and it was then optimized to reduce the length and size as much as possible. Exponentially-tapering plates were used instead of linearly tapering plates as shown in Figure 3.8. The exponentially-tapering transition improved the return loss across all frequencies compared to the linearly-tapering transition as shown in Figure 3.9, where the two transitions have comparable length. An unconventional 50 Ω coaxial connector with an inner diameter of 7 mm and an outer diameter of 1.61 cm is used. These unusually large dimensions of the connector were chosen to maintain a large enough distance between the plates and to make the transition sturdy and robust. The outer coaxial conductor is cut at angle as shown in Figure 3.8 while the inner coaxial conductor tapers outwards away from the trimmed outer conductor until it connects to the plates. The coaxial connector is air-filled for added ease of fabrication. For measurements, the coaxial connector of the coaxial to parallel-plate transition is terminated with a 4-hole flange which is connects to a flanged N-type connector.

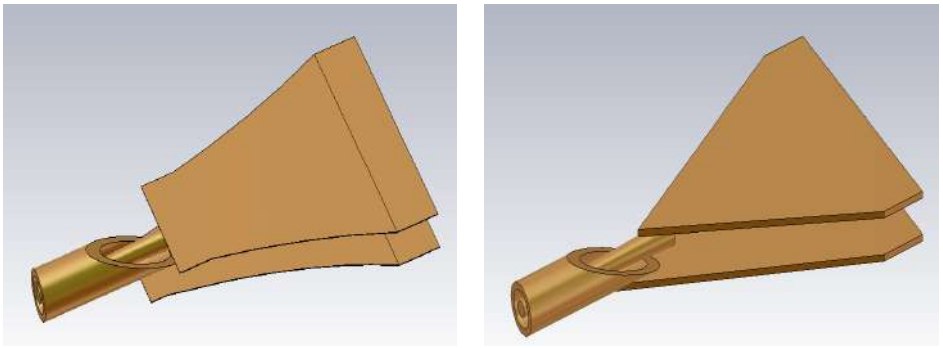

Figure 3.8: Exponentially-tapering (left) and linearly-tapering (right) coaxial to parallel-plate transitions.

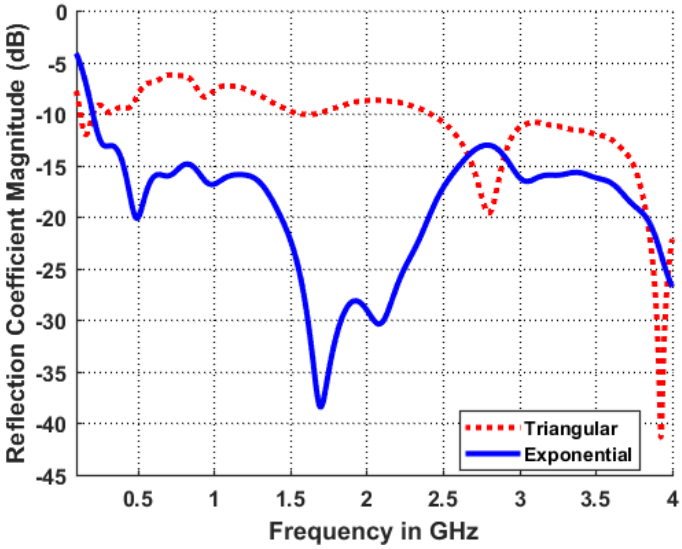


Figure 3.9: Reflection coefficient magnitude of the exponentially-tapering coaxial to parallel-plate transition, where the top and bottom plates start at a given width and exponentially tapers, compared to the reflection coefficient of a linearly-tapering transition, both shown in Figure 3.8. The two transitions are both of the same length.

Figure 3.10 and Table 3.4 show more elaborate dimensions of the exponentially-tapering coaxial to parallel-plate transition as modelled in CST Studio Suite. The total length of the transition is 22 cm.

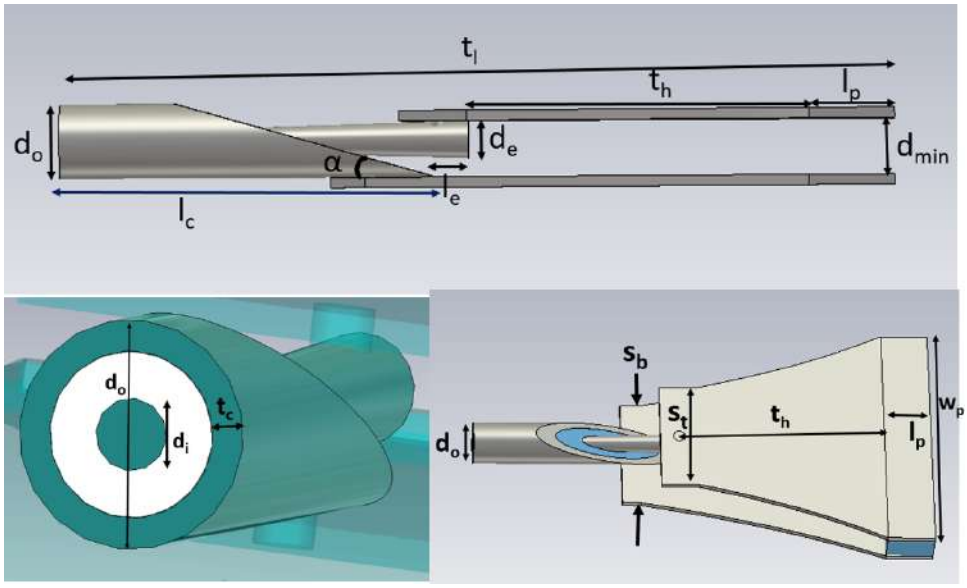


Figure 3.10: Dimensions of the exponentially-tapering coaxial to parallel-plate transition, a side-view, end-view and top-view, with the parameter values shown in Table 3.4

.

Table 3.4: Parameters for the modelled coaxial to parallel-plate transition, angle in ° and length in cm

| Symbol | Parameter | *Value* |
|---|---|---|
| $\alpha$ | angle | 21.00 |
| $l_c$ | coaxial length | 8.00 |
| $d_0$ | coaxial outer conductor diameter | 2.21 |
| $d_i$ | coaxial inner conductor diameter | 0.70 |
| $d_e$ | coaxial inner conductor end diameter | 1.10 |
| $t_c$ | outer coaxial conductor thickness | 0.30 |
| $d_{min}$ | transition plates separation distance | 1.66 |
| $l_p$ | length of parallel plate | 2.50 |
| $w_p$ | width of parallel plate | 12.48 |
| $s_b$ | start width of bottom plate | 4.00 |
| $s_t$ | start width of top plate | 6.00 |
| $l_e$ | extended length | 1.50 |
| $t_h$ | triangle height | 10.00 |
| $t_l$ | total length of transition | 22.00 |

## 3.5 Conclusion

The three antennas have been successfully designed and modelled in CST Studio Suite, a DRGH without side walls, an exponentially-tapering TEM horn antenna and a Valentine antenna with an exponential profile. Several techniques have been employed to improve the performance of the antennas such as rounding of edges for the DRGH ridges and the Valentine antenna and the use of wedges inside the DRGH cavity. A wideband coaxial to parallel-plate transition has also been designed and modelled for use with the TEM horn and the Valentine antennas. The following chapter, Chapter 4, will describe the fabrication of these antennas. Chapter 5 will present the simulated results of these modelled antennas as well as the measured results of the fabricated antennas.

# Chapter 4

# Fabrication

After a preliminary parametric study of the three antenna models in CST Studio Suite and satisfactory initial simulated results, low-cost prototyping of the antennas was considered. This was done to analyse the complexity involved in building them as well as to be able to perform measurements to compare to the simulated results as presented in Chapter 5. The three modelled antennas, whose perspective view and dimensions shown in Figure 4.1 and side-view in Figure 4.2, were fabricated. The three antennas were prototyped using the facilities available in-house, at Stellenbosch University. All the three antennas are terminated with a special N-type RF connector (Part number: SC9245, by Fairview Microwave) with a thicker centre conductor for rigidity. The coaxial connector of the coaxial to parallel-plate transition is terminated with a 4-hole square flange which allows the system to be connected to a flanged N-type connector.

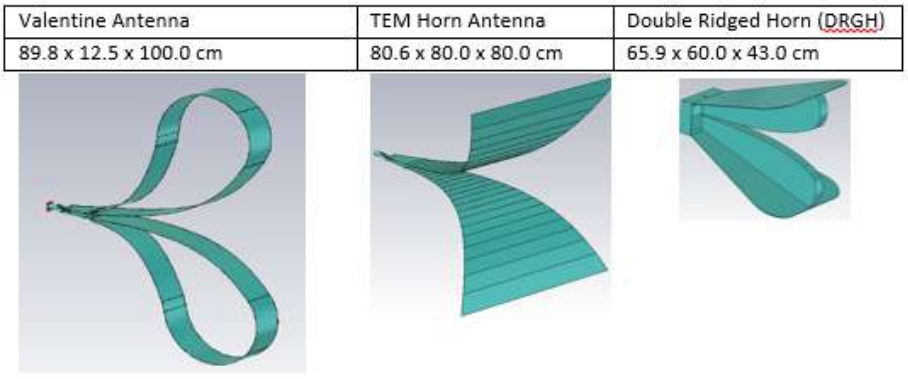


Figure 4.1: A perspective view of the three modelled antennas

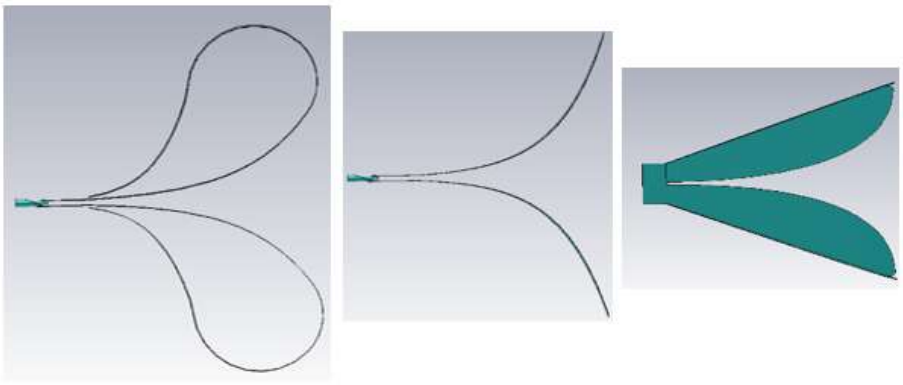

Figure 4.2: A side-view of the three modelled antennas

## 4.1 Valentine and TEM Horn Antennas

The fabrication of these two antennas was done in two steps. First, the exponentially-tapering coaxial to parallel-plate transition, shown in Figure 3.8, was made for each of the antennas. The top and bottom exponential tapering plates of the transition whose dimensions are shown in Figure 4.3, were laser-cut. Additional fabrication dimensions of the coaxial to parallel-plate transition are shown in Figure 3.10 and Table 3.4. The trimmed dimensions of the coaxial outer conductor and the tapered inner conductor are shown in Figure 4.4. The entire transition was made from brass and perspex was used to provide a base support. Polystyrene pieces were used to provide vertical separation between the plates. The fabricated coaxial to parallel-plate transition is shown in Figure 4.5.

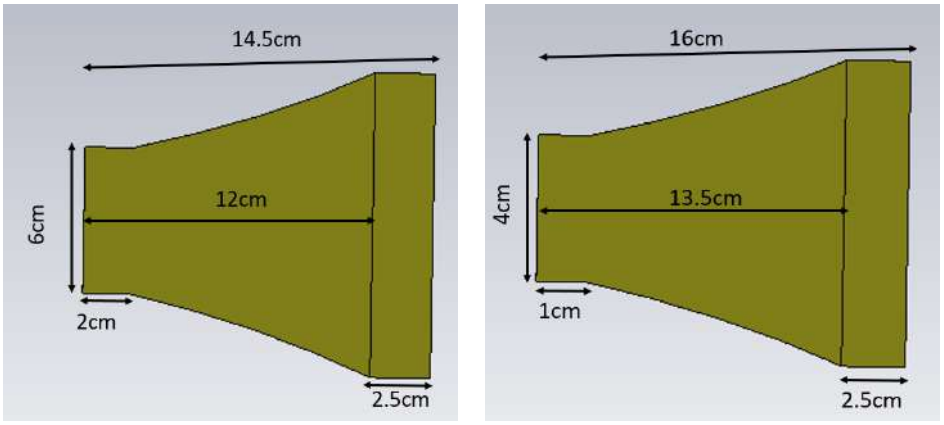


Figure 4.3: Top (left) and bottom (right) plate dimensions of the exponentially-tapering coaxial to parallel-plate transition

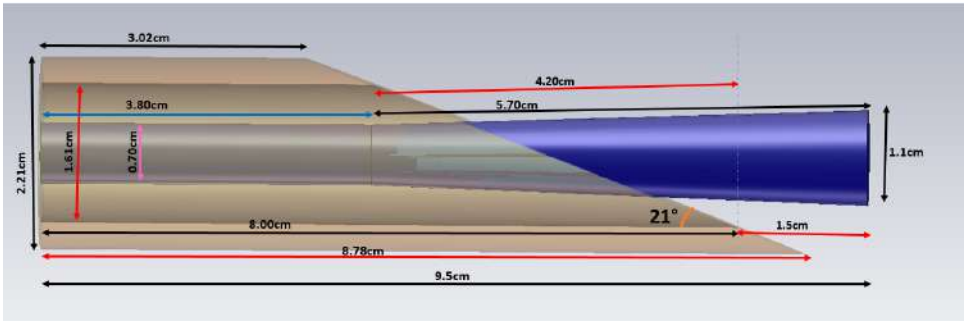


Figure 4.4: The fabricated dimensions of the trimmed air-filled coaxial transition

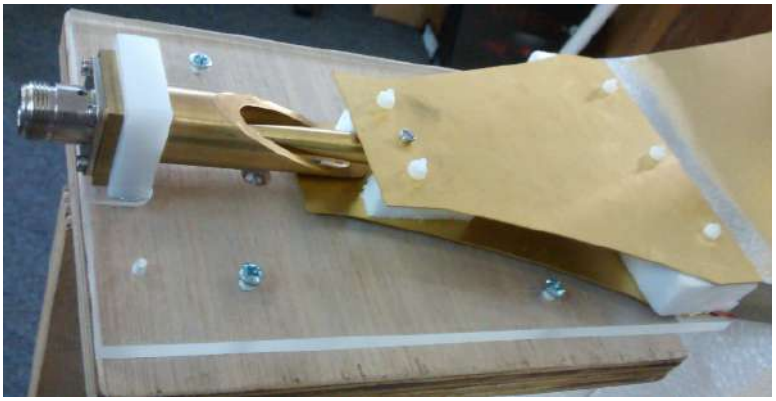

Figure 4.5: The fabricated exponentially-tapering coaxial to parallel-plate transition

In the second step of fabrication, the plates of the two antennas were cut out and bent to follow their respective profiles. The flattened plates of the TEM horn antenna, whose outline is shown in Figure 4.6, were cut out from a sheet of brass and bent along the profile shown in Figure 4.6.

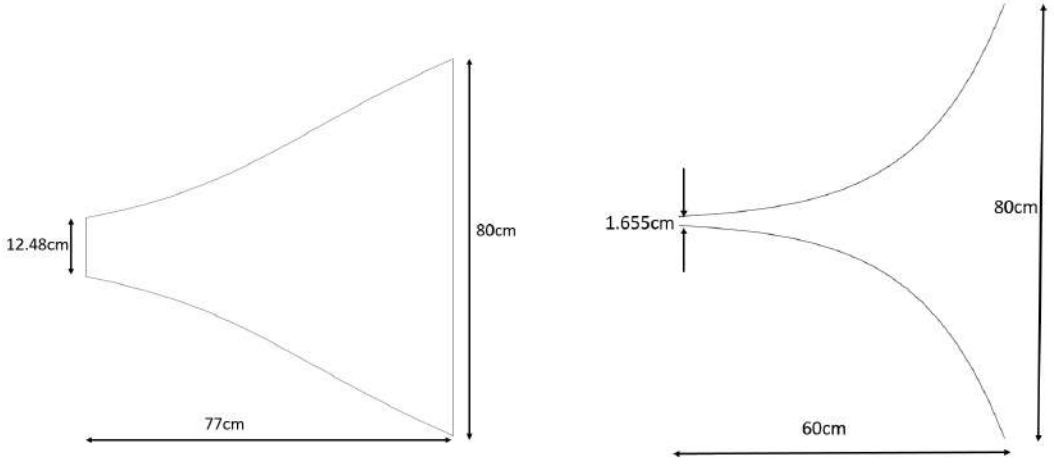


Figure 4.6: Outline of flattened TEM horn plates (left) and the folding profile (right) for the TEM horn antenna plates.

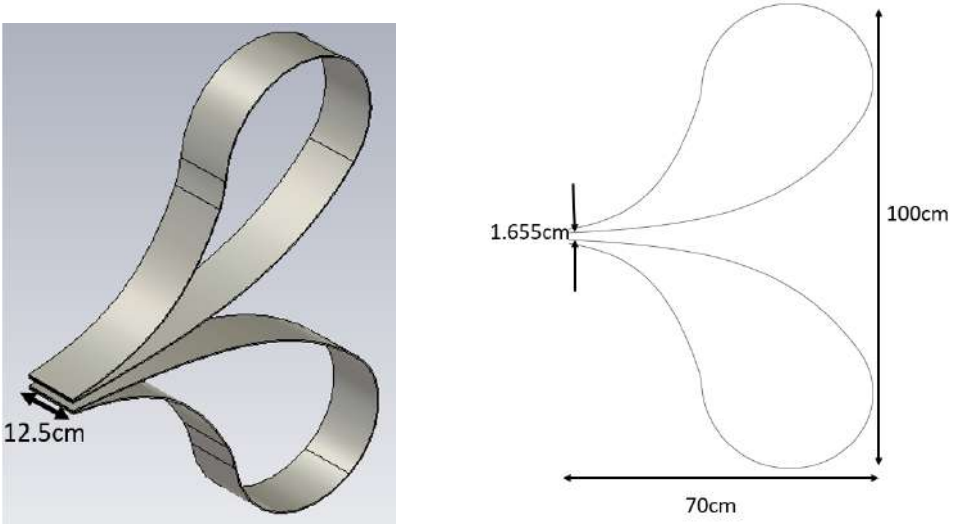


Figure 4.7: The 12.5 cm wide Valentine antenna plates (left) and the folding profile (right).

The 12.5 cm wide plates for the Valentine antenna, were cut from a tin-plated mild steel of 0.3 mm thickness. A number of plates were soldered, as needed, to get the desired length and folded along the profile shown in Figure 4.7. Figure 4.8 shows the fabricated TEM horn and Valentine antennas. Polystyrene was used and was sufficient to mechanically support both antennas' plates. However, it was hard to support the TEM horn plates solely with Polystyrene. Additionally, a wooden stand was made for the TEM horn to provide further mechanical support at the feed and to provide a height at which the plates to taper from. This resulted in a heavier fabricated TEM horn compared to the Valentine antenna, however, the TEM horn antenna was more stable and sturdy. The weight of the assembled Valentine antenna, including its polystyrene stand is 5 kg, compared to 7 kg of the TEM horn antenna. While doing the outdoor measurements, the Valentine antenna was easily blown by the wind because of its large surface area and light weight and additional mechanical support, to keep it in place, was required.

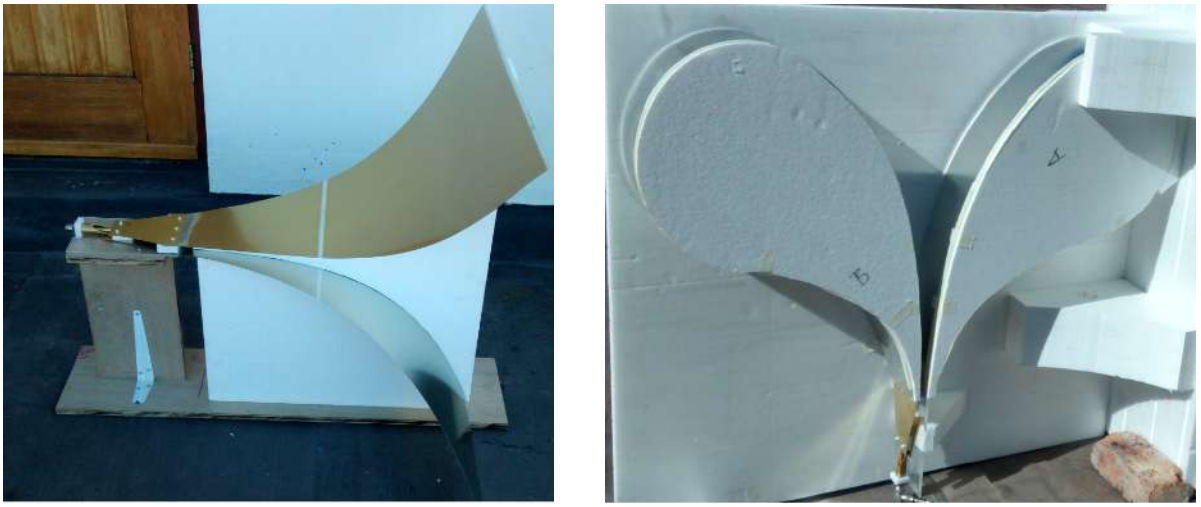

Figure 4.8: Fabricated TEM horn antenna with a wooden base support (left) and fabricated Valentine antenna (right) with Polystyrene stand

## 4.2 Double-Ridged Guide Horn Antenna

The back cavity section of the DRGH, including the ridges and the wedges were modelled in a 3-dimensional CAD (Computer-Aided Design) software as two different parts shown in Figure 4.9. The two parts fit into each other to form the complete back cavity of the DRGH. The two parts were 3D-printed in plastic and coated with Aluminium tape. A hollow cylindrical part was machined from metal and inserted into the hole shown in Figure 4.9 to hold the coaxial feed. For the flared part of the DRGH, the top and bottom plates were cut out of plastic and covered in Aluminium tape. The ridges of the flared part were cut out from Polystyrene, coated in Aluminium tape and glued to the top and bottom plates of the antenna. The final fabricated DRGH antenna, whose dimensions are shown in Figure 4.10 and Table 4.1, is shown in Figure 4.11. Like the TEM horn antenna and the Valentine antenna, Polystyrene was used to provide additional mechanical support for the DRGH, between the plates and under the bottom plate of the antenna. The antenna was also fixed on a wooden stand for stability and sturdiness. The weight of the assembled DRGH antenna is 5 kg.

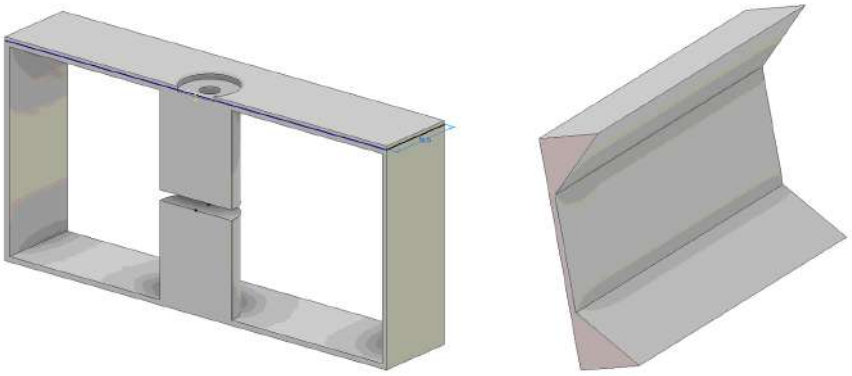

Figure 4.9: The back cavity of the DRGH modelled as two parts for 3D printing.

Table 4.1: Fabrication dimensions of the DRGH, the parameters are illustrated in Figure 3.4.

| **Symbol** | Parameter | ***Value(cm)*** |
|---|---|---|
| $fdi$ | feed inset | 0.80 |
| $wh$ | wedge height | 3.00 |
| $wl$ | wedge length | 3.00 |
| $de$ | coaxial pin end diameter | 1.00 |
| $br$ | ridge blend radius | 1.85 |
| $b_0$ | ridge separation | 0.60 |
| $a_0$ | ridge width | 5.00 |
| $b$ | waveguide height | 12.19 |
| $c$ | waveguide length | 5.00 |
| $a$ | waveguide width | 26.00 |
| $A$ | horn aperture height | 43.00 |
| $B$ | horn aperture width | 60.00 |
| $L_{max}$ | antenna axial length | 60.00 |

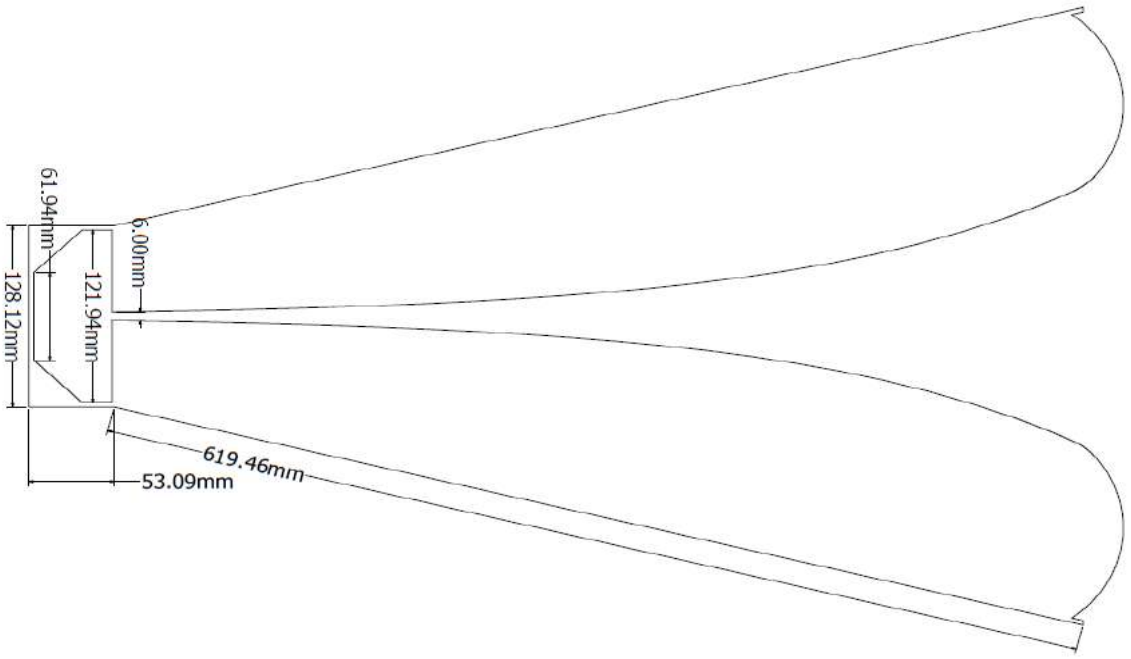


Figure 4.10: Side-view dimensions of the DRGH showing the wedges in the back cavity, the top and bottom plates and the ridge profile.

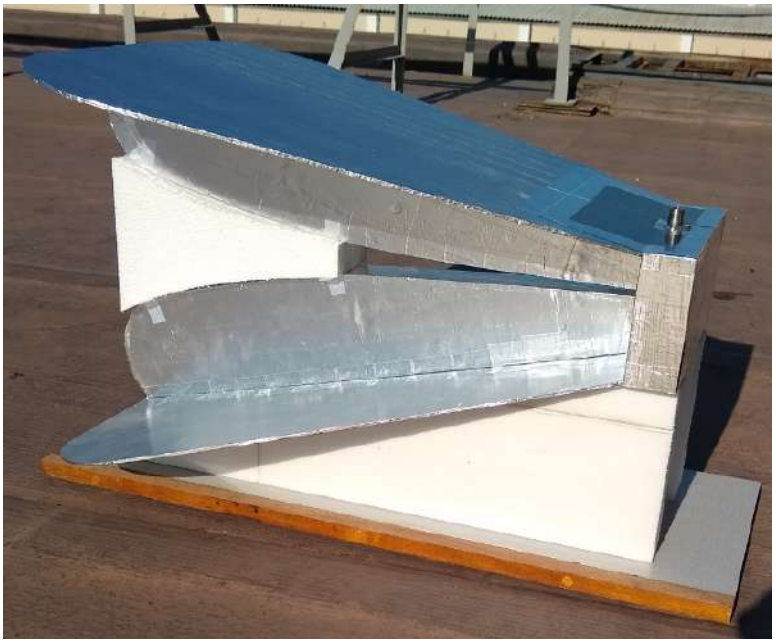

Figure 4.11: The fabricated Double-Ridged Guide Horn antenna

## 4.3 Discussion

All the three antennas are fed via an N-type coaxial connector. Apart from the Valentine antenna, they are all sturdy. All the antennas are less than 7 kg which makes them easily portable. The largest dimensions of the antenna are within reasonable limits and the

antennas can go through doors and can easily be carried by one person. All the three antennas were fairly simple to make and did not consume too much time and resources. The fabricated DRGH antenna, with stand, is the shortest of all the three fabricated antennas at 80 cm while the Valentine is the longest of all the antennas at 118 cm. Table 4.2 provides an in-depth comparison of the weight, volume and dimensions of the three fabricated antennas. A picture comparing the three fabricated antennas is shown in Figure 4.12. Overall, the DRGH is the most compact of the three antennas. The wooden stands of the DRGH and the TEM make the two antennas sturdy and stable. Although the Valentine antenna is light (5 kg) for its size, it is not stable enough to stand in an outdoor windy environment and requires additional mechanical support.

Figure 4.12: The three fabricated antennas compared side by side, Valentine antenna on the far left, TEM horn antenna at the middle, and DRGH on the far right. The DRGH is the smallest of all the three antennas.

Table 4.2: Size comparison of the three fabricated antennas

| **Parameter** | **DRGH** | **TEM horn** | **Valentine** |
|---|---|---|---|
| Length (cm) | 80 | 92 | 118 |
| Width (cm) | 54 | 80 | 49 |
| Height (cm) | 48 | 83 | 113 |
| Weight (kg) | 5 | 7 | 5 |
| Packaging volume ($m^3$) | 0.2 | 0.6 | 0.7 |

## 4.4 Conclusion

The three antennas have been successfully fabricated as discussed in this chapter. A DRGH would be chosen over the other two antennas because of its small size and sturdiness. However, the performane of the three antennas need to be compared before deciding on an antenna. The following chapter, Chapter 5, will present and discuss the results of these antennas as simulated in CST Studio Suite and compare them with those measured from the fabricated antennas.

# Chapter 5

# Simulated and Measured Results

The simulations presented in this thesis were obtained using the Time Domain (TD) solver of CST Studio Suite [6]. This section compares the simulated performance of the three antennas with each other as well as the measured results of the fabricated antennas with those simulated for each antenna. Three characteristics of the antennas will be analysed: the reflection coefficient, the radiation patterns and the realized gain. Most of these results have already been presented in [40].

## 5.1 Reflection Coefficient

### 5.1.1 Simulation

Figure 5.1 shows the simulated reflection coefficients of the three antennas that were fabricated. The -10 dB bandwidth-ratio of the DRGH is 11, although with a narrow mismatch at 2.72 GHz where the reflection coefficient is -8.5 dB. The reflection coefficients of the other two antennas are very similar to that of the DRGH, both with a -10 dB bandwidth-ratio of 10. Similar to the DRGH, the -10 dB bandwidth-ratio of the two antennas could potentially be increased by getting rid of the mismatch at 360 MHz where the reflection coefficient is -8.7 dB. The DRGH outperforms the other two antennas at the low frequency end but the TEM horn and the Valentine antenna are better matched at high frequencies. Overall, the DRGH has a better bandwidth than the other two antennas.

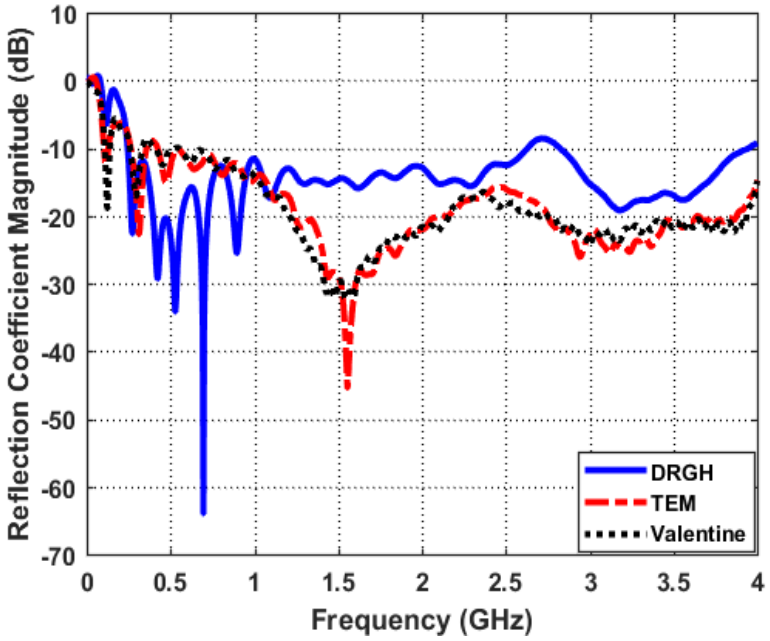


Figure 5.1: Comparison of the simulated reflection coefficients of the three fabricated antennas

### 5.1.2 Measurement

The reflection coefficient of the three antennas was measured inside the anechoic chamber at the Radio Frequency Laboratory at Stellenbosch University using an Agilent N5242A Vector Network Analyser (VNA) as shown in the set-up of Figure 5.2. The reflection coefficient measurements of the Valentine and the TEM horn antennas were repeated outdoors with an Anritsu USB VNA with the antennas facing up in the sky as shown in Figure 5.3. The measurements were done twice, indoors and outdoors to check their repeatability.

The measured reflection coefficients of each of the three antennas are compared to the simulated reflection coefficients in Figure 5.5. The measured results of the TEM horn and the Valentine antennas were verified to be repeatable by the two measurements done indoors and outdoors as shown in Figure 5.5. The measured reflection coefficients are in good agreement with the simulated reflection coefficients except at a few frequencies. The measured -10 dB bandwidth-ratio for the TEM horn and the Valentine antennas is reduced from that simulated by a mismatch at 2.75 GHz. This large reduction in reflection coefficient noted at 2.75 GHz in both of the TEM horn and the Valentine antenna measurements, is attributed to the slight variation in the fabricated and simulated coaxial to parallel-plate transition. This mismatch was tracked in time domain using the Inverse Fourier Transform feature of the Vector Network Analyser (VNA) and noted to come from the coaxial to parallel-plate transition part of the antenna. A parametric study of the transition also revealed that slight changes, in the order of millimetres, in

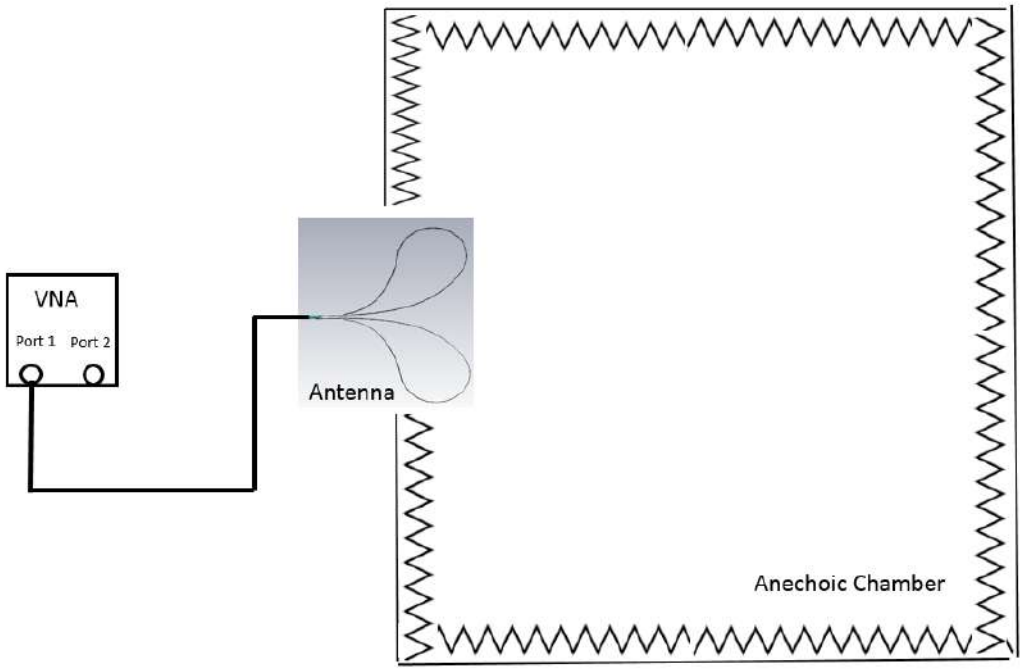


Figure 5.2: Set-up for measuring reflection coefficient inside the anechoic chamber

Figure 5.3: Set-up for measuring reflection coefficient outdoor with the TEM horn antenna facing up in the sky.

the length of the tapering inner coaxial conductor of the transition, resulted in a sudden change in the reflection coefficient at 2.75 GHz as shown in Figure 5.4. This mismatch could therefore be attributed to the manufacturing tolerances of the transition, which are in the order of a few millimetres. The measured reflection coefficient of the DRGH closely replicates that simulated except some little difference in the low frequencies. The bandwidth-ratio of the measured DRGH is also close to that simulated. The variation of the measured reflection coefficients of all the three antennas observed below 1 GHz is because the anechoic chamber is designed to work well only above 1 GHz. Moreover, underneath the rooftop where the outdoor measurements were done, for the TEM horn and the Valentine antennas, is a copper plate which could also be responsible for additional reflections noted in the outdoor measurements.

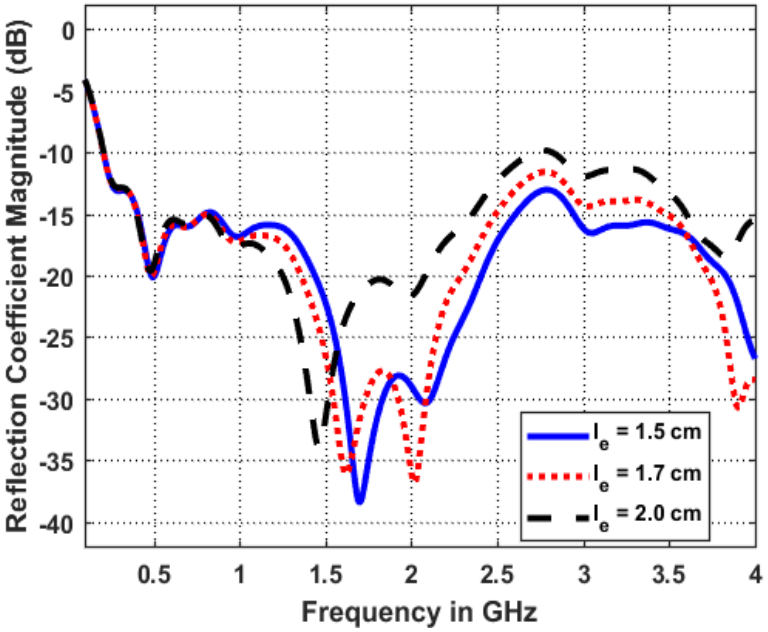


Figure 5.4: According to parametric simulations, a small increase in length of the inner coaxial conductor that extends beyond the outer coaxial conductor, $l_e$, of Figure 3.10, leads to increased reflection coefficient of the coaxial to parallel-plate transition at 2.75 GHz.

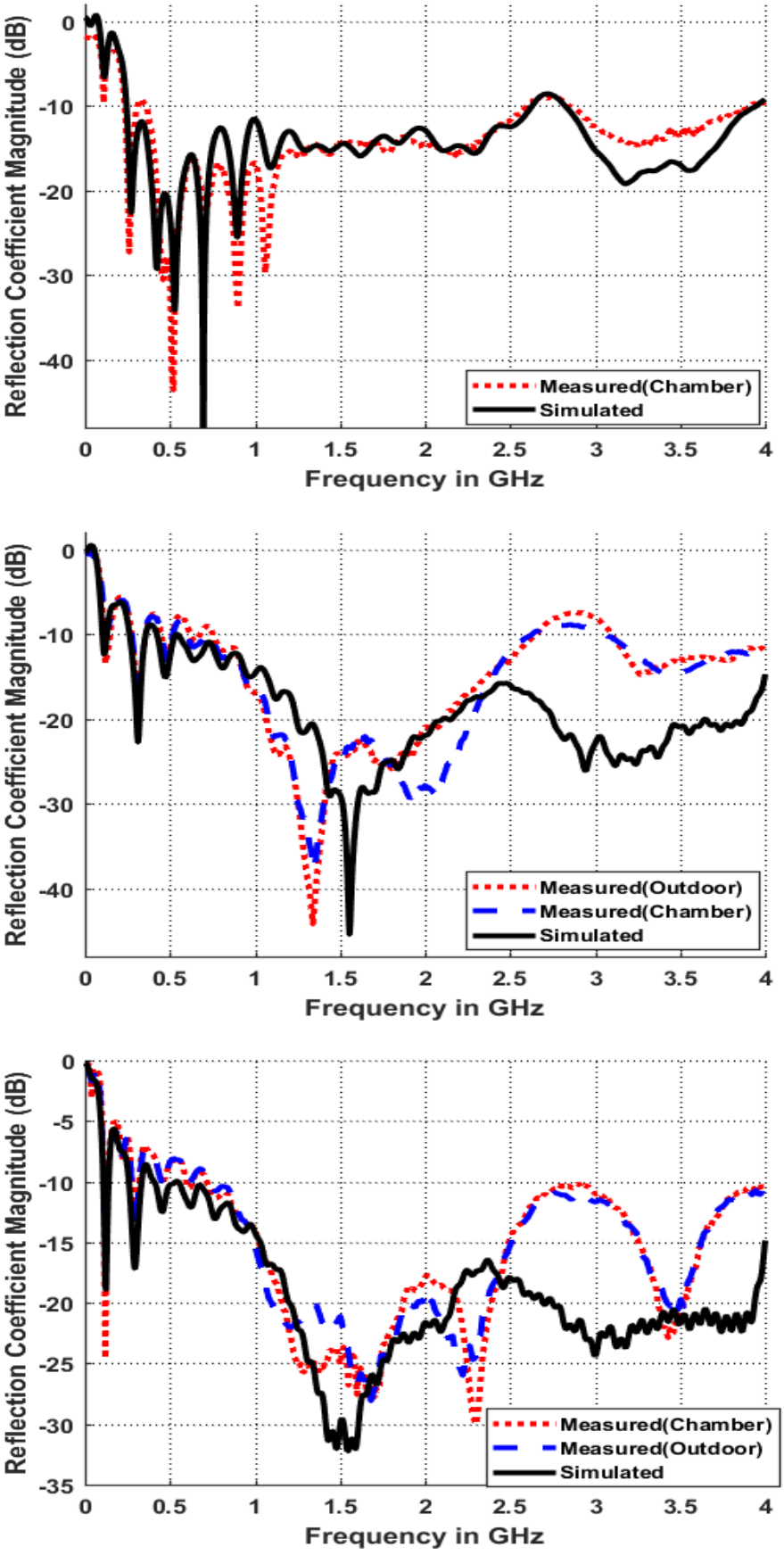


Figure 5.5: Measured and simulated reflection coefficient magnitude of the DRGH (top), TEM horn (middle) and Valentine (bottom) antennas

## 5.2 Radiation Patterns

### 5.2.1 Simulation

The simulated far-field radiation patterns of the three antennas at three different frequencies are shown in the polar plots of Figure 5.6. The three antennas have better directivity at high frequencies compared to the low frequencies. The beamwidth in the H-plane is also wider than the beamwidth in the E-plane for all three as would be expected because all the three antennas do not have H-plane walls.

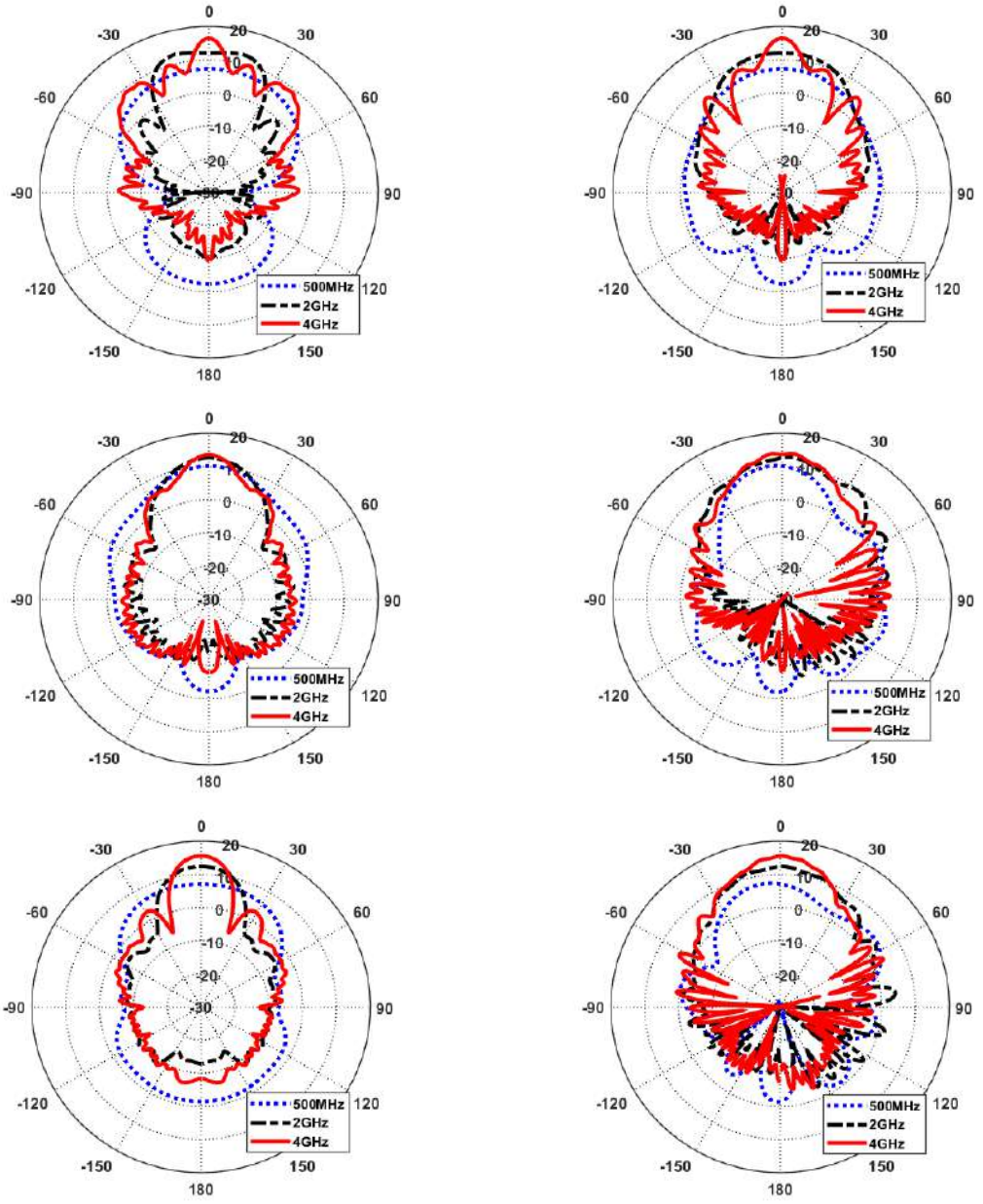


Figure 5.6: The simulated E-plane (left column) and H-plane (right column) directivity radiation patterns of the three antennas: DRGH (top), TEM horn (middle) and Valentine (bottom) antennas at 500 MHz, 2 GHz and 4 GHz.

The main lobe of the DRGH radiation splits at high frequency above 2.6 GHz while those of the Valentine and the TEM horn antennas remain rounded as shown in the 3D radiation patterns in Appendix E. The beamwidth of the main beam of the Valentine antenna is the narrowest of all the three antennas in the E-plane. Figure 5.7 shows the E-plane and the H-plane half-power beamwidth of the three antennas as a function of frequency. The beam narrows with frequency for all the three antennas. The DRGH has the narrowest main beam at 4 GHz where the 3-dB (half-power) beamwidth is about 10 degrees. The TEM horn antenna has the narrowest beamwidth at 500 MHz in both the E-plane and the H-plane.

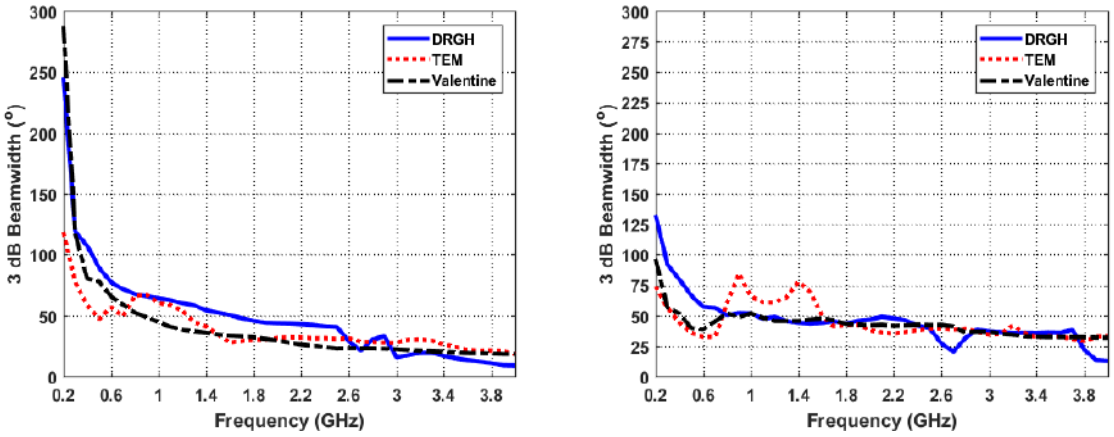


Figure 5.7: E-plane (left) and H-plane (right) half-power (3-dB) beamwidth of the three antennas as a function of frequency.

### 5.2.2 Measurements

A near-field planar scan of the three antennas was done to compare the measured radiation patterns to those simulated. The antennas were set-up inside the anechoic chamber as shown in Figures 5.8 and 5.9. A scanning probe, model OEWG WR187, operating in the 3.95 - 5.85 GHz range, was used to determine the radiation patterns of the three antennas. This limited the frequencies at which the antenna radiation patterns could be determined, therefore the measurement was set to acquire data from 3.5 to 4 GHz. The antennas were positioned about $3\lambda$ away from the probe and a scan with angular span of 120 (-60 to 60) degrees was done. Figures 5.10 - 5.12 compare the measured radiation patterns with those simulated for the three antennas at three selected frequencies. For all three measurements, the maximum scanning area span was less than 1.7 m in both the X and the Y direction.

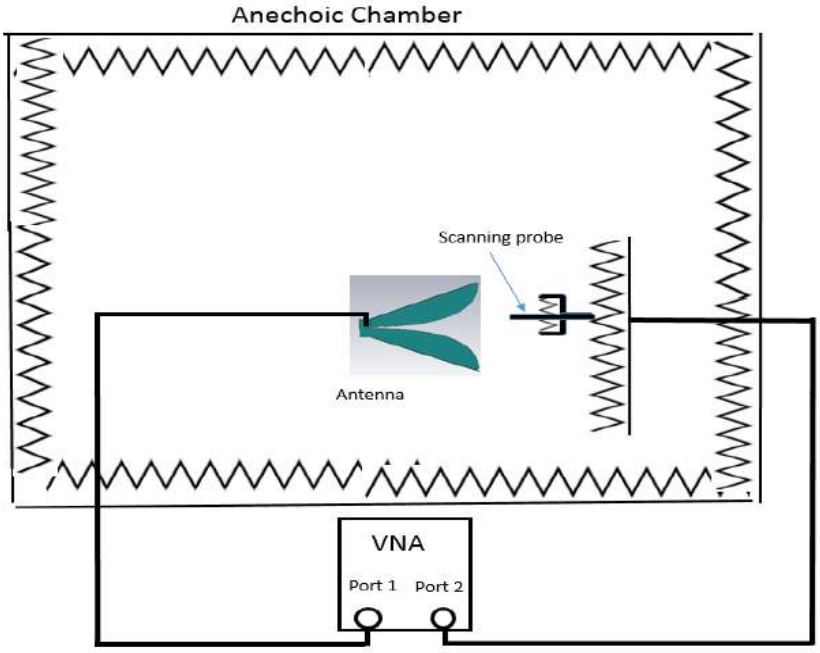


Figure 5.8: Planar scan measurement set-up inside the anechoic chamber

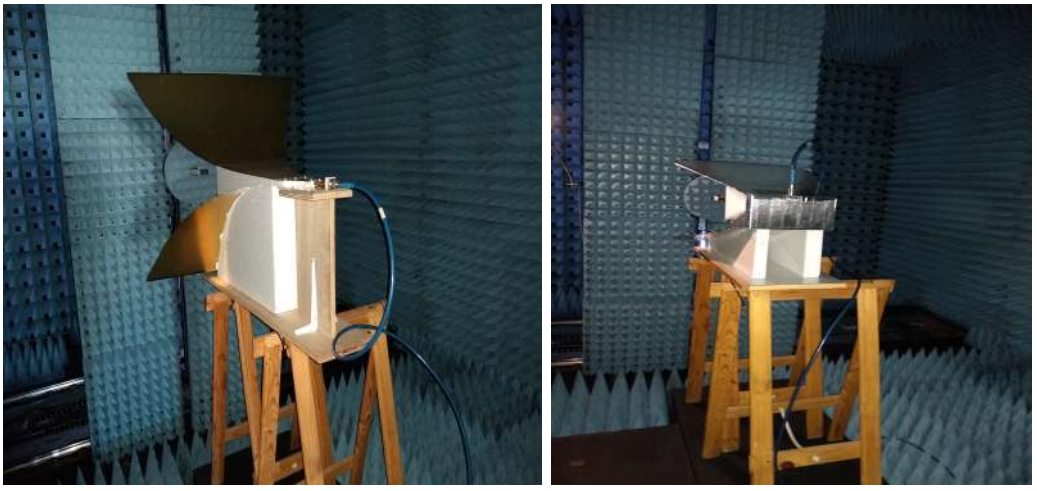

Figure 5.9: TEM horn antenna (left) and DRGH antenna (right) set-up for the radiation pattern planar scan measurement inside the anechoic chamber.

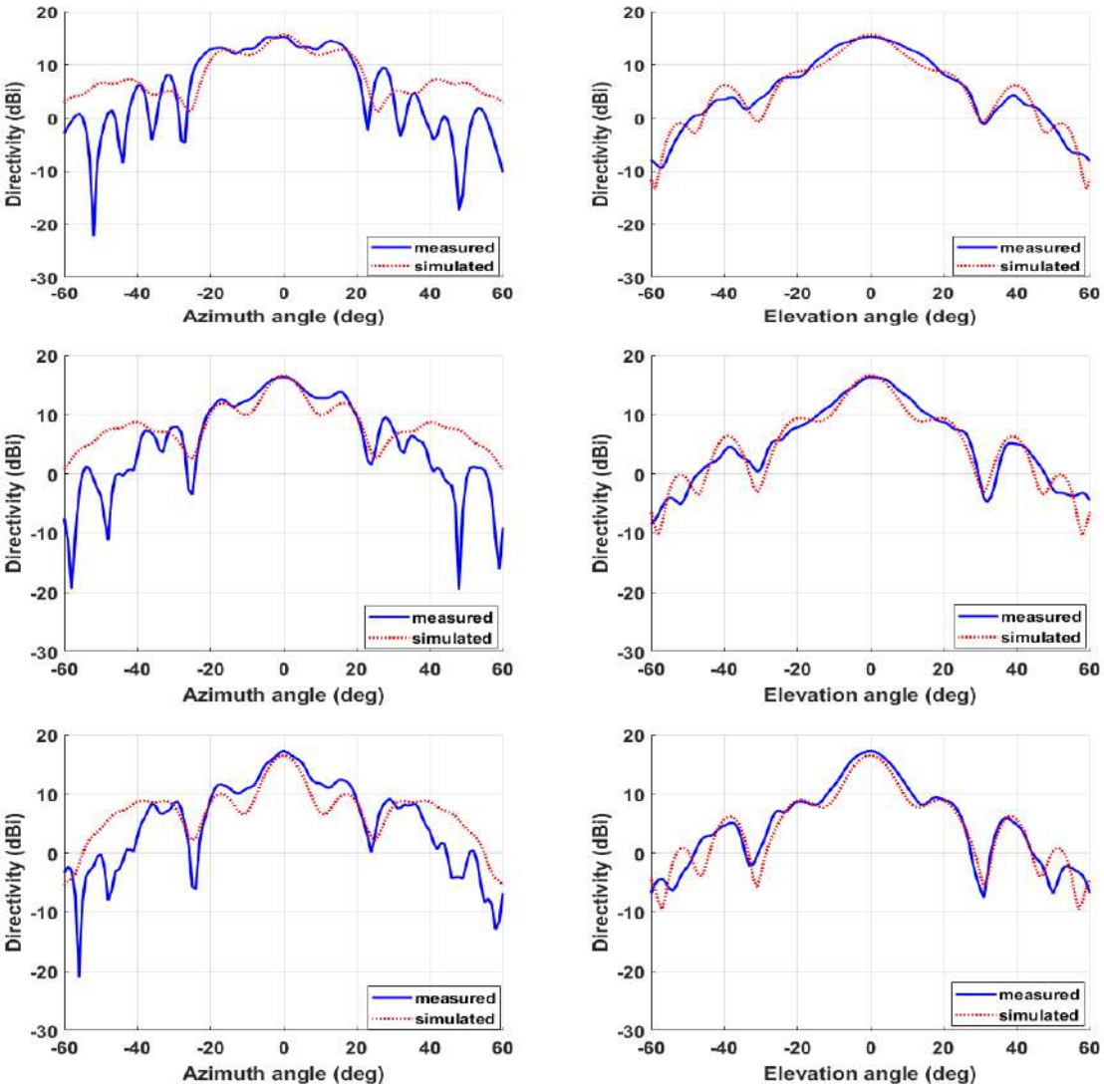


Figure 5.10: The measured E-plane (left column) and H-plane (right column) directivity radiation patterns of the fabricated DRGH antenna at 3.6 GHz (top), 3.8 GHz ( middle), and 4 GHz (bottom).

The far-field radiation patterns are in good agreement with the simulated radiation patterns, particularly for the DRGH because of its relatively small size. Because of the large size of the Valentine antenna and the TEM horn antennas, the accuracy (number of points) that could be obtained for the scan was limited by the small scan area of the probe of about 1.7 m in the X-axis and 1.5 m in the Y-axis. The amplitude of the near field power at the edges was at an average minimum of about -25 dB to -20 dB for the Valentine and the TEM horn antennas as shown in 5.13, but at least -30 dB for the DRGH. A large enough probe scanning area is a requirement to obtaining accurate results. The amplitude of the measurements at the edges of at least 30 dB below the near field peak [41], is required in order to obtain accurate scan results. This is barely met for the DRGH and not met for the TEM horn and the Valentine antennas as shown

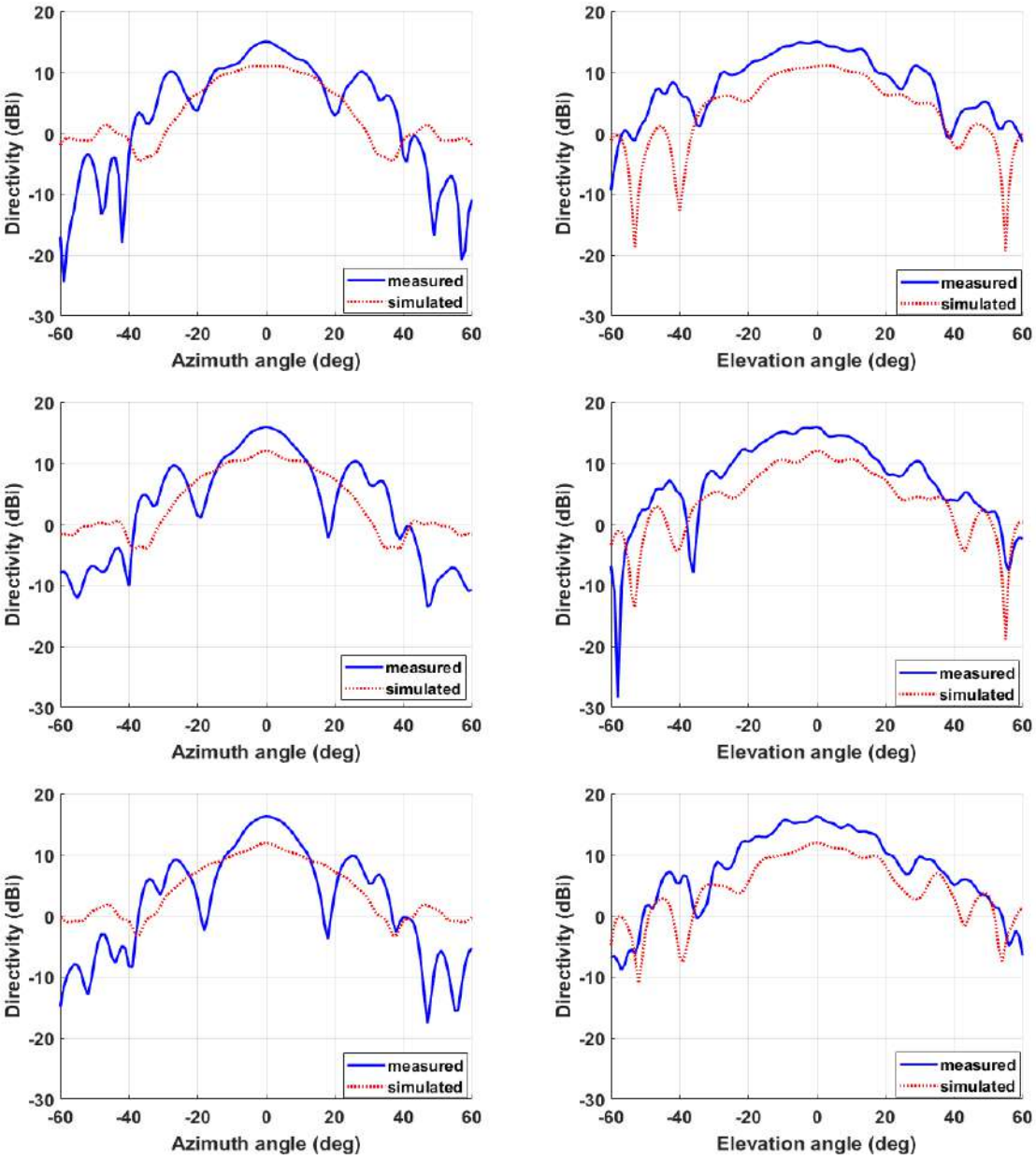


Figure 5.11: The measured E-plane (left column) and H-plane (right column) directivity radiation patterns of the fabricated TEM horn antenna at 3.5 GHz (top), 3.8 GHz (middle) and 4 GHz (bottom).

in 5.13. However, the main lobe radiation pattern of the three antennas, similar to those simulated, though with different directivity levels, is evident in the measured results and this validates the simulated patterns.

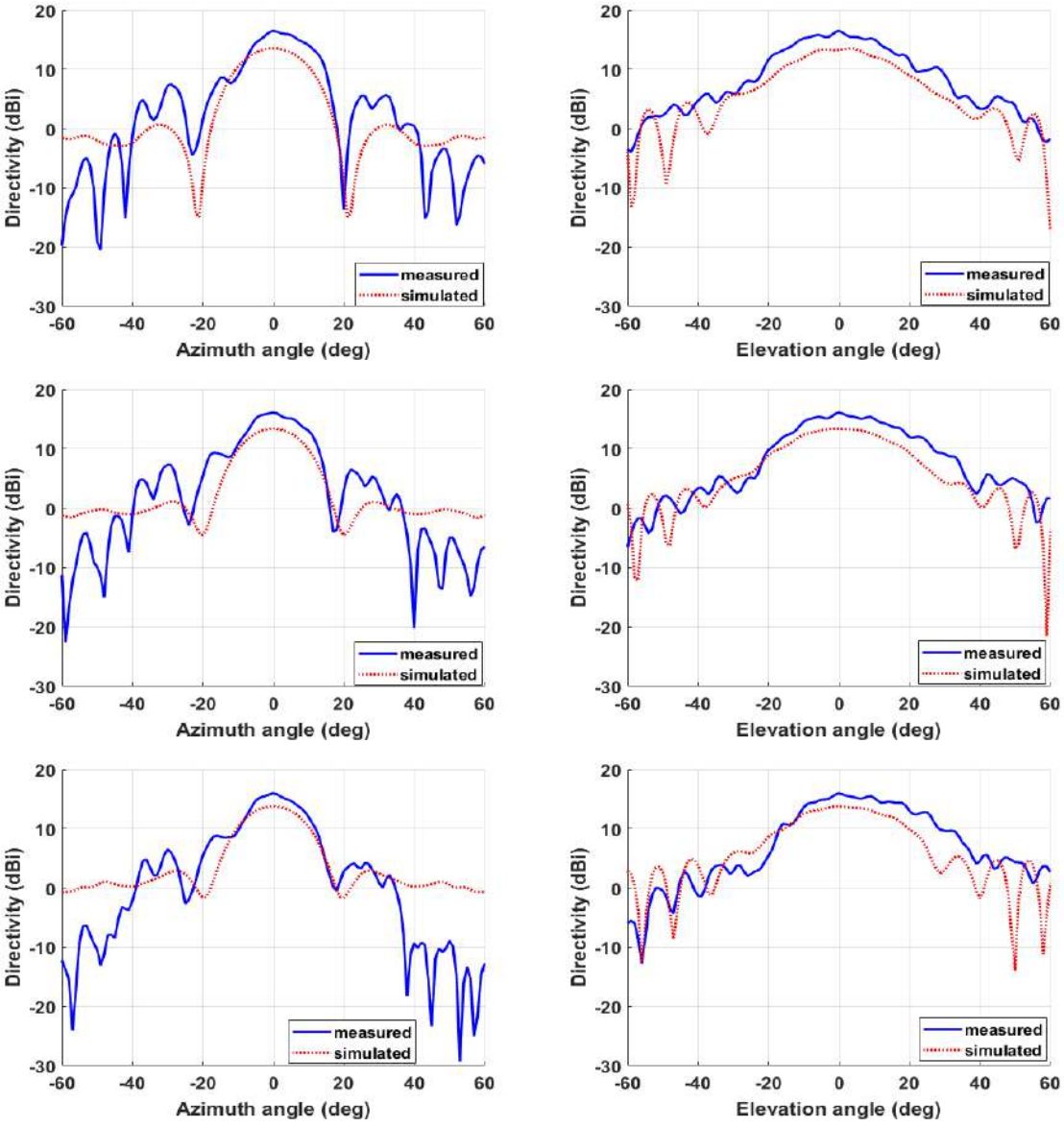


Figure 5.12: The E-plane (left column) and H-plane (right column) directivity radiation patterns of the fabricated Valentine antenna at 3.5 GHz (top), 3.8 GHz (middle) and 4 GHz (bottom).

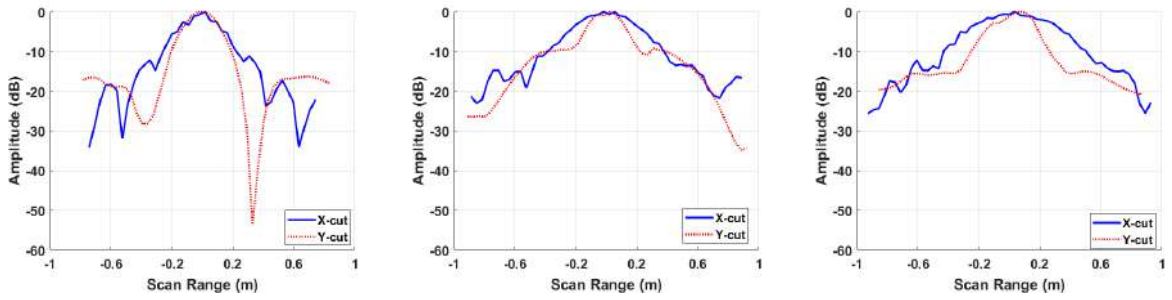


Figure 5.13: X-cut and Y-cut co-polarised near-field amplitude measurements of DRGH (left), TEM horn (middle) and Valentine (right) antennas at 4 GHz over the scan area

The planar scans depict a good agreement between the measured and the simulated radiation patterns for the three antennas. The following section compares the simulated realized gain of the three antennas to those measured.

## 5.3 Gain

### 5.3.1 Simulation

The three antennas all have simulated gain of at least 4 dBi at the designed low frequency limit of 200 MHz. The simulated realized gain of the three antennas are compared in Figure 5.14. The TEM horn antenna has comparably high gain at 500 MHz compared to the other two antennas, about 4 dB higher. However, the gain deteriorates at high frequencies for both the TEM horn antenna and the Valentine, where the TEM horn antenna has the lowest of about 11.7 dBi at 4 GHz compared to 16 dBi of the DRGH antenna.

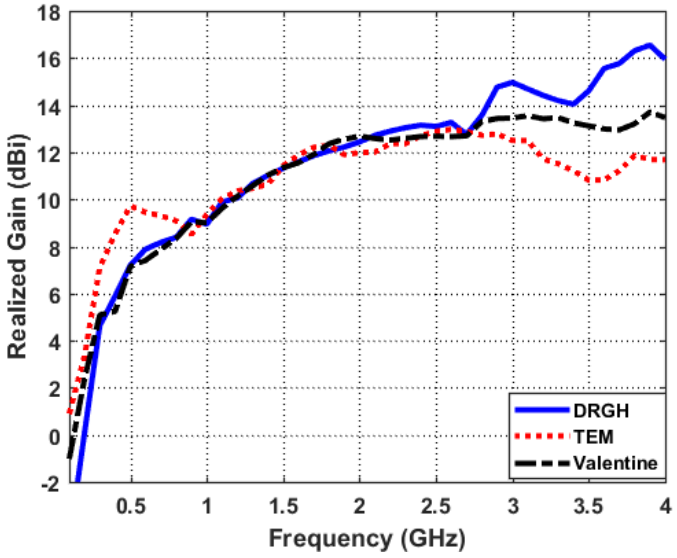


Figure 5.14: The simulated realized gain of the three fabricated antennas, compared to each other. The TEM horn antenna has the highest gain below 1 GHz while the DRGH has the highest gain above 2.5 GHz.

### 5.3.2 Measurements

In order to accurately measure the gain of these antennas to within 1 dB error [42], the gain measurements need to be done in the radiating far-field region, also known as the Fraunhofer zone, where the angular field distribution of the antenna is independent of the distance from the antenna. This far-field distance should be greater than $r$, calculated

by [8],

$$r = \frac{2D^2}{\lambda}, \tag{5.1}$$

where $D$ is the largest dimension of the antenna and $\lambda$ is the wavelength. Far-field distances of the three antennas at the frequencies of interest are calculated as shown in Table 5.1. As shown in the table, the far-field distances required for these antennas to cover the whole band up to 4 GHz is at least 26.67 m for the Valentine antenna whose largest dimension is 1 m, 11.27 m for the DRGH and 17.93 m for the TEM horn. An improved measurement accuracy of within 0.05 dB in gain measurements would require an even greater distance of $32D^2/\lambda$ [43]. Determining the gain of these antennas poses a great challenge because of their size and bandwidth. A distance of $32D^2/\lambda$ will be impractical for these antennas. The measured gain of standard pyramidal horn antennas, if done at a distance less than $32D^2/\lambda$, can be corrected using the gain correction method described in [42]. In addition, carefully determining the actual phase centre of the antenna under test reduces the variation in gain with the measurement distance [43]. To determine the gain of the three antennas, two methods, a time domain technique and the three-antenna frequency method were investigated.

Table 5.1: Far-field distance, $r = 2D^2/\lambda$, calculations for the three antennas.

| | | **DRGH** | **TEM** | **Valentine** |
|---|---|---|---|---|
| **D (m)** | | 0.65 | 0.82 | 1.00 |
| **f (GHz)** | **$\lambda$ (m)** | **Far-field distance, $r$ in metres** | | |
| 0.20 | 1.50 | 0.56 | 0.90 | 1.33 |
| 0.30 | 1.00 | 0.85 | 1.34 | 2.00 |
| 0.40 | 0.75 | 1.13 | 1.79 | 2.67 |
| 0.50 | 0.60 | 1.41 | 2.24 | 3.33 |
| 1.00 | 0.30 | 2.82 | 4.48 | 6.67 |
| 2.00 | 0.15 | 5.63 | 8.97 | 13.33 |
| 3.00 | 0.10 | 8.45 | 13.45 | 20.00 |
| 4.00 | 0.08 | 11.27 | 17.93 | 26.67 |

#### 5.3.2.1 Three-antenna method

The three-antenna measurement method, a frequency domain method, was investigated since it would allow gain characterization of the three antennas, without a prior knowledge of any of their gain. The three antennas, the DRGH, the TEM horn and the Valentine antennas would be used in the three-antenna method to determine their bore-sight gain. The three antennas would be paired up in twos as shown in Figure 5.15, the Valentine and the TEM horn in setup 1, the Valentine antenna and the TEM horn antenna for setup 2

and finally the TEM horn and the DRGH antennas in the third setup. An experimental setup of measurement, for each pair of the antennas, is as shown in Figure 5.16.

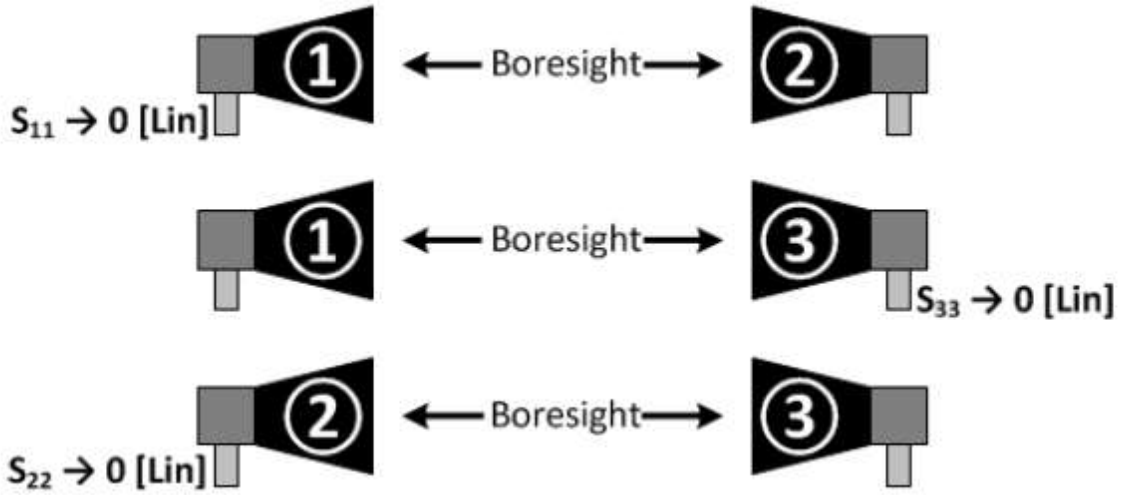


Figure 5.15: Set-up for determining gain of three antennas using the three-antenna method [44].

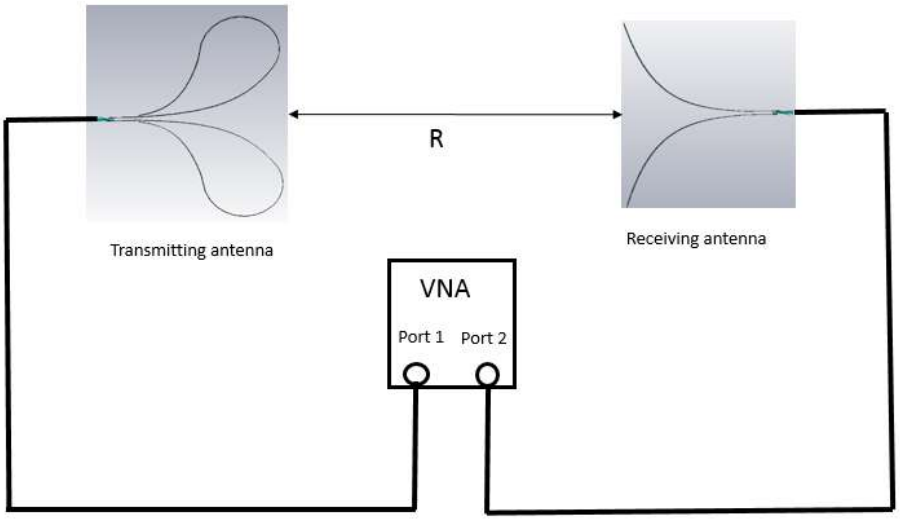


Figure 5.16: Set-up for each pair of antennas for determining gain of three antennas using the three-antenna method

The gain of the three antennas under test can then be calculated using a set of three equations which are a form of Friis transmission formula [45]. These equations are given

by

$$\begin{aligned} G_{1\text{ dB}} + G_{2\text{ dB}} &= 20\ \log_{10}\left(\frac{4\pi R}{\lambda}\right) + 10\ \log_{10}\left(\frac{P_{r2}}{P_{t1}}\right)^{\text{Setup 1}}, \\ G_{1\text{ dB}} + G_{3\text{ dB}} &= 20\ \log_{10}\left(\frac{4\pi R}{\lambda}\right) + 10\ \log_{10}\left(\frac{P_{r3}}{P_{t1}}\right)^{\text{Setup 2}}, \\ G_{2\text{ dB}} + G_{3\text{ dB}} &= 20\ \log_{10}\left(\frac{4\pi R}{\lambda}\right) + 10\ \log_{10}\left(\frac{P_{r3}}{P_{t2}}\right)^{\text{Setup 3}}, \end{aligned} \tag{5.2}$$

where $R$, is the separation distance between the antennas and antenna 1 is the Valentine antenna, antenna 2 is the TEM horn antenna and antenna 3 is the DRGH antenna. By measuring the transmission coefficient, $S_{21}$, at the receiving antenna, the three equations can be solved for the three unknowns, $G_1$, $G_2$ and $G_3$, which are the desired gains of the three antennas.

The range, the separation distance between the antennas would be chosen to provide far-field distance for all the three antennas. A far-field distance, $R$ of at least 26.67 m, the far-field distance of the Valentine (largest antenna of the three) at 4 GHz according to Table 5.1, was chosen to ensure that all the three antennas are in their far-field region for accurate measurements. Because of the required large range of at least 26.67 m, these measurements can only be performed outdoors due to the limited size of the anechoic chamber available. However, outdoor measurements come with additional challenges such as weather and other environmental effects from the surroundings. IEEE standard test procedures for antennas [45] suggest two methods to combat ground reflections that come with outdoor measurements through the use of well-designed elevated and reflection ranges [46][8]. For an elevated range, both the receiving and the transmitting antennas need to be raised above the ground by a height of at least four times the diameter of the antenna under test [45]. This would require at least a 4-metre height for the Valentine antenna. For the reflection range method illustrated in Figure 5.17, the height of the two antennas in a measurement setup can be determined by adjusting the height of the transmitting antenna until reflections from the ground are minimized [46]. In this reflected range design, the transmitting antenna should be mounted at a height, $h_t$, that is approximated by

$$h_t \approx \frac{\lambda R}{4h_r}, \tag{5.3}$$

where R is separation distance between the two antennas and $h_r$ is the height of the receiving antenna which for accurate results should be greater than $4D$. The required heights for both of these range designs are impractical and required more planning and specialized equipment than was readily available in the University lab, especially mounting masts for such heights. The antennas had also not been fixed with mountable bases, such as holes for mounting them on a tripod stand.

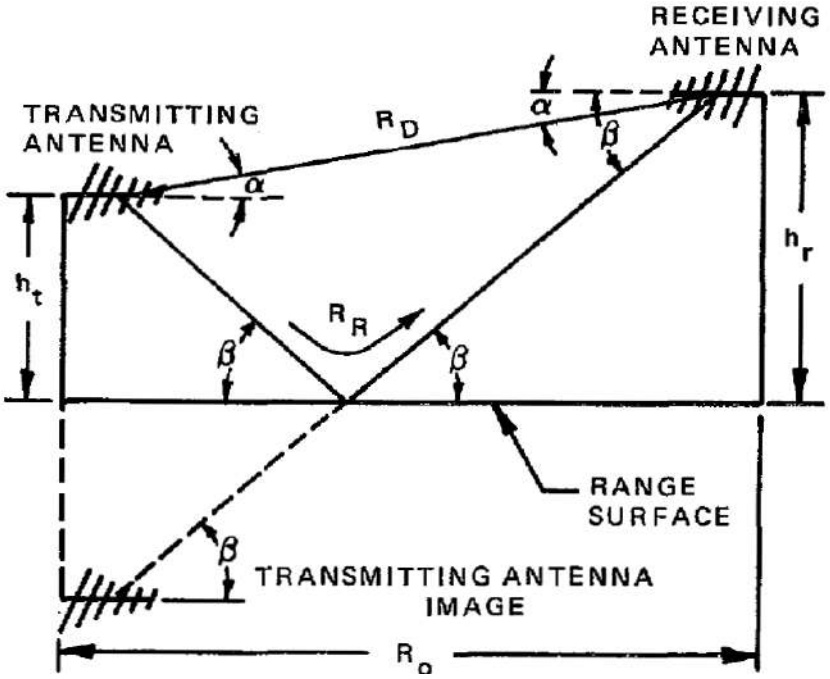


Figure 5.17: Design for a ground reflection range, the height of the transmitting and the receiving antennas are to be determined to limit ground reflections received by the receiving antenna [46].

#### 5.3.2.2 Time Domain Method

To get a preliminary characterization of the antennas' gain, time domain measurements described in [47] were done in the near-field inside the anechoic chamber. The distance of measurement was limited to 5 m by the size of the chamber. An initial attempt to perform these measurements on a roof-top as discussed in Appendix B was not successful. A lot of reflections in the roof-top measurements were noticed which were attributed to the metallic stand used for the measurements and a later realization that there was an the underlying copper material on the roof. Because of the measurements being done in the near-field, the gain obtained from this method would need to be corrected using a similar approach as the gain correction method described in [42]. The range of the measurements will also need an accurate calculation by precise determination of the phase centres of the antennas because of the wideband nature of the antenna measurements. The low frequency signals are expected to be radiated close to the antenna aperture while the high frequency signals are expected to radiate closer to the antenna feed.

In this method, a conducting reflection target of comparable size to the antenna is placed in front of an antenna at a distance, R, as shown in Figure 5.18. Rectangular plates were used because of readily available sizes although a circular plate and a spherical ball were also attempted as shown in Appendix B.

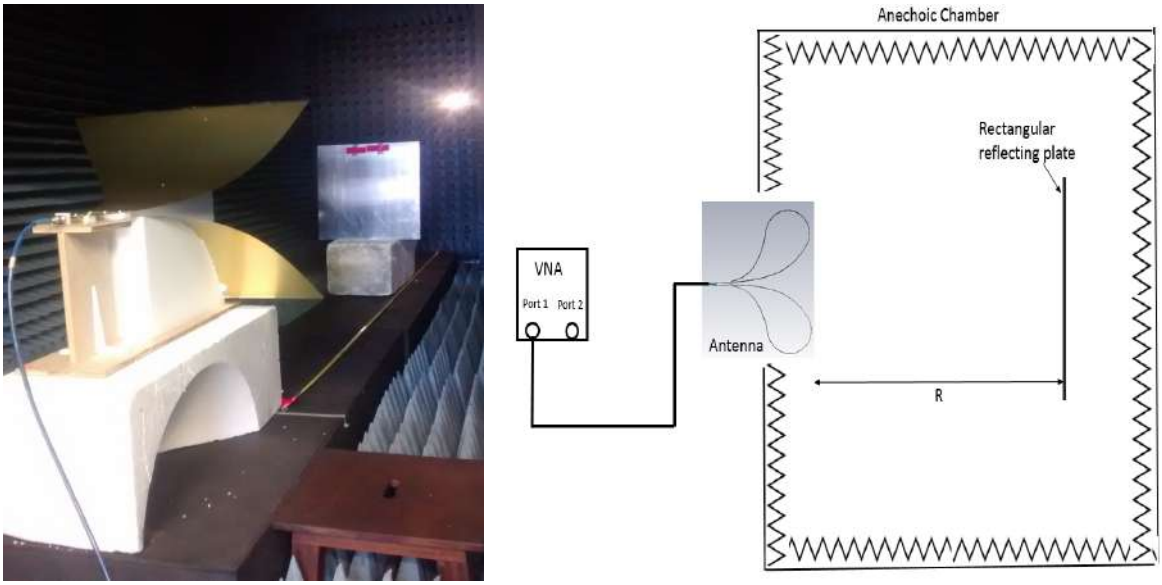


Figure 5.18: Time domain gain measurement set-up inside anechoic chamber with a rectangular plate placed at distance, R, from the antenna aperture. The size of the plate should be comparable to the size of the antenna.

A vector network analyzer (VNA) was used to capture the reflection coefficient of the antenna without a reflecting target in front of it. With the plate in front of an antenna and using the Inverse Fourier Transform (IFT) feature of the VNA, the reflected signal off the plate was monitored in time domain as shown in Figure 5.19. Using the time-gating feature to isolate only the reflected signal from other responses, a frequency response of this reflection coefficient, $S'_{11}$, was obtained. The reflection coefficient, $S_{11}$, without the plate and the reflection coefficient with the plate in front of the antenna, $S'_{11}$, are then used to calculate gain using the Radar Range Equation [47]. Gain is given by,

$$G = \frac{|S'_{11}|}{(1-|S_{11}|)^2}\frac{8R^2}{\lambda}\sqrt{\frac{\pi^3}{\sigma}}, \tag{5.4}$$

where R is the range, that is, the distance from the target to the antenna aperture, $\lambda$ is wavelength, and $\sigma$ is the Radar Cross Section (RCS), calculated by [48],

$$\sigma = \frac{4\pi a^2}{\lambda^2}, \tag{5.5}$$

for a rectangular plate, where a is the area of the plate.

Plates with sizes comparable to the size of each of the antenna were used for these measurements. A plate of dimensions 75 cm by 64.3 cm was used for the TEM horn, as this was the closest size to the 80-cm square aperture of the antenna. An optimum range of 4.7 m was also chosen, that is, the distance from the antenna aperture to the plate. The distance was determined by choosing the maximum distance where a distinct reflected signal from the plate was detected by the VNA. A noisy reflected signal would lead to loss of information especially at the low frequencies. The reflected signal was centred at

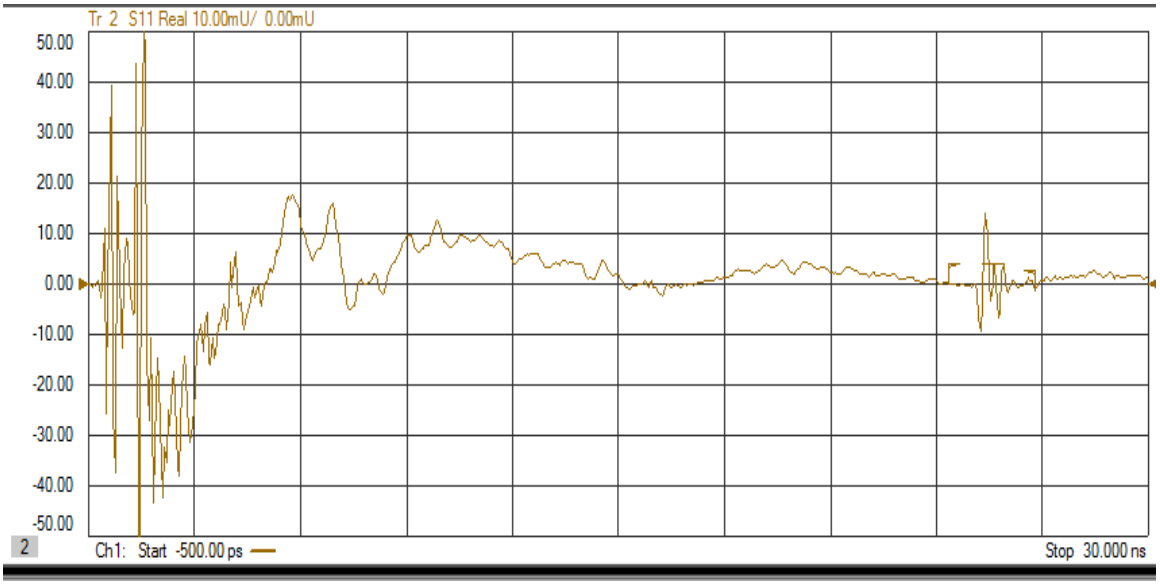


Figure 5.19: Time domain representation of the reflected signal on the VNA, seen close to 30 ns, due to the reflecting plate placed in front of the antenna. This reflected signal is time-gated and the resulting frequency domain reflection coefficient is recorded.

37.34 ns and a time-gating span of 3 ns was applied. For the DRGH, a range of 3 metres was used. A square plate of dimensions 62.1 cm by 62.1 cm was used as the reflection target for the DRGH measurements. This was a comparable size to the aperture of the DRGH (53.6 cm by 43.0 cm). A time-gating window was chosen with a span of 2.51 ns and centred at 25.54 ns. Time-gating windows were chosen appropriately to include all the reflected signals, so as not to lose any signal information and not too large to include noise. Similarly, a plate of size 82 cm by 67 cm was used with the Valentine antenna.

Because of the wideband nature of these antennas, the calculated gain from measurements is expected to vary with the actual gain of the antenna because of the location of the real phase centre of these antennas at the various frequencies. The phase centres of the antennas are expected to be close to the aperture at the low frequencies and to be closer to the feed at high frequencies. It is, therefore, important that the exact phase centres of the antennas be accurately determined in order to perform the gain calculations correctly. The phase centre of an antenna is defined as the position that approximates the centre of curvature of the waves radiating from the antenna [7]. Muehldorf [49] describes the calculation of phase centres of rectangular and diagonal horn antennas which cannot be easily applied to the three antennas described in this thesis. There doesn't exist a known theoretical approach for calculating the phase centres of the DRGH, TEM horn and the Valentine antennas. CST Studio Suite, however, provides a method that can be used to determine the phase centres of these antennas.The phase centre can be calculated using a far-field post-processing step of the Finite Integral Method (FIM) solver in CST Studio Suite. H-plane as well as the E-plane phase centres of these antennas can be determined. Phase centres of the three antennas were calculated by first analysing the

phase pattern of the antennas. An angle about the bore-sight axis was determined by choosing an angle that minimized the change in the phase pattern around the bore-sight axis. An angle of $1^o$ was chosen for all the three antennas, as this gave the least phase pattern variation, and thus the least error in the phase calculation.

Figure 5.20 shows the E-plane, the H-plane and the averaged phase centres of the three antennas calculated using CST Studio Suite, as well as the standard deviation (error) in the calculated phase centre. As predicted, the simulated phase centres of these antennas vary with frequency. Based on the average value of both the E-plane and the H-plane centres, the phase centre of the DRGH moves away from the aperture as frequency increases. However, beyond 2.6 GHz, the phase centre becomes unstable and is located outside the antenna. From the 3D radiation patterns in Appendix E, it is shown that the main lobe of the radiation splits beyond 2.6 GHz making the phase centre hard to determine. The standard deviation in Figure 5.20 shows that the error of phase centre calculation increases at these frequencies. The calculated E-plane phase centre is more reliable than the calculated H-plane centre. For both the TEM horn and the Valentine antennas, the error of the E-plane phase centre is very large compared to that of the H-plane. The absence of the H-plane walls and the complex geometry of the three antennas make the phase centre more difficult to determine compared to a conventional horn antenna. The magnitude of error of the E-plane being much greater than the H-plane error would probably be attributed to the geometry of the antennas and particularly the difference in the H-plane and E-plane geometries and related radiation patterns. Phase centre calculations rely on fitting of a constant function through the radiation pattern phase in a given sector. If the amplitude of the pattern is not smooth in that sector, the calculation becomes difficult (or even meaningless). Because of the large error in the E-plane, the H-plane phase centre calculation is more reliable and can be used as estimate of the actual phase centre. Based on the H-plane phase centre, it is also evident that the phase centre of the Valentine antenna moves toward the feed as frequency increases and is about 55 cm from the aperture at 4 GHz. The phase centre of the TEM horn antenna fluctuates at the different frequencies, but there is also a trend that the phase centre moves away from the aperture as frequency increases. The measured gain from the time domain method was first calculated without taking the actual phase centre into consideration. Figure 5.21 shows the calculated gain of the TEM horn antenna and the DRGH compared to those simulated. The measured gain was then calculated using the phase centres determined from CST Studio Suite. The results of this range correction are shown in Figure 5.22. This range correction improves the measured gain by an average of about 2 dB for the TEM horn antenna and an average of about 1 dB for the DRGH antenna. The gain is, however, not improved beyond 2.6 GHz for the DRGH because of the unreliable phase centre.

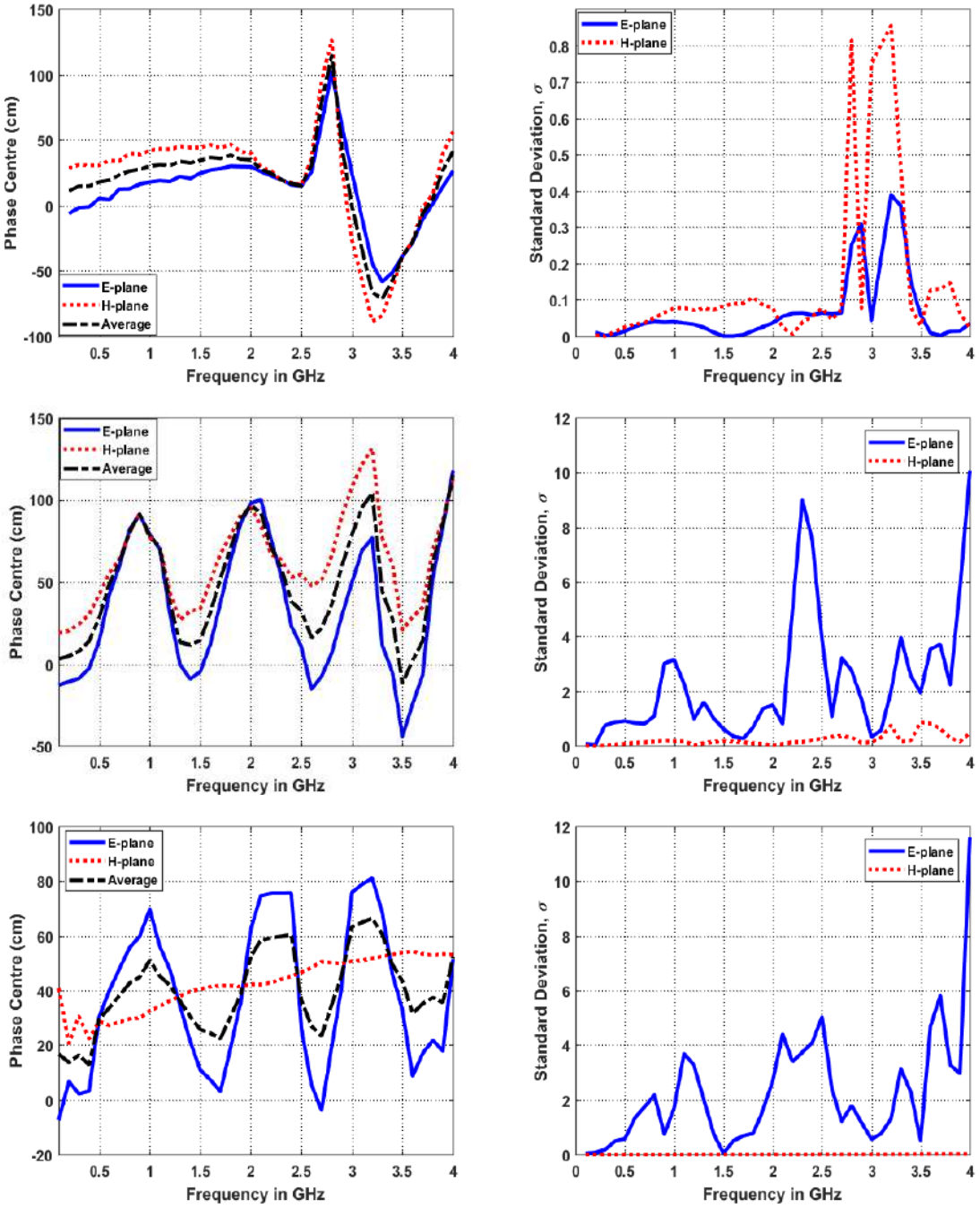


Figure 5.20: CST Studio Suite-calculated bore-sight phase centre (distance from antenna aperture) in the E-plane, H-plane and their average (left column) for the DRGH (top), TEM horn (middle), and Valentine (bottom) antennas and the corresponding standard deviation error in both planes (right column). A scan angle of 1 deg was used to minimize the error in phase pattern.

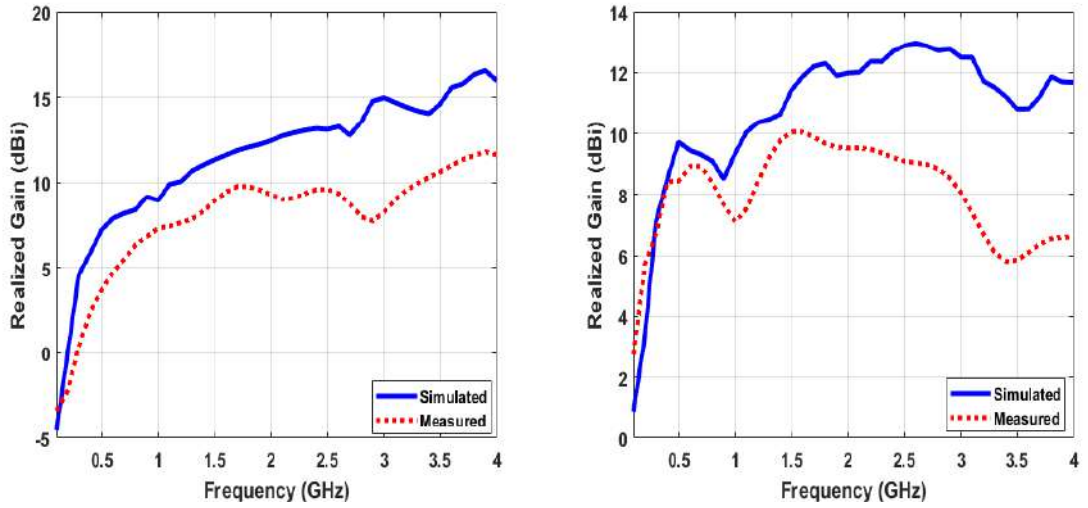


Figure 5.21: The calculated time domain gain measurement for the DRGH (left) and TEM horn (right) antennas using the distance from the antenna aperture to the rectangular plate as the range. The measured gain is much lower than the simulated gain, especially at high frequencies where the far-field distance requirement is not met.

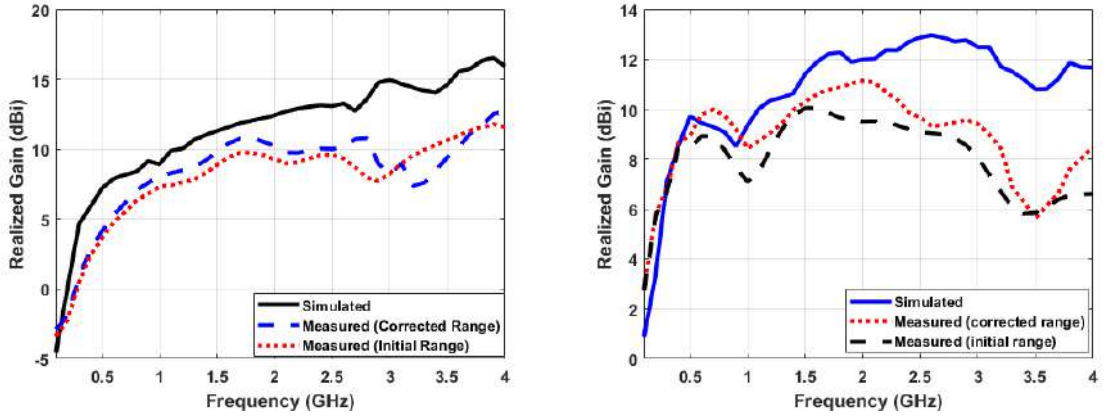


Figure 5.22: The measured gain compared to the simulated gain, calculated using phase centre-corrected range from CST Studio Suite simulation, for the DRGH antenna (left) and for the TEM horn antenna (right).

As noted, the measured gain, even with the corrected range, is much lower than the anticipated gain from simulation. The measured gains of the two antennas suffer deterioration especially at high frequencies where the far-field criterion is not met. At 4 GHz, the DRGH measurements at 3 m and the TEM horn antenna measurements at 4.7 m are only a small fraction of the required range of $2D^2/\lambda$, for obtaining gain within 1 dB [42]. From this method, we expect accurate gain results, only where the far-field distance criterion of the antenna as well as the far-field distance of the plate used is met [47]. As highlighted in Table 5.1 and Table 5.2, the far-field criterion for both antenna and plate are met for Valentine antenna measurements at 5 m for frequencies up to 400

MHz, for the DRGH measurements at 3 m for frequencies up to 500 MHz and for the TEM horn antenna measurements at 4.7 m measurements for frequencies up to 500 MHz. We expect the gain measurements calculated with the phase-centre corrected range, to be within 1 dB accurate below these frequencies.

Table 5.2: Far-field distance, $r = 2D^2/\lambda$, calculations for the three plates used.

| | | **Plate A (DRGH)** | **Plate B (TEM horn)** | **Plate C (Valentine)** |
|---|---|---|---|---|
| **Largest dimension D (m)** | | 0.621 | 0.75 | 0.82 |
| **f (GHz)** | **$\lambda$ (m)** | **Far-field distance, $r$ in metres** | | |
| 0.20 | 1.50 | 0.51 | 0.75 | 0.90 |
| 0.30 | 1.00 | 0.77 | 1.13 | 1.34 |
| 0.40 | 0.75 | 1.03 | 1.50 | 1.79 |
| 0.50 | 0.60 | 1.29 | 1.88 | 2.24 |
| 1.00 | 0.30 | 2.56 | 3.75 | 4.48 |
| 2.00 | 0.15 | 5.13 | 7.50 | 8.97 |
| 3.00 | 0.10 | 7.69 | 11.25 | 13.45 |
| 4.00 | 0.08 | 10.25 | 15.00 | 17.93 |

The TEM horn antenna measurements agree with the simulations to within 1 dB for frequencies lower than the mentioned 500 MHz. The DRGH measurements, however, deviate from the simulated measurements, with a deviation of almost 3 dB at 500 MHz, however, the shape of the graph is similar to that simulated. For the Valentine antenna, the measurements obtained were not satisfactory even at low frequencies. The plate used, which was the largest available at that time, was smaller compared to the antenna aperture. The results obtained for this antenna with this plate size are shown in Section B.4 of Appendix B.

For the high frequency deterioration caused by measurements being in the near-field, Chu and Semplak [42] give equations to correct measured gain of pyramidal horn antennas as a function of horn geometry and the range, $R$, of measurement. Gain measurements need to be corrected because of the often limitation of not being able to measure gain in the required far-field distance [42]. By using equations in [42] as described in Appendix C, Section C.2, it is noted that a pyramidal horn antenna with the same waveguide and horn aperture dimensions as the fabricated DRGH suffers a gain deterioration of 2.41 dB at 4 GHz when measured at a range of 3 m as was done for the time domain measurements of a DRGH. Although, there are no known techniques to determine the deterioration of gain for these specific antennas, we expect that the gain will reduce by a significant magnitude. The gain correction factor calculated for a pyramidal horn antenna with same dimensions as the DRGH is plotted against frequency in Figure 5.23. When this correction factor

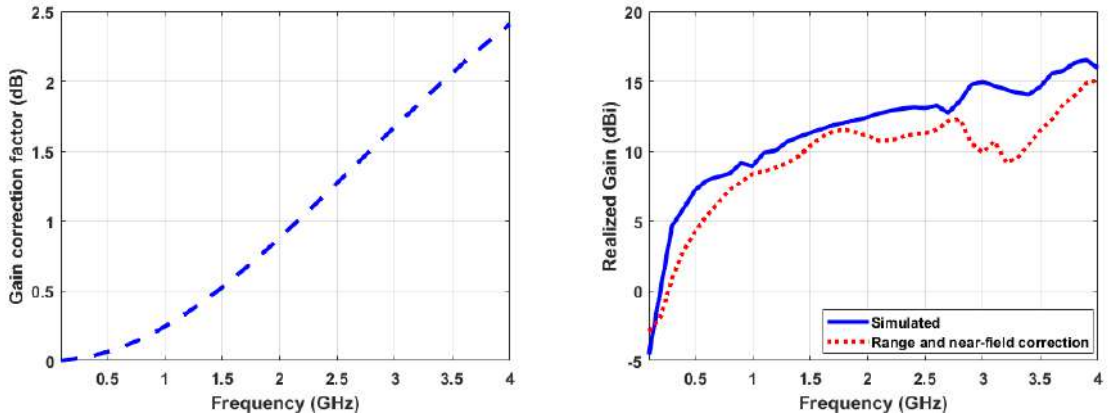


Figure 5.23: (Right) The near-field correction factor calculated for measurements done at 3 m for a pyramidal horn antenna with similar dimensions as the DRGH. The gain deteriorates by 2.41 dB at 4 GHz. (Left) The measured gain calculated using both the corrected range and by adding Semplak and Chu's near-field correction factor [42].

is used on the measured gain for the DRGH antenna, the gain is improved and closely replicates the simulated gain as shown in the right column of Figure 5.23. Besides the gain deterioration observed in the time domain measurements for both the TEM horn antenna and the DRGH, it is still evident that the gain of the antennas increase with frequency. The trend of the measured gain of the fabricated antennas is similar to that simulated.

## 5.4 Conclusion

In this chapter, the performance of the three antennas, in terms of the reflection coefficient, radiation patterns and the realized gain, has been presented and discussed. It has been shown that the simulated results can be replicated by measuring the fabricated antennas. In the following chapter, Chapter 6, the three antennas that were fabricated and measured will be optimized to further improve the reflection coefficient.

# Chapter 6

# Parametric Study and Optimization

The simulated results obtained in Chapter 5 can be improved through a parametric study and optimization. This chapter presents the results of an initial parametric study done in CST Studio Suite for the reflection coefficient of the DRGH antenna and the coaxial to parallel-plate transition. The optimization of the reflection coefficient of the three antennas using Surrogate Modelling (SUMO) toolbox [50] is then described and the results of the optimization are presented. Some of the results presented here have already been presented in [40].

## 6.1 Parametric Study

Initially, a basic parametric study of the three antennas in CST Studio Suite was done to observe the effect of the different parameters on the reflection coefficient.

### 6.1.1 Reflection Coefficient of DRGH antenna

A complete assembly of the DRGH, including both the back cavity and the flared section, was studied for the reflection coefficient. The parameters of the back cavity of the DRGH were observed to influence the reflection coefficient of the antenna. The reflection coefficient could be improved by changing the parameters of the ridged back-cavity shown in Figure 3.4. Increasing $br$, the radius at which the end edges of the ridges inside the waveguide are rounded with, was observed to improve the reflection coefficient at the 2.75 GHz where there is a mismatch as shown in Figure 6.1. However, there is a limit of how much the radius can be increased to, as this shortens the ridges inside the waveguide. An optimum length for the ridges is required to provide enough and manufacturable space for the coaxial feed. The reflection coefficient can also be improved by decreasing $fdi$, the distance from the edge of the ridges to the centre of the coaxial feed, and by increasing the end diameter of the tapering inner coaxial conductor (between the ridges), $de$, as shown in Figure 6.1. The dimensions of the wedges, wedge length, $wl$, and wedge height,

$wh$, also affect the reflection coefficient, with a varying effect at the different frequencies as shown in Figure 6.1.

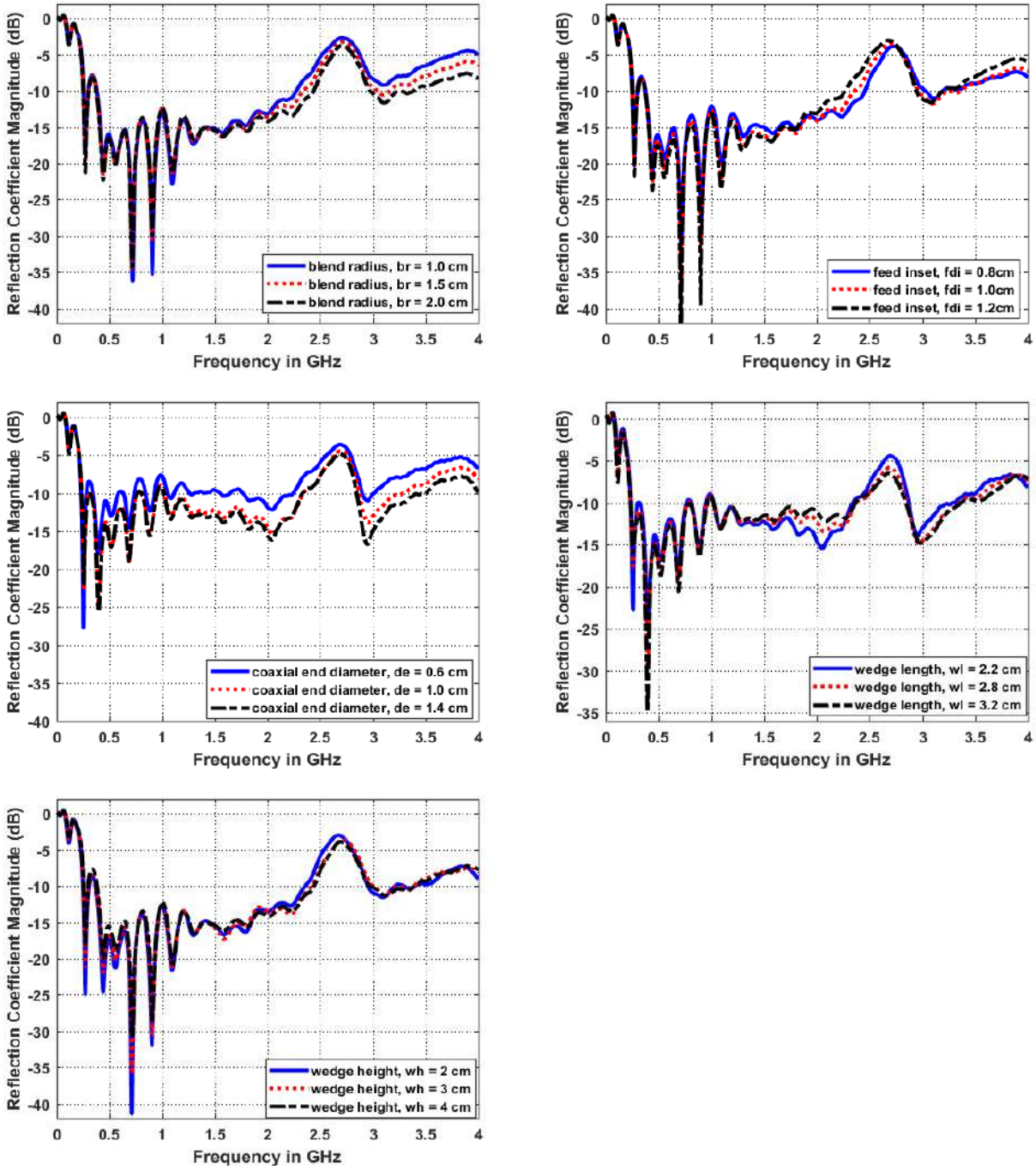


Figure 6.1: Effect of blend radius, feed inset, inner coaxial conductor end diameter, wedge length and wedge height of the back cavity on the reflection coefficient of the DRGH.

The dimensions of the waveguide: the height, $b$, and the width, $a$, as well as the ridge width, $a_0$, and the ridge separation distance, $b_0$, can be modified to improve the bandwidth by changing the cut-off frequency of the next higher mode as shown in Figure 6.2. In addition, the length of the waveguide, $c$, shown in Figure 3.4, is also seen to affect

the reflection coefficient and can be optimized to achieve the best matching possible. Most of these parameters are, however, limited by the possibility of manufacturing. The parameters have to be kept at reasonable dimensions that can be manufactured, for example, the separation between ridges, $b_0$, was limited to 6 mm and the feed inset, $fdi$, was limited to 8 mm.

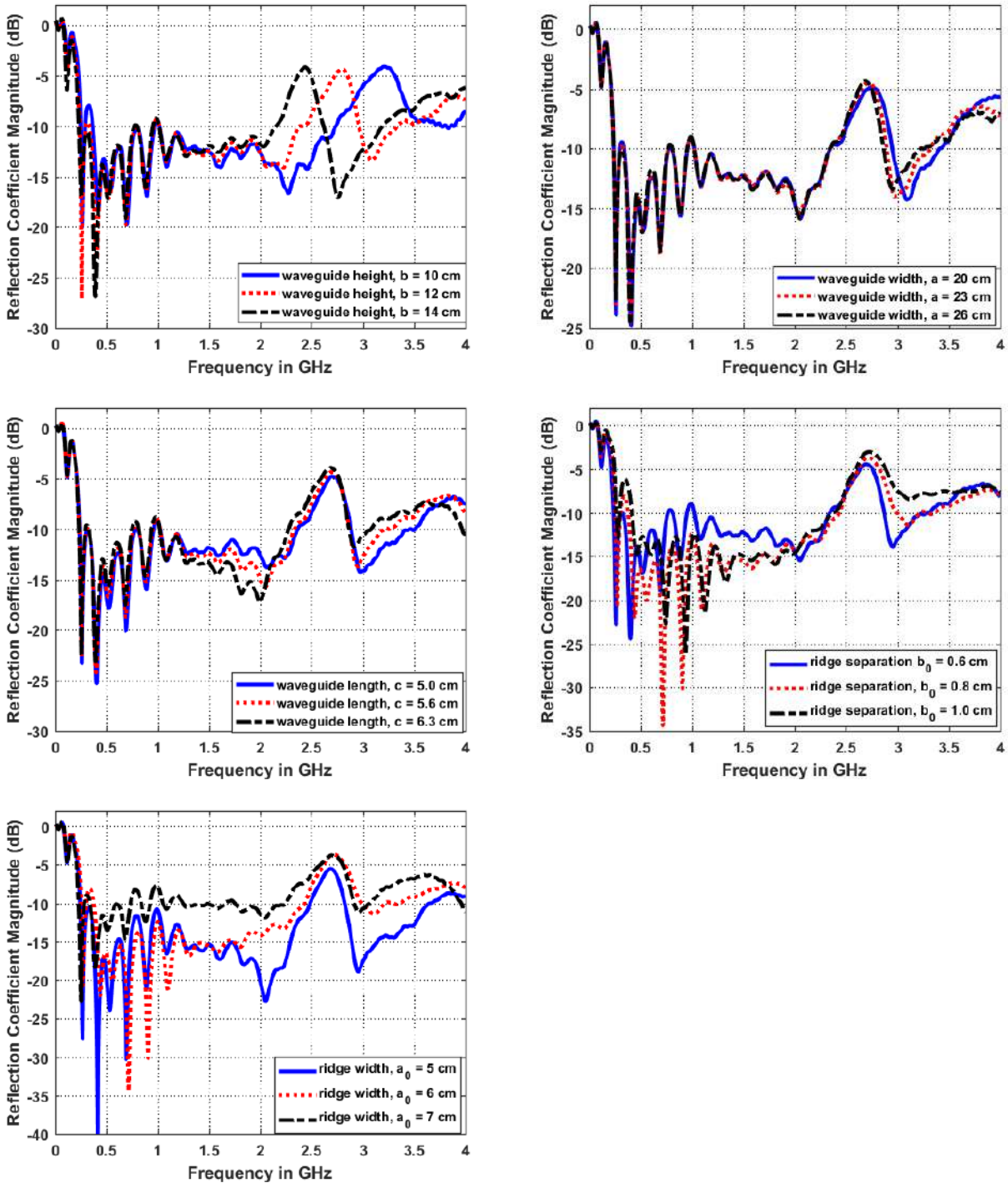


Figure 6.2: Effect of waveguide height, waveguide width, waveguide length, ridge separation distance and ridge width parameters of the back cavity on the reflection coefficient of the DRGH.

### 6.1.2 Reflection Coefficient of TEM horn and Valentine antennas

The reflection coefficient of the TEM horn and the Valentine antennas were found to depend significantly on the parameters of the coaxial to parallel-plate transition illustrated in Figure 3.10. Particularly, nine parameters of the exponentially-tapering coaxial to parallel-plate transition were noted to have significant effect on the reflection coefficient of the transition, namely: the start width of the top exponential plate, $s_t$, the start width of the bottom exponential plate, $s_b$, the length of the rectangular parallel plates, $l_p$, the length of the exponentially-tapering plates, $t_h$, the trim angle of the outer coaxial conductor, $\alpha$, the inner coaxial conductor end diameter, $d_e$, the thickness of the outer coaxial conductor, $t_c$, the length of the outer coaxial conductor, $l_c$, and the length of the tapering inner conductor extending beyond the outer conductor, $l_e$. A parametric study of these parameters on the reflection coefficient of the transition was done, as this could be directly applied to both the complete assembly of the TEM horn and the Valentine antennas.

It was noted that there is a better matching when the starting width of the top exponentially-tapering plate is wider than the starting width of the bottom plate. The variations of both starting widths of the exponential plates have an impact on the reflection coefficient. Generally, wider starting widths improve matching at the low frequencies and narrower start widths improve matching at high frequencies as shown in Figure 6.4. The length of the rectangular parallel-plate section, $l_p$, as well as the length of the exponentially-tapering plates, triangle height, $t_h$, affect the reflection coefficient of the transition. Long plates tend to improve low frequency matching while short plates improve high frequency matching. A length that balances the high frequency and the low frequency effect should be arrived at. The effect of these lengths is shown in Figure 6.4.

The thickness of the outer conductor, $t_c$, which determines the separation distance between the parallel plates of the transition, has a big influence on the reflection coefficient, particularly at low frequencies, as shown in Figure 6.3. The length of the tapering inner conductor extending beyond the outer conductor, $l_e$, greatly impacts the reflection coefficient at high frequencies with the shortest length giving better reflection coefficient as shown in Figure 6.3. The end diameter of the tapering inner coaxial conductor, $d_e$, also varies matching at different frequencies, a small diameter provides better matching at the lower frequency at the expense of a mismatch at the high frequency. Similarly, if the diameter is too large, the reflection coefficient is improved at the high frequency while the low frequency end suffers. The length of the coaxial, $l_c$, also leads to a slight variation in the reflection coefficient at different frequencies as shown in Figure 6.3 and including it in optimization could improve reflection coefficient at certain frequencies. Finally, the angle at which the outer conductor of the coaxial connector is trimmed, $\alpha$, can also be

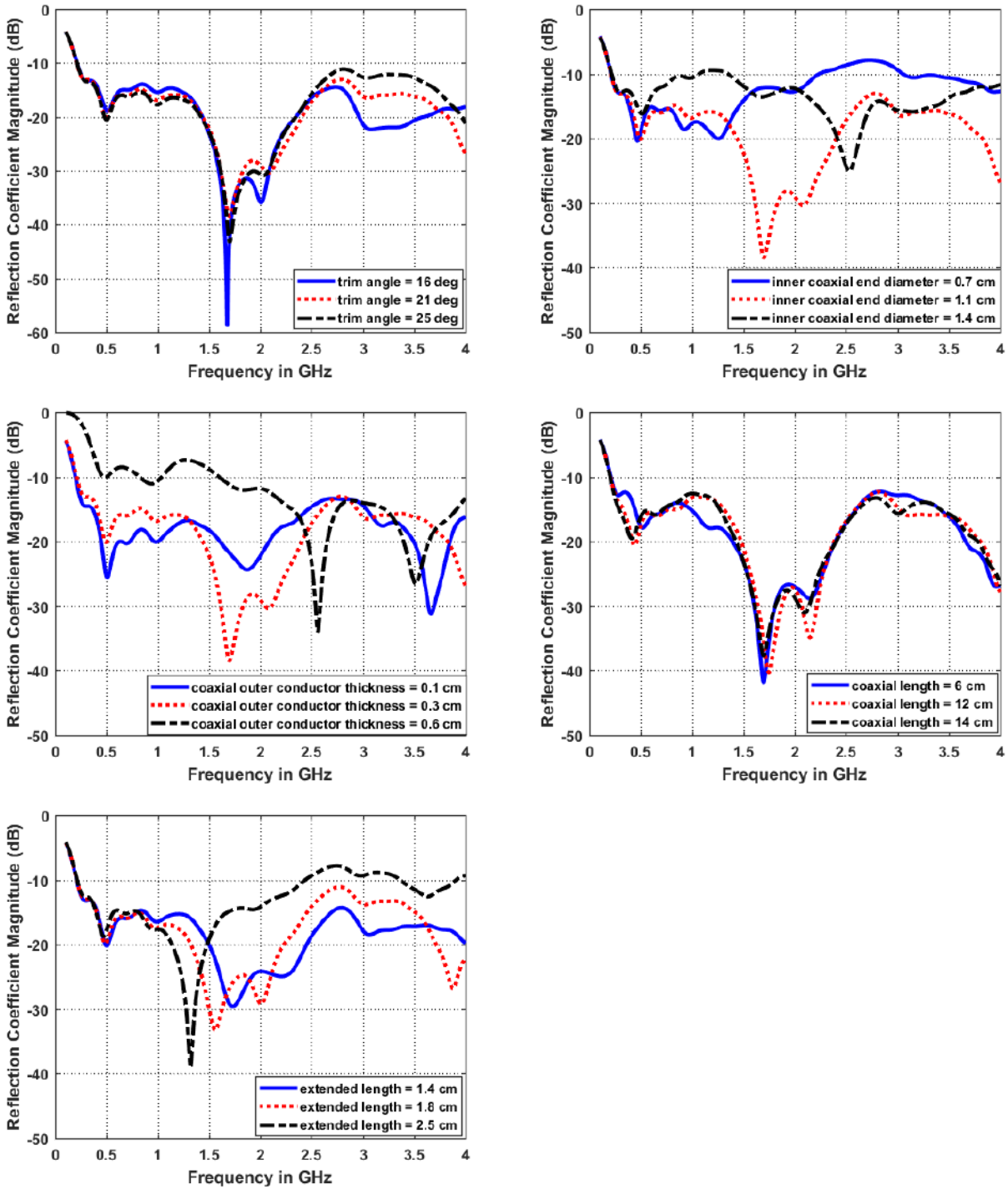


Figure 6.3: Effect of coaxial trim angle, end diameter of the tapering inner conductor, thickness of outer conductor, length of the outer conductor and length of the tapering inner conductor beyond the outer conductor on the reflection coefficient of the exponential transition.

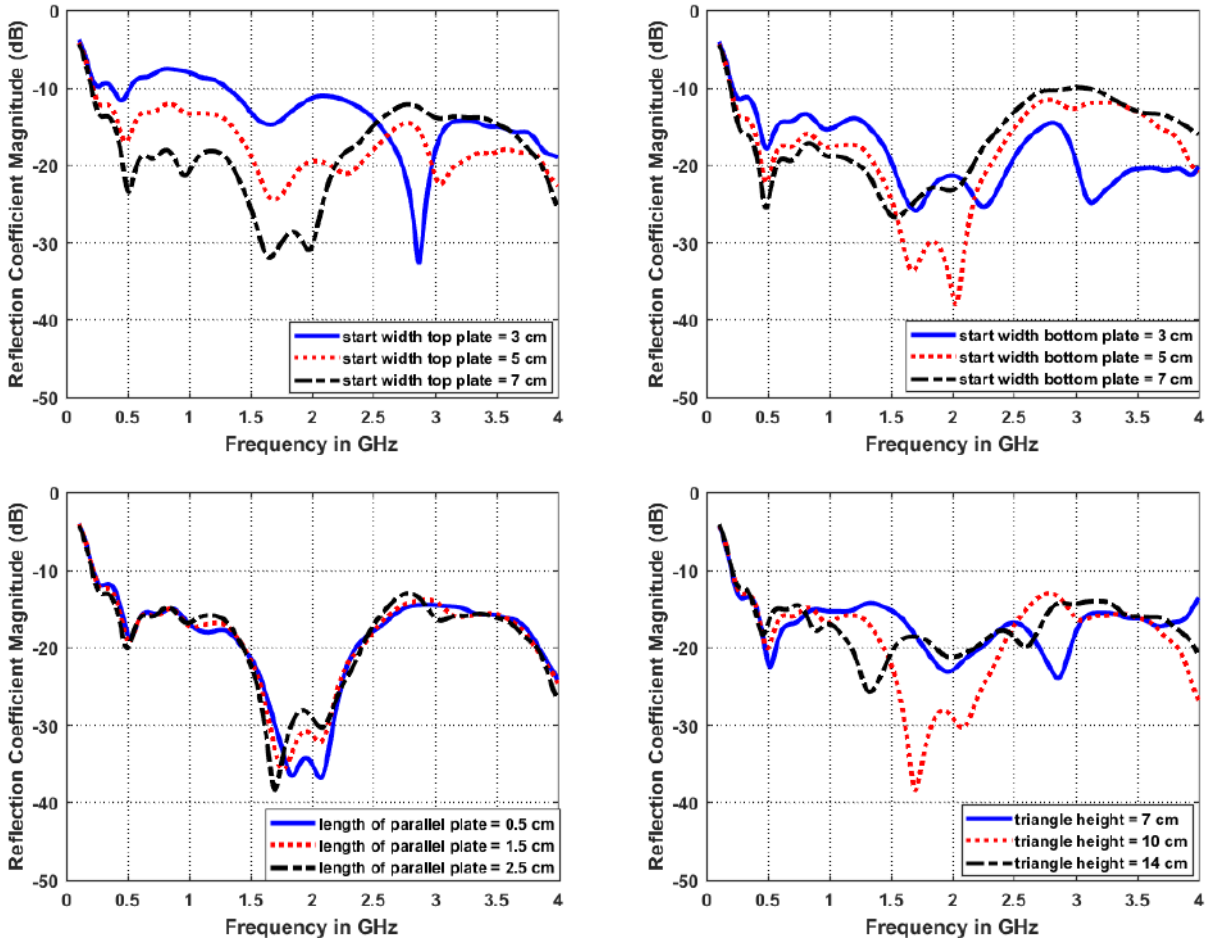


Figure 6.4: Effect of the start width of the top exponential plate, the start width of the bottom exponential plate, the length of the transition's rectangular plate section and the length of the exponentially-tapering plates (triangle height) on the reflection coefficient of the transition.

varied to improve the reflection coefficient as shown in Figure 6.4. The smallest trim angle, that is, the most gradual cut, gives the best reflection coefficient. This angle is however limited by what is possible to manufacture. The least angle that was practical for manufacturing was $20^o$.

## 6.2 Optimization

### 6.2.1 Methodology

Because of the wide bandwidth and large number of geometric parameters of the antennas, detailed design of these antenna structures through the usual supervised parametric sweeps is impractical due to the lengthy simulation times. A Surrogate-Based Optimization (SBO) technique was used to optimize the antennas' reflection coefficients. This SBO technique creates a surrogate model that approximates the response of the antenna.

Specifically, a Kriging model was employed for the reflection coefficient response surface, where the sampling is informed by standard Expected Improvement (EI). EI calculates the actual amount of improvement expected at all points in the sample space, assigning the highest value where a function changes significantly, therefore, its use as an infill sampling criterion is best for problems that aim to determine a global optimum [51]. Kriging interpolates given data points by determining the spatial correlation between the given data points and uses this correlation to predict behaviour of other points. Kriging can create models for very complex functions of up to 20 variables and 10000 data points [52]. A Latin Hypercube initial design was used to generate initial samples for the Kriging model while EI was subsequently used to find a minimum of the response surface iteratively. The right number of initial samples must be chosen to ensure the accuracy of the surrogate model built. The Latin Hypercube Sampling is used to generate random initial values of the variable using the mean and standard deviation of a variable. The design space is divided into several equal sized bins and a data sample is allocated to each bin [51]. The number of training (initial) samples needed for a given problem is generally given by [53]

$$n = 11k - 1, \tag{6.1}$$

where n is the number of initial samples and k is the number of parameters to be optimized. Figure 6.5 shows two examples of Kriging models created for a one-parameter optimization and a two-parameter optimization for the Valentine antenna. The choice of subsequent samples using EI is illustrated here, where subsequent samples are crowded at the minima of the function.

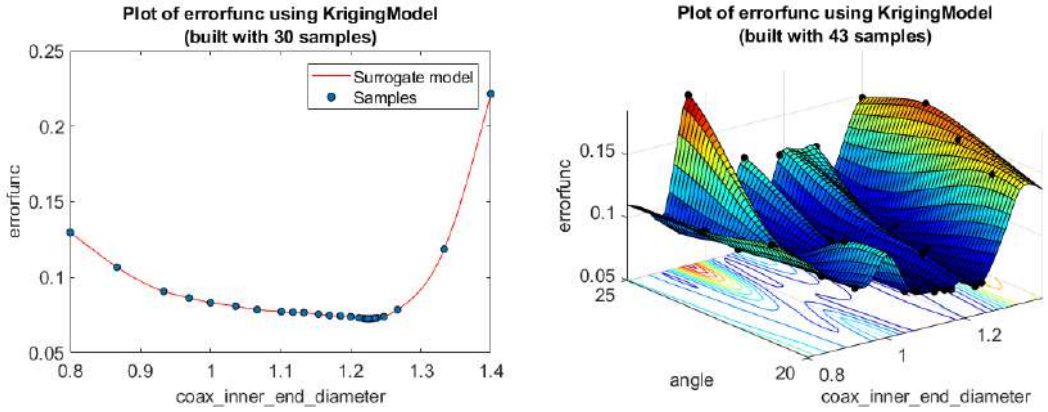


Figure 6.5: Example of a one-parameter, 1D and a two-parameter, 2D Kriging models built for the Valentine antenna optimization

Using SUMO toolbox, a single objective optimization with ten variables was set up for each antenna with a goal of return loss greater than or equal to 10 dB in the 200 MHz to 4 GHz frequency range. The response surface was defined by,

$$f_e = \frac{f_{min}}{f_{max}} + p, \tag{6.2}$$

where $f_e$ is the error function, $f_{min}$ is the minimum frequency, $f_{max}$ is the maximum frequency and $p$ is the penalty. The penalty is calculated to be directly proportional to the area of the reflection coefficient graph above -10 dB, that is, the integral magnitude of the reflection coefficient above -10 dB. This error function is minimized until the lowest possible value is obtained. For each antenna, the optimization time was set to a maximum of 50 hours or to be terminated when a maximum of 300 samples have been obtained. A plot of the error function against the number of samples is shown in Figure 6.6 for the DRGH optimization and the minimum error function is achieved after 245 samples. For the reflection coefficient to be completely below -10 dB in the required frequency range of 200 MHz to 4 GHz, the error function must be minimized to 0.05.

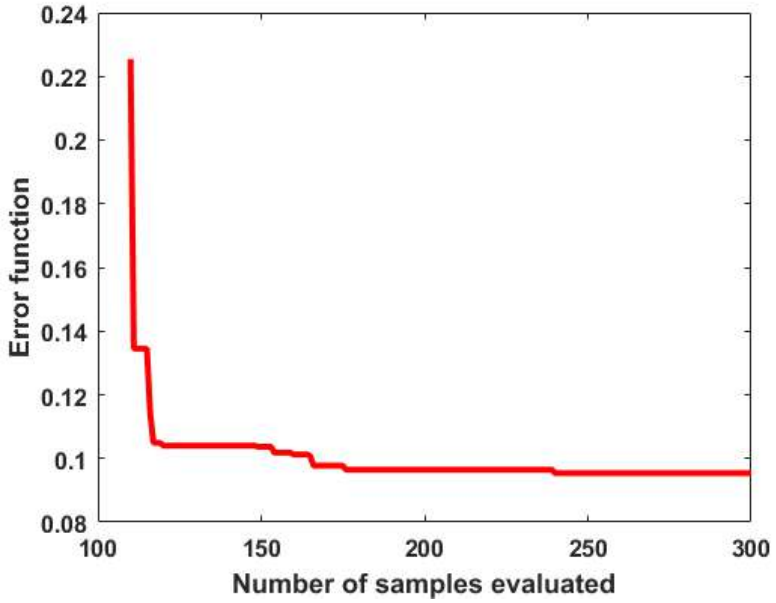


Figure 6.6: Error function with the increasing number of samples for the DRGH optimization

### 6.2.2 Reflection Coefficient of DRGH antenna

The return loss of the DRGH was found to depend significantly on ten parameters of the back cavity that were investigated in Section 6.1.1. These ten parameters were chosen for optimization as shown in Table 6.1. For manufacturability, certain limits for the parameters were set. For example, the distance of the coaxial feed pin should at least be 8 mm from the end of the ridges to allow enough space for the rest of the coaxial cable to go through the ridge. The separation distance between the ridges must also be kept at a minimum of 6 mm. The height of the wedges must not exceed half of the waveguide height, and the added length of the wedges and the ridges inside the cavity back must not exceed the waveguide length. Table 6.1 shows the initial values before optimization and the values after optimization. Figure 6.7 shows the improvement achieved by this

optimization. The optimization is able to reduce the mismatch at 2.75 GHz and improves the reflection coefficient at the low frequencies thus increasing the bandwidth ratio from the initial simulated value of 11 to 16.

Table 6.1: Initial and optimized parameters of the DRGH antenna

.

| *Symbol* | *Parameter* | *Initial (cm)* | *Optimized (cm)* |
|---|---|---|---|
| $fdi$ | feed inset | 0.90 | 0.80 |
| $wh$ | wedge height | 3.10 | 3.91 |
| $wl$ | wedge length | 2.20 | 3.20 |
| $de$ | inner coaxial end diameter | 1.00 | 1.40 |
| $br$ | ridge blend radius | 1.85 | 1.85 |
| $b_0$ | ridge separation | 0.60 | 0.60 |
| $a_0$ | ridge width | 6.00 | 5.28 |
| $b$ | waveguide height | 12.40 | 11.87 |
| $c$ | waveguide length | 5.50 | 5.87 |
| $a$ | waveguide width | 24.80 | 23.00 |

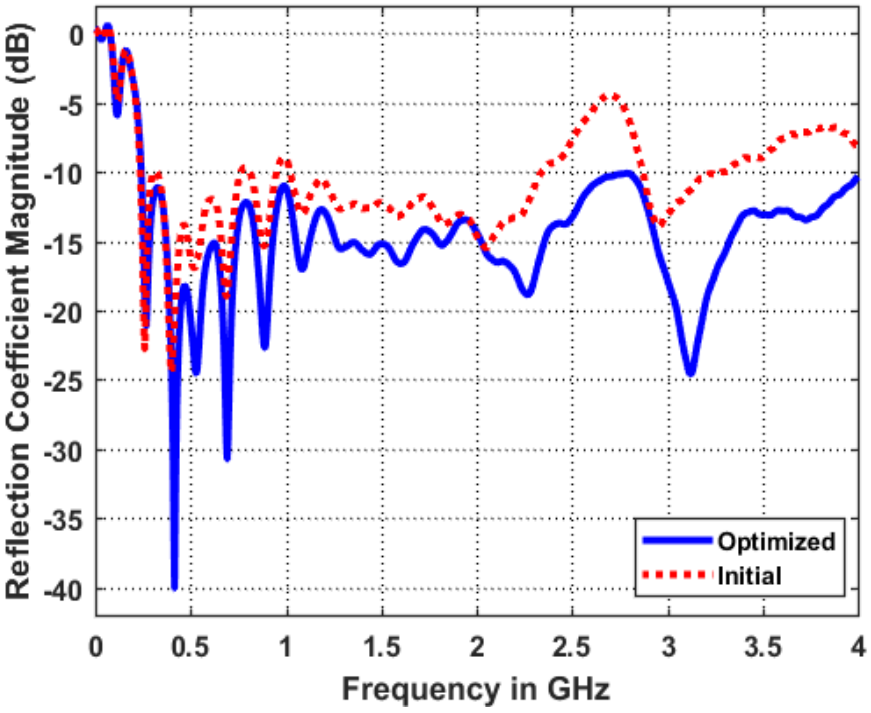


Figure 6.7: Initial and the improved optimized reflection coefficient of the DRGH antenna.

### 6.2.3 Reflection Coefficient of TEM horn and Valentine antennas

The reflection coefficients of the TEM horn and the Valentine antennas were found to be dependent on the nine coaxial to parallel-plate transition parameters that were studied in Section 6.1.2. These nine parameters, together with the axial length of each antenna were optimized. Tables 6.2 and 6.3 show the values of the initial and the optimized parameters for the TEM horn antenna and Valentine antenna respectively. The initial parameter values are the same as those of the fabricated antennas. Figure 6.8 shows the reflection coefficients of these two antennas before and and after optimization.

Table 6.2: Initial and optimized parameters for the TEM horn antenna in ° and cm

| ***Symbol*** | ***Parameter*** | ***Initial*** | ***Optimized*** |
|---|---|---|---|
| $\alpha$ | trim angle | 21.00 | 20.00 |
| $d_e$ | inner coaxial conductor end diameter | 1.10 | 1.18 |
| $l_c$ | coaxial length | 8.00 | 10.46 |
| $t_c$ | coaxial conductor thickness | 0.30 | 0.24 |
| $l_p$ | length of parallel plate | 2.50 | 0.50 |
| $s_b$ | start width of bottom plate | 4.00 | 5.49 |
| $s_t$ | start width of top plate | 6.00 | 5.50 |
| $l_e$ | extended length | 1.50 | 1.63 |
| $t_h$ | triangle height | 10.00 | 8.00 |
| $L_{max}$ | axial length of antenna | 60.00 | 60.00 |

Table 6.3: Initial and optimized parameters for Valentine antenna in ° and cm

| ***Symbol*** | ***Parameter*** | ***Initial*** | ***Optimized*** |
|---|---|---|---|
| $\alpha$ | trim angle | 21.00 | 20.94 |
| $d_e$ | inner coaxial conductor end diameter | 1.10 | 1.18 |
| $l_c$ | coaxial length | 8.00 | 10.50 |
| $t_c$ | outer coaxial conductor thickness | 0.30 | 0.15 |
| $l_p$ | length of parallel plate | 2.50 | 0.72 |
| $s_b$ | start width of bottom plate | 4.00 | 3.50 |
| $s_t$ | start width of top plate | 6.00 | 5.66 |
| $l_e$ | extended length | 1.50 | 1.76 |
| $t_h$ | triangle height | 10.00 | 8.30 |
| $L_{max}$ | axial length of antenna | 70.00 | 68.48 |

The reflection coefficient below 1 GHz is improved for both antennas without an increase in the total length of the antenna. The initial total length of the TEM horn

antenna, including the transition was 82 cm, while the optimized antenna is 80.6 cm. Similarly, the optimized Valentine antenna is 89.8 cm compared to the initial 92 cm. Optimization improves the bandwidth ratio of the two antennas from 10 to 16.

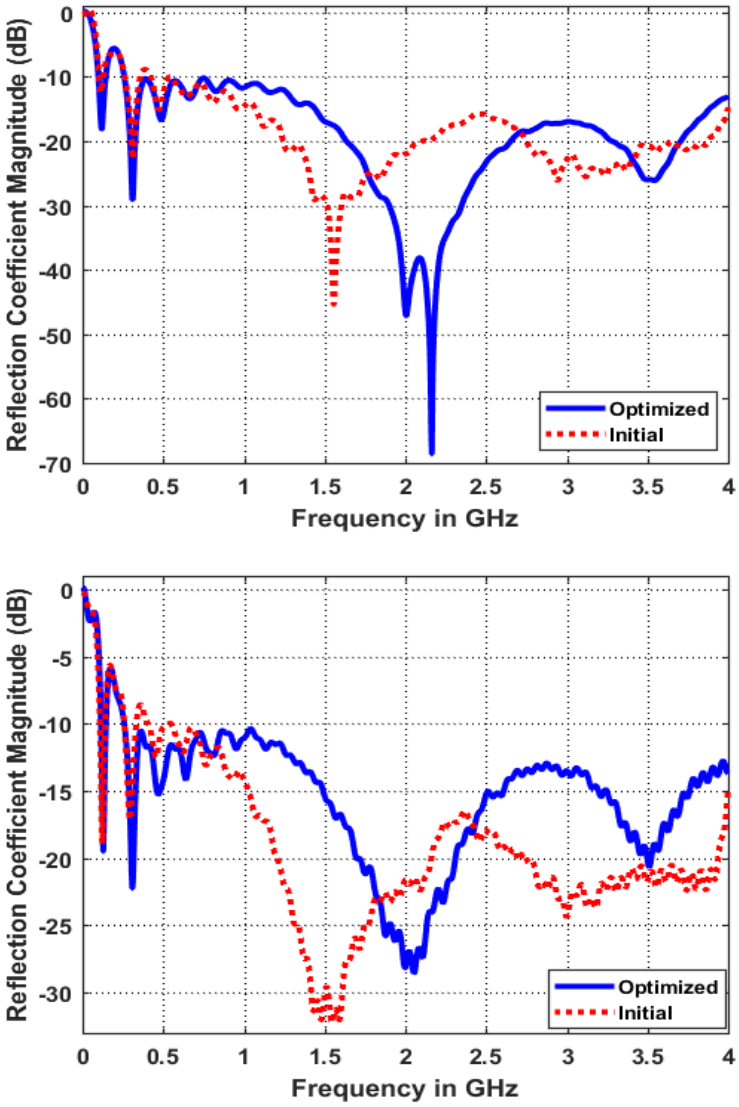


Figure 6.8: Optimized and initial reflection coefficients for the TEM horn (top panel) and the Valentine (bottom panel) antennas.

The realized gain of the optimized antenna is not affected much by the reflection coefficient optimization. The realized gain before and after optimization is compared in Figure 6.9 for all the three antennas. The realized gain of the TEM horn and the Valentine antennas at 4 GHz are improved by about 2 dB.

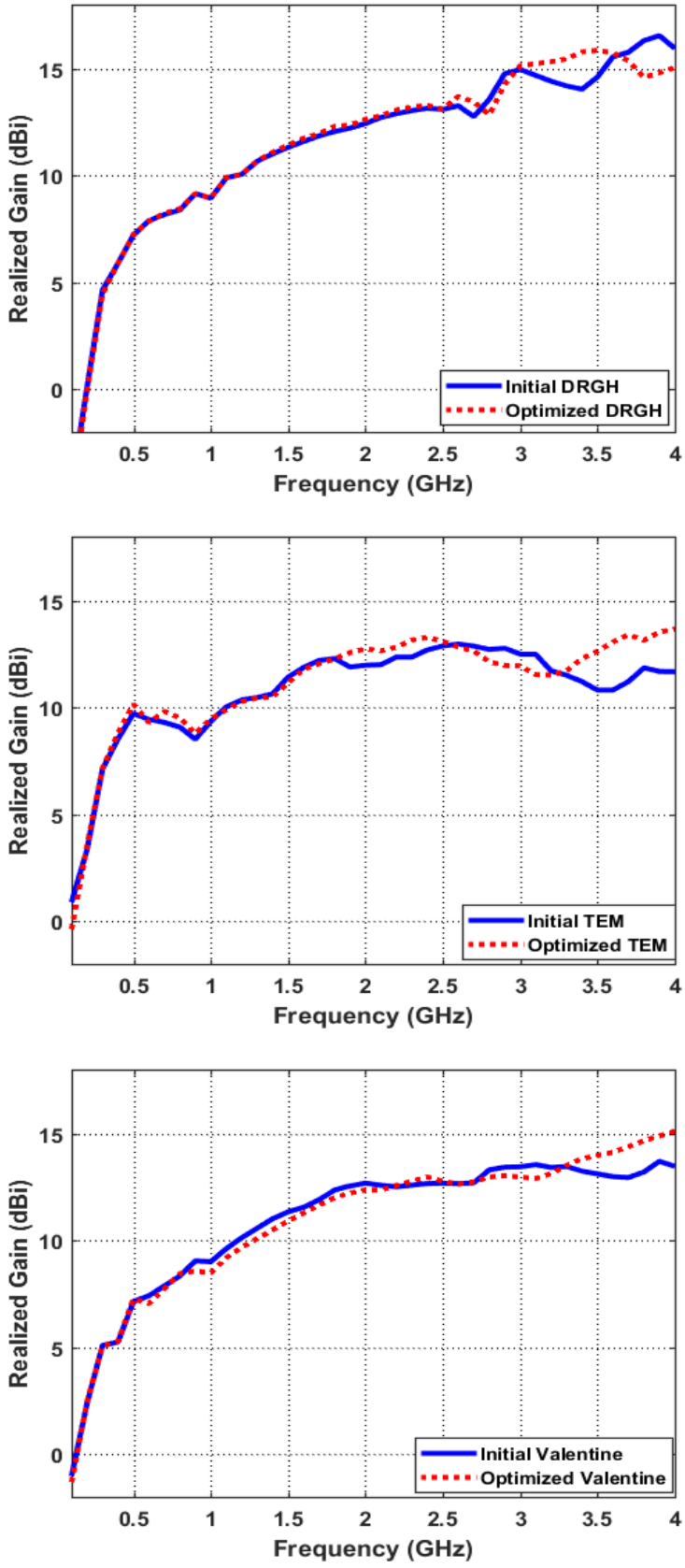


Figure 6.9: Realized gain of the three antennas before and after reflection coefficient optimization, the (top) DRGH, (centre) TEM and (bottom) Valentine antennas.

Figure 6.10 shows the reflection coefficients of the three optimized antennas compared with each other. All the three optimized antennas have a -10 dB bandwidth of 250 MHz to 4 GHz, a bandwidth ratio of 16.

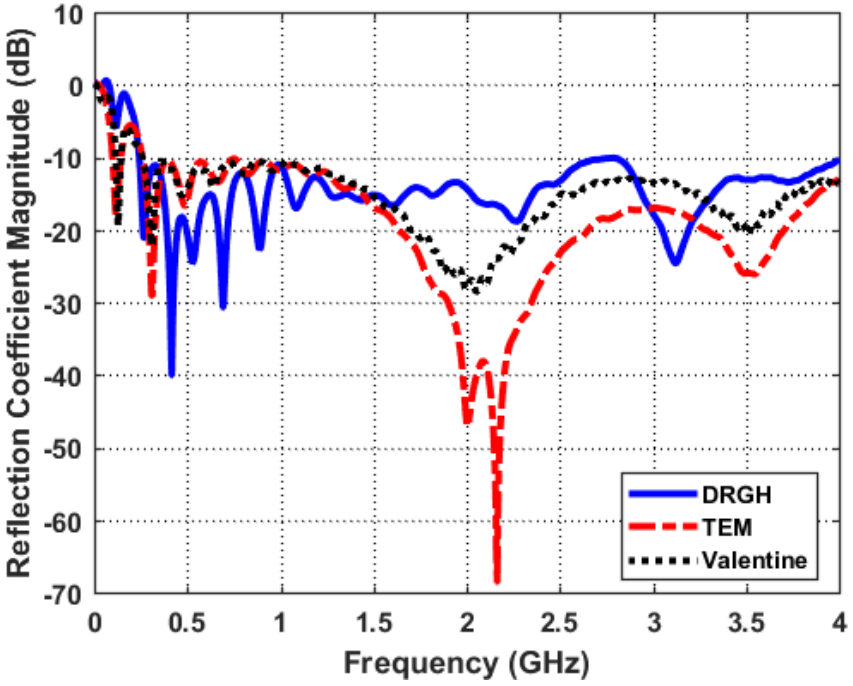


Figure 6.10: Comparison of the optimized reflection coefficients of the three antennas

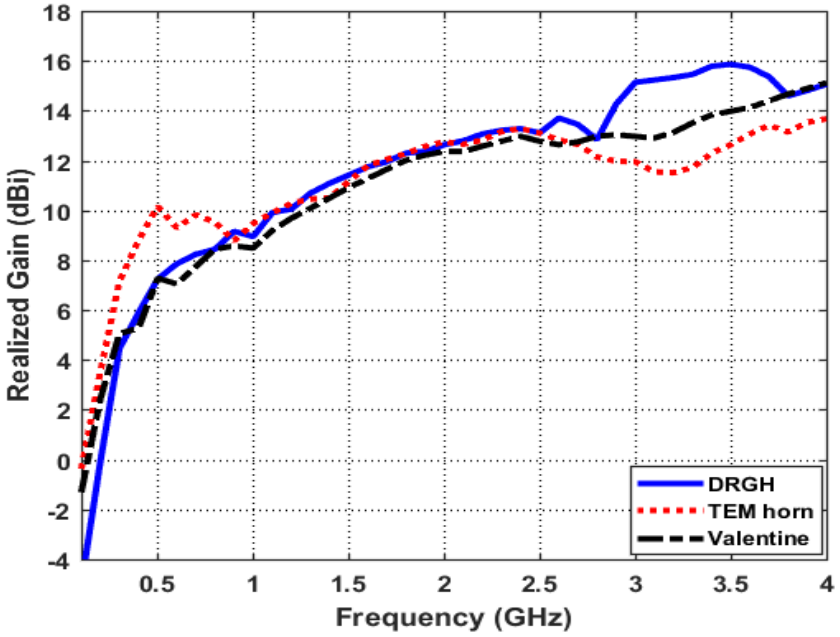


Figure 6.11: Realized gain of the three optimized antennas as a function of frequency.

## 6.3 Conclusion

Optimization has been shown to improve the return loss of the three antennas without any increase in the lengths of the antennas, instead, with a slight decrease in the lengths. The reflection coefficient optimized antennas also do not show any deterioration in the realized gain. The bandwidth ratio of the antennas is improved to 16 and the antennas still remain manufacturable because the necessary limits were enforced. Because of the time limitation, it was not possible to manufacture these optimized antennas although a good performance is expected given the correlation between the measurements and the simulations presented in Chapter 5. The three optimized antennas have comparable realized gain at the mid frequencies 1-2.5 GHz but the TEM performs better at low frequencies. The optimized DRGH has the best gain at high frequencies.

# Chapter 7

# Future Work

Due to time constraints and the unavailability of some equipment, certain aspects of the project could not be completed in full. Here follows a list of recommendations for future work to continue the project:

- Characterizing gain of the antennas further. It was not possible to correctly characterize the gain of the three antennas because of limited time and facilities at teh University. Larger facilities such as a larger anechoic chamber available at Denell Dynamics could be used to characterize the gain of the antennas. Outdoor measurements using the three antenna method can also be explored further with the right equipment.
- Correctly determining the phase centres. The phase centres of these antennas need to be accurately determined by measurement, as this could help in accurately determining the range in gain measurements which would remove a lot of inconsistencies and errors in the gain measurements.
- Further optimization of the antennas. Limited optimization of the antennas was done prior to fabrication of the antennas. An integrated dual-goal function for both the return loss and the gain of the antennas could also be implemented to improve the performance of the antennas before manufacturing the final versions of the antennas.
- Proper manufacturing of the antennas. This could possibly eliminate some discrepancies in the measured and the simulated data as the antennas presented in this thesis were made with affordable and readily available materials in the lab.
- Improving the time domain measurement method. The time domain measurement method that was attempted to characterize the gain of these antenna has not been fully defined. There is a big uncertainty on how to choose the correct measurement distance as well as the size of plates to use for a given measurement. The gain measurements could be improved by correctly determining the size of the plate and the measurement distance that matches with each antenna well. The necessary

time gating window that is large enough to preserve the signal integrity without allowing noise also needs to be determined.

- Determining each antenna's efficiency. Due to the size of the antennas and the amount of metal that were used in their manufacturing, it will also be important to characterize each antenna's efficiency. This would be important in further comparing and deciding on an antenna to use.
- Field testing at the SKA site. The final versions of the antennas should also be taken to the SKA telescope site for testing to see if they do the work they were designed for.

# Chapter 8

# Conclusion

Three types of modified horn antennas, the Double-Ridged Guide Horn (DRGH) antenna, the Transverse ElectroMagnetic (TEM) horn antenna and the Valentine antenna have been designed for Radio Frequency Interference (RFI) testing. All the three antennas have been fabricated using the facilities available at the University. The fabricated antennas have been measured for return loss, radiation patterns and gain and found to confirm the simulated results. Further return loss optimization of the antennas, using SUMO toolbox [50], has also improved the reflection coefficient bandwidth ratio of all three from 10 to 16 (250 MHz to 4000 MHz).

Table 8.1 compares the performance and physical characteristics of the three fabricated and optimized antennas. All the three fabricated antennas were easily prototyped using the facilities available at the University's workshop. The three fabricated antennas each weigh less than 7 kg and are easily portable by one person. The Valentine antenna is the largest of the three antennas with the largest dimension of 118 cm while the DRGH is the smallest of all the three with the largest dimension of 80 cm. The fabricated TEM horn antenna and the DRGH, because of the wooden base, are more robust. The Valentine, however, was predominantly made out of Polystyrene making it light-weight. Because of the Valentine antenna's large surface area, it requires additional mechanical support while doing measurements, particularly outdoor measurements, as it can easily be blown by the wind. The sharp edges of the TEM horn antenna prototype is also a safety hazard as it can easily cause an injury as well as get damaged if care is not taken while transporting it. Rounding of these edges can be looked into in the future versions.

The antennas were fabricated prior to further optimization. It is however evident that the measured DRGH antenna results better replicate the simulated results than for the other two antennas. The TEM horn antenna and Valentine antenna are more susceptible to manufacturing tolerances because of their plate profiles and the coaxial to parallel-plate transition. Moreover, the size of the Valentine antenna and the TEM horn antenna made the two antennas hard to characterize because of the equipment and measurement facilities limitations. The limited scan area of the planar scan probe favoured the smaller

DRGH antenna than the other two antennas. The large dimensions of the TEM horn and the Valentine antenna also made it hard to do measurements inside the small anechoic chamber because of the large required far-field distances.

Overall, the three antennas have comparable return loss performance and realized gain with slight variations across the frequency range. The TEM horn antenna could be preferred for use at low frequencies because of its relatively high gain at low frequencies compared to the other two. The realized gain of the TEM horn antenna deteriorates at the high frequency end. While the gain of the DRGH and the Valentine are relatively higher at high frequencies, the main beam of the DRGH's radiation splits above 2.6 GHz. However, out of all the three fabricated antennas, the DRGH would be chosen over the other two because of its small size, robustness, low weight and easier characterization.

Table 8.1: Comparison of the size and performance of the three antennas

| | **DRGH** | **TEM horn** | **Valentine** |
|---|---|---|---|
| Impedance Bandwidth Ratio (Simulated) | 11 | 10 | 10 |
| Impedance Bandwidth Ratio (Measured) | 9 | 4 | 5 |
| Impedance Bandwidth Ratio (Optimized) | 16 | 16 | 16 |
| Simulated realized gain at 2 GHz (dBi) | 12.5 | 12 | 12.8 |
| Robustness | ✓ | ✓ | ✗ |
| Ease of Manufacturing | ✓ | ✓ | ✓ |
| Replication of simulated results | ✓ | ✗ | ✗ |
| Ease of Characterization | ✓ | ✗ | ✗ |
| Dimensions, L x W x H in cm (Fabricated) | 80 x 54 x 48 | 92 x 80 x 83 | 118 x 49 x 113 |
| Weight (kg) | 5 | 7 | 5 |

# Appendices

# Appendix A

# Antenna Definitions

An antenna is a structure that radiates energy into free space. Its simplest form is a wire. There are terms used to characterize the performance of an antenna, some of them are discussed below.

## A.1 Radiation Intensity

Total power radiated from an antenna per unit solid angle

## A.2 Gain

Gain in a given direction is the ratio of the radiation intensity in that direction to the total power input radiated isotropically.

## A.3 Radiation Pattern

A representation in form of a graph or a function that describes the radiation characteristics of an antenna as a function of spatial coordinates, often in two dimensions or three dimensions. It is usually calculated in the far field.

## A.4 Directivity

Directivity is the ratio of radiation intensity measured for a given direction to that averaged over all the directions. A high directivity in a given direction means that most of the antennas energy is radiated in that direction more than to any other directions.

## A.5 Bandwidth

A range of frequencies for which an antenna operates, frequencies for which the return loss is good, typically less than 10dB

## A.6 Half Power Beamwidth

Half Power Beamwidth (HPBW) is the angular separation of two points where the radiation intensity is half of the maximum radiation intensity, where the two points lie on the plane containing the maximum.

# Appendix B

# Time-Domain Measurement Methods

## B.1 TEM horn and Valentine antenna : Attempt 1

In this first experiment, we attempted to determine the gain of the Valentine antenna and the TEM horn antenna. These measurements were done inside an anechoic chamber and repeated outside on the fifth-floor rooftop. A conducting flat circular plate of comparable size to the antennas, a diameter of 60 cm, was placed at a distance in front of the antennas. Inside the chamber, the plate was placed 2.04 m from the antenna aperture as shown in Figure B.1, which was the maximum distance where the reflected signal was noticeable on the VNA. The measurements were repeated outside with the desire to increase the range. Outside, the circular plate was mounted on a metallic stand, horizontally above

Figure B.1: Time domain gain measurement set up inside anechoic chamber with circular plate (left) and using a rectangular plate (right).

Figure B.2: Outdoor time domain gain measurement set-up with a circular plate target, (left) TEM antenna and (right) Valentine antenna

the sky-facing antenna as shown in Figure B.2. The circular target plate was placed at a height of 2.24 m above the antenna aperture, which was a slightly better range than the indoor measurements. There were, however, too many reflections from the surroundings as shown by the results in Figure B.3.

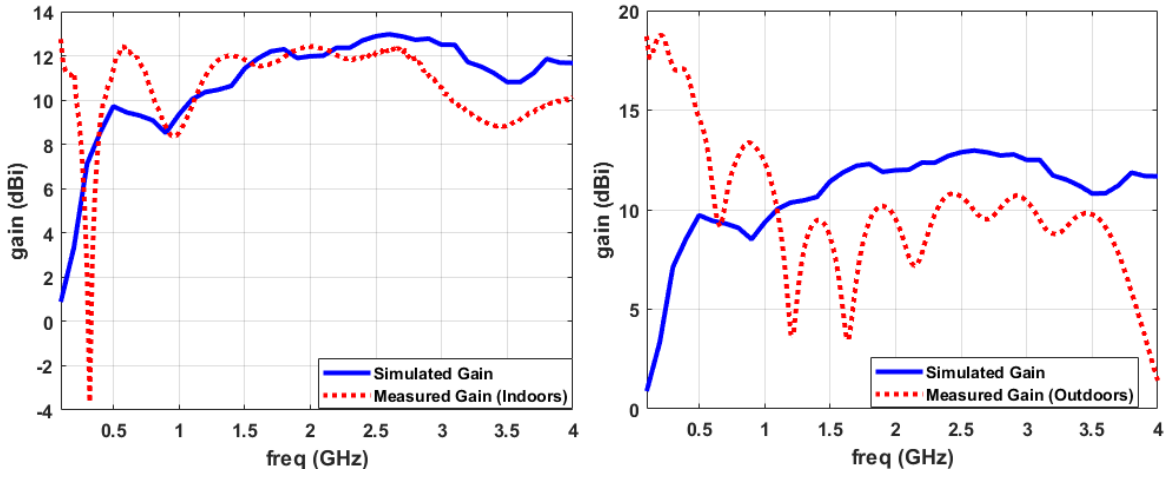


Figure B.3: Realized gain of TEM horn antenna measured by time domain method with a circular plate of diameter 60 cm, compared to the simulated realized gain, the measurements done inside anechoic chamber (left) and outdoors on rooftop (right).

The RCS of a circular plate is given by

$$\sigma = \frac{4\pi^3 r^4}{\lambda^2}, \tag{B.1}$$

when the angle of incidence is $0^o$ and $r$ is the radius of the plate. Figure B.3 shows the measured gain of the TEM horn antenna compared to that simulated. The indoor measurements show some viability especially at the high frequencies, however, the low frequency end doesn't show any similarity to the measurements. Both the TEM horn antenna and the circular plate are in their far-field region at 200 MHz for the given indoor range of 2.04 m. The outdoor measurements seems to have been greatly affected by the metallic pole that used to mount the reflecting plate as well as the ground reflections from the metallic material below the roof. The measurements obtained with the Valentine antenna using this method were equally unsatisfactory. A second attempt was made using rectangular plates and a sphere.

## B.2 TEM horn and Valentine antenna : Attempt 2

Analysis of data from attempt 1 proved that the measurements taken inside the anechoic chamber were much better than those attempted outdoors. A second attempt was therefore made to use rectangular plates and a sphere instead of a circular plate. Two differently sized rectangular plates and a spherical ball were used in this experiment in an attempt to determine the gain of both the TEM and the Valentine antennas. The DRGH was still in the fabrication process. Two rectangular plates, plate 1 of dimension 47.7 cm by 35 cm and plate 2 of size 75 cm by 64.3 cm, were used. A foam sphere coated in Aluminium tape, with radius 15 cm was also tested. The plates were placed at different distances from the antenna aperture. Placing the plate too close to the antenna restricted the range distance which led to a lot of deterioration of gain at the high frequencies. Placing them too far away reduced the quality of the reflected signal, which led to mixing of the signal with noise and loss of information particularly at low frequencies.

The measurements were carried out inside the anechoic chamber with an Agilent N5242A VNA as the measuring equipment. Calibration was done with N-type connectors at the antenna feed. The two rectangular plates were positioned vertically (long side vertical because the H-plane beam-width is wider) in front of the TEM horn antenna at distances 1.6 m, 2.7 m and 4.7 m from the antenna aperture as shown in Figure B.1. The spherical ball centre was positioned at only one distance of 1.4 m away from the TEM horn antenna aperture because beyond 1.4m, there was no reflection detected. Because of promising results with plate 2, experiment was repeated with the Valentine antenna using only plate 2 at the three distances 1.6m, 2.7m and 4.7m. Following the above similar procedure with attempt 1, reflection coefficients with and without the reflecting targets were recorded and used to calculate the gain of the antennas.

The results obtained from this experiment are presented in Figures B.5 and B.4. The results did not agree with the simulated gain. However, there is a similar trend of higher frequency gains, requiring the near-field correction factor. Out of the the two rectangular plates and the sphere, only Plate 2 setup with the TEM horn antenna at 4.7 m was the only promising outcome. The best measurements for the TEM experiment at low frequencies was using the larger rectangular plate (plate 2: 75 cm by 64.3 cm) where the plate size is comparable to the antenna dimensions and at maximum range (4.7 m). The low frequency measurements agree well with the simulation only up to 0.5 GHz after which the gain deviates. This is expected because both the plate and the antenna are only in their far field region below 0.5 GHz at 4.7 m. The smaller plate records better measurements at higher frequencies than at lower because the beam width of the antenna is narrow at high frequencies and 4.7 m provide longer far field distance for both the plate and the antenna. The results of the sphere did not turn out well either.

Overall, none of these time domain measurements give us an accurate gain measurement yet. Different sizes of plates have to be used to determine gain at different frequencies. Determining the correct plate size and range of the plates from the antennas for these time domain measurements has to be thoroughly investigated on a case-by-case basis before doing the measurements.

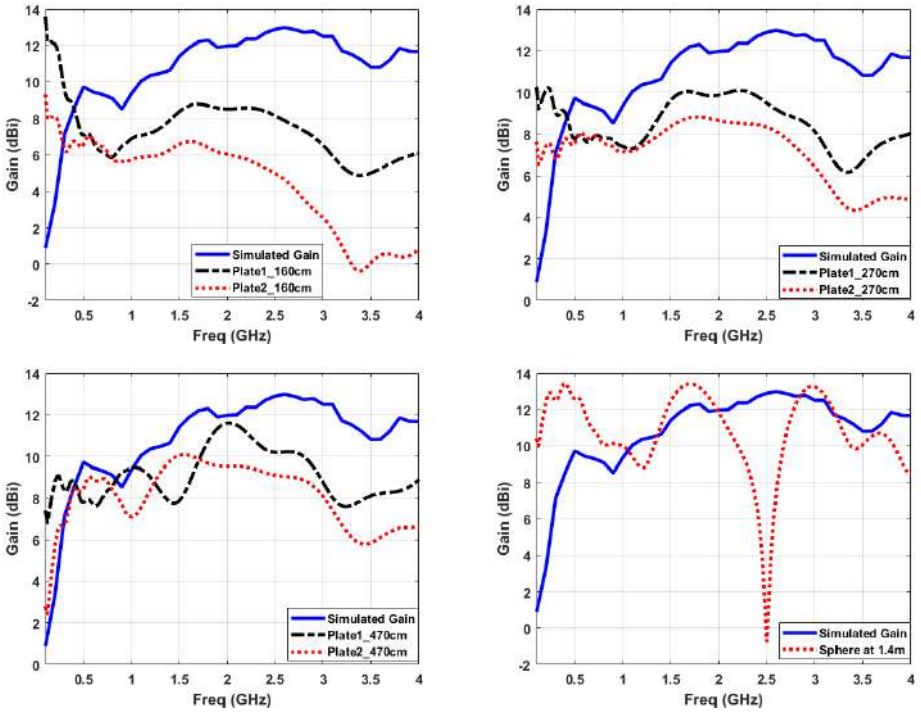


Figure B.4: Measured and simulated gain of the TEM horn antenna using two different plates, plate 1 (47.7 cm by 35 cm ) and plate 2 (64.3 cm by 75 cm) placed at 160cm, 270 cm and 470 cm away from the antenna aperture and and a sphere (30 cm diameter) placed at 140 cm from the antenna aperture.

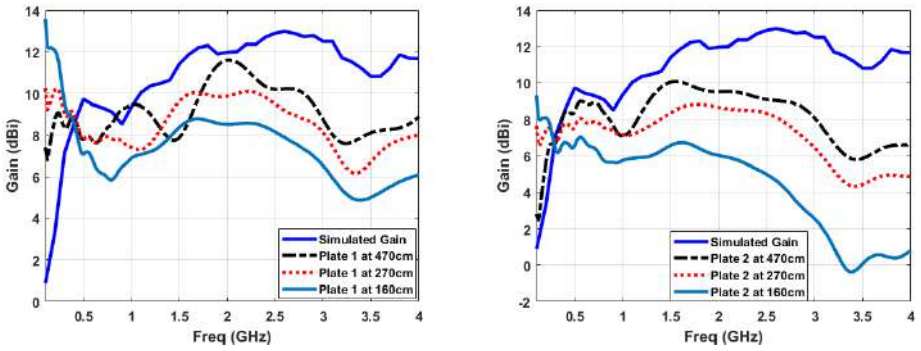


Figure B.5: Measured and simulated gain of the TEM horn antenna using two different plates, (left) plate 1 (47.7 cm by 35 cm ) and (right) plate 2 (64.3 cm by 75 cm) placed at 160cm, 270 cm and 470 cm away from the antenna aperture.

## B.3 DRGH : Attempt 3

The DRGH antenna was also tested with the time domain method. Three different sized rectangular plates were used plates A, B and C. Plate A was 47.6 cm by 34.9 cm, Plate B was 56cm by 47.5 cm and plate C was 62.1 cm by 62.1 cm. Three different gating windows were used for each measurement, Windows 1, 2 and 3 with window 1 being the smallest and 3 the largest window. Each plate was placed at four different distances from the antenna aperture, Distance 1 at 1.5 m, Distance 2 at 3 m, Distance 3 at 4.2 m and Distance 4 at 5 m. Figures B.6-B.9 show the results obtained from this experiment. The measurements obtained at 3 m closely replicate the simulated results. At distances beyond 4.2 m there seems to be loss of information in the reflected signal. A plate with similar size to the antenna gives the best results.

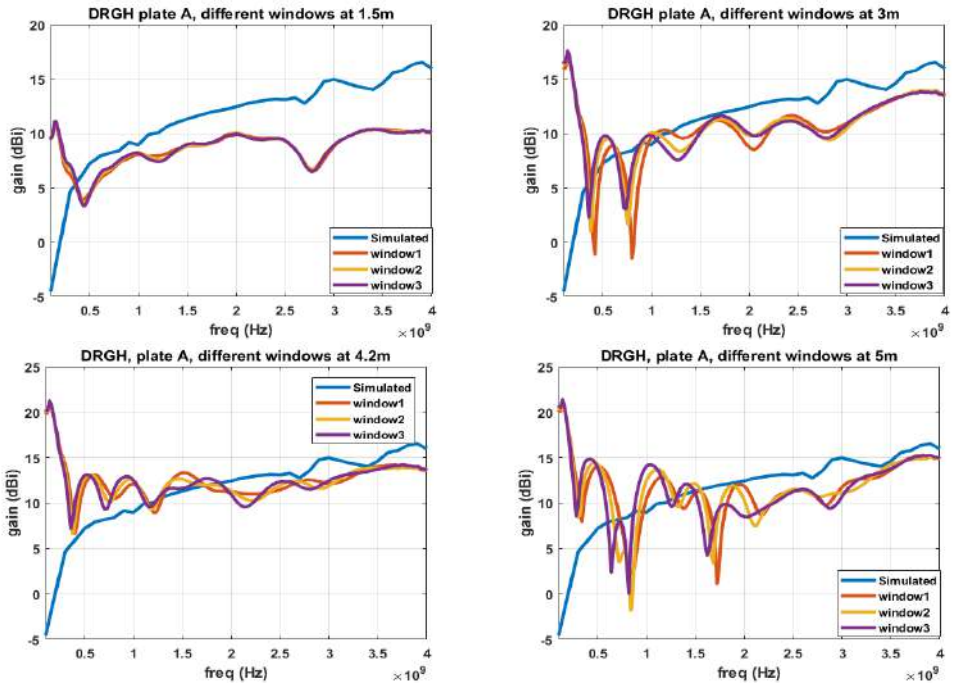


Figure B.6: DRGH gain measurements using plate A at 4 different distances. Different gating windows applied.

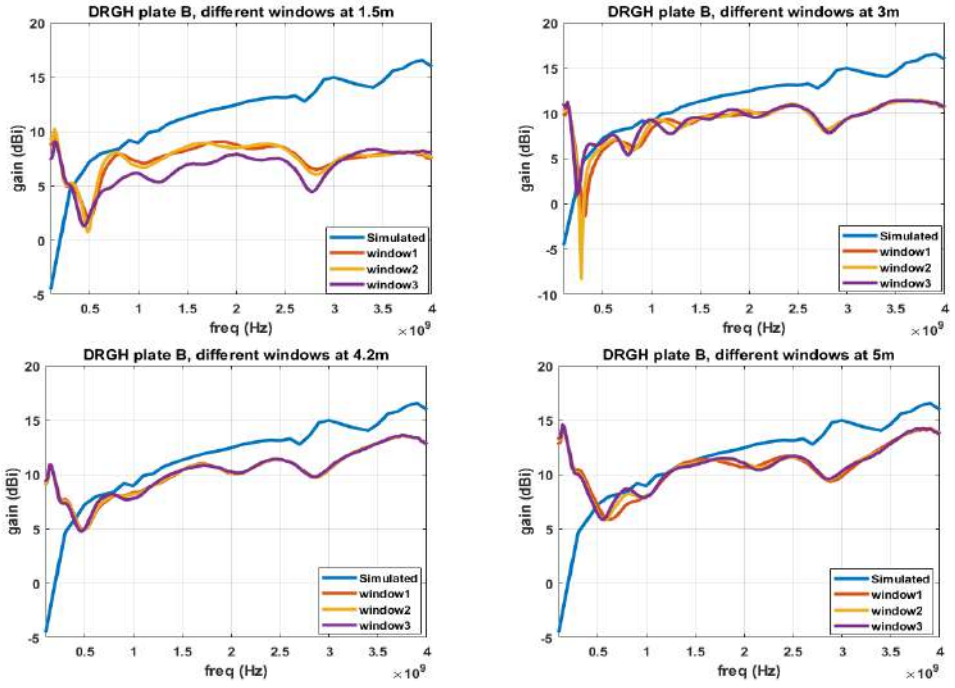


Figure B.7: DRGH gain measurements using plate B at 4 distances. Different gating windows applied.

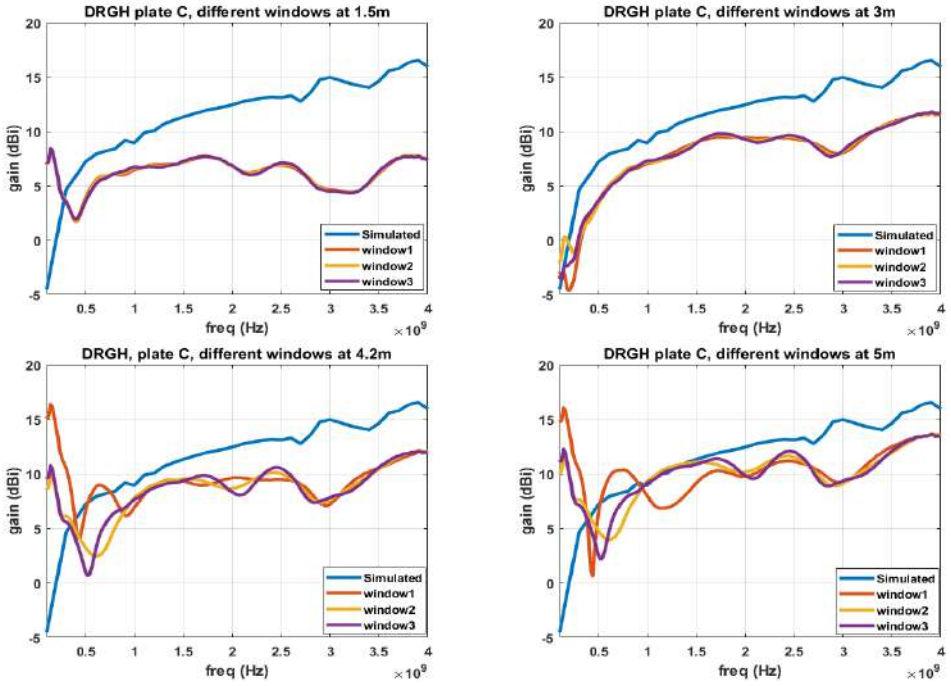


Figure B.8: DRGH gain measurements using plate C at 4 distances. Different gating windows applied.

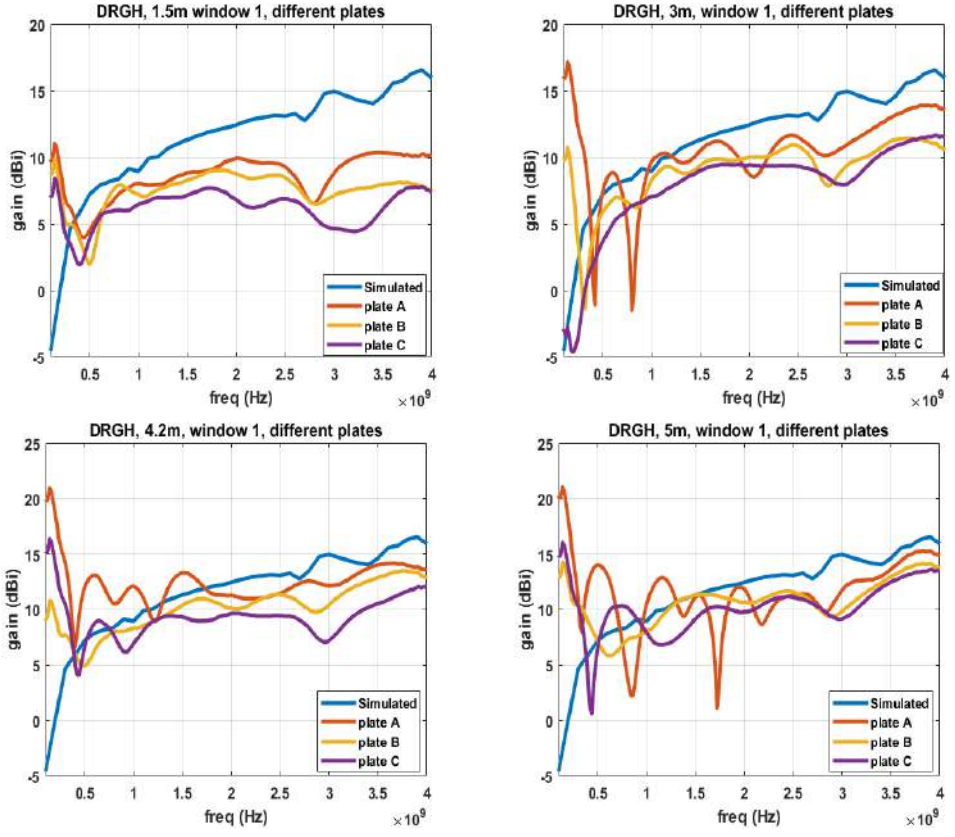


Figure B.9: Plate comparison at different distances

## B.4 Valentine Antenna : Attempt 4

Time domain measurements were repeated for the Valentine antenna with a plate size of 82 cm by 67 cm, the largest that was available. Ideally, we would have used a plate with a comparable size with the antenna aperture (about 1m). Only one plate was used, but measurements were done at 7 different ranges: 2.5 m, 3 m, 3.5 m, 4 m, 4.5 m, 5 m and 5.5 m. As shown in Figure B.10, none of the measurements is close to the expected simulated gain. The plate used is to big to be in the far-field distance from the antenna inside the anechoic chamber. The furthest distance in the anechoic chamber is also too far for the low frequency components of the signal to be retained.

Similar to what was observed with the other antenna measurements, it is evident that at greater distances the gain deterioration at high frequency is the greatest. At such far distances, the information loss at low frequeny is also observed.

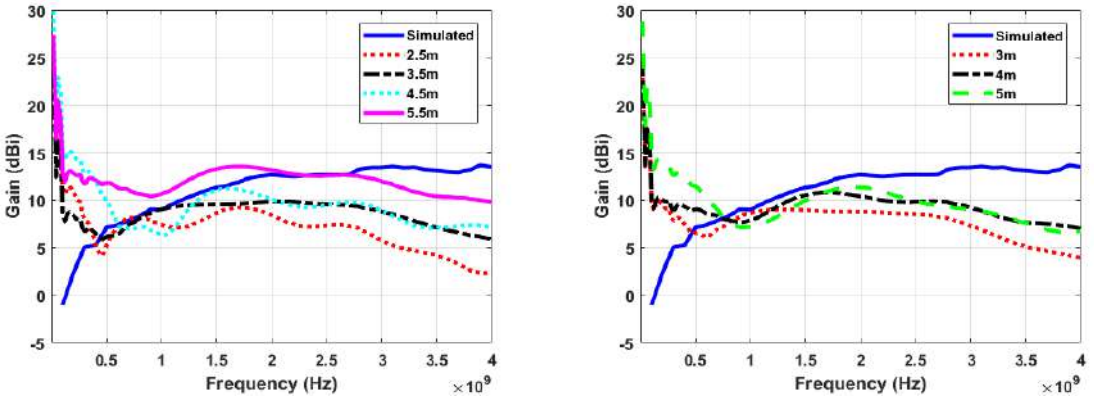


Figure B.10: Valentine antenna gain measurements using a plate of size 82 cm by 67 cm at 7 different range distances compared to the simulated gain.

# Appendix C

# Gain Corrections

## C.1 Phase Centre Calculation

The range, R, in gain measurements, needs to be accurately determined because of the wide-band nature of the antenna. Phase centre calculations at the different frequencies were done using the method discussed in [49] for a pyramidal horn antenna with similar dimensions to the DRGH. The radiation at low frequencies is expected to occur at the aperture of the antenna while the rest occur close to the feed. For a pyramidal horn antenna model with the dimensions shown in Figure C.1, the E-plane and the H-plane phase centres can be calculated [49]. The phase centre is the distance along the axial length with the antenna aperture as the reference point. The E-plane phase centre is given by

$$\Delta_r(\theta, \phi = 90^o) = l_e\left[1 - \frac{a}{2v_e}\frac{\cos\frac{\pi}{2}(\frac{a}{2v_e})^2 C(\frac{a}{2v_e}) + \sin\frac{\pi}{2}(\frac{a}{2v_e})S(\frac{a}{2v_e})}{C^2(\frac{a}{2v_e}) + S^2(\frac{a}{2v_e})}\right], \tag{C.1}$$

and the H-plane phase centre, $\Delta_r(\theta, \phi = 0^o)$ is given by

$$l_h\left[1 + \frac{\left[W_1\cos\frac{\pi}{2}{U_1}^2 - U_1\cos\frac{\pi}{2}{W_1}^2\right]\left[C(U_1) - C(W_1)\right] + \left[U_1\sin\frac{\pi}{2}{W_1}^2 - W_1\sin\frac{\pi}{2}{U_1}^2\right]\left[-S(U_1) + S(W_1)\right]}{\left[C(U_1) - C(W_1)\right]^2\left[-S(U_1) + S(W_1)\right]^2}\right], \tag{C.2}$$

where

$$v_e = \sqrt{l_e\lambda/2}, U_1 = \frac{v_h}{b} + \frac{b}{2v_h}, W_1 = \frac{v_h}{b} - \frac{b}{2v_h}, v_h = \sqrt{l_h\lambda/2} \tag{C.3}$$

and a is the aperture width, b is the aperture height, C(.) is the Fresnel cosine function and S(.) is the Fresnel sine function. This method doesn't however provide an approach to theoretically calculate the phase centre of TEM horn, Valentine and DRGH antennas. Only an approximation for a similar-sized pyramidal horn antenna as the double ridged horn antenna. The phase centre for a pyramidal horn antenna with similar dimensions like the DRGH was calculated using the equations in [49]. The E-plane phase centre is as shown in Figure C.2. The phase centre moves aways from the aperture as the frequency

increases. However, as seen in C.2, the Muehldorf calculated phase centres vary greatly in the two planes because of the rectangular aperture.

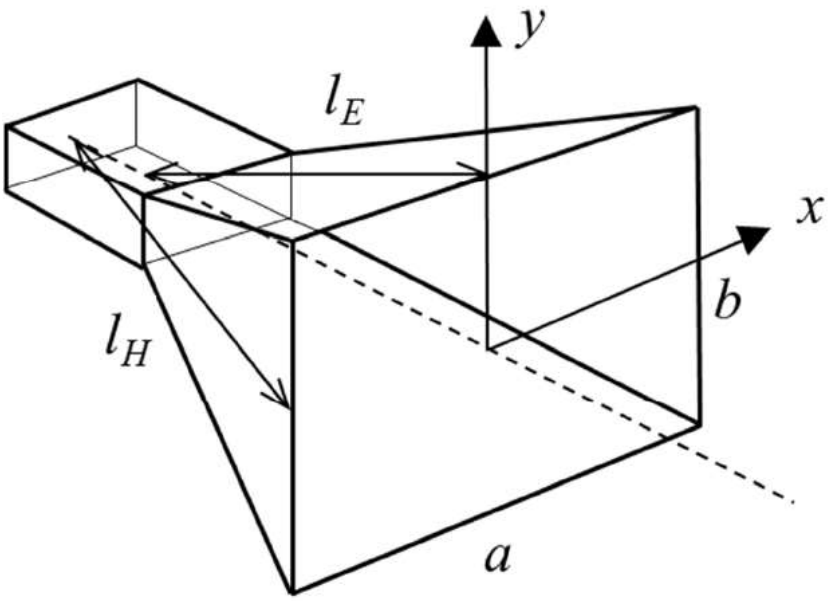


Figure C.1: Dimensions of a horn antenna used to calculate the phase centre [54]

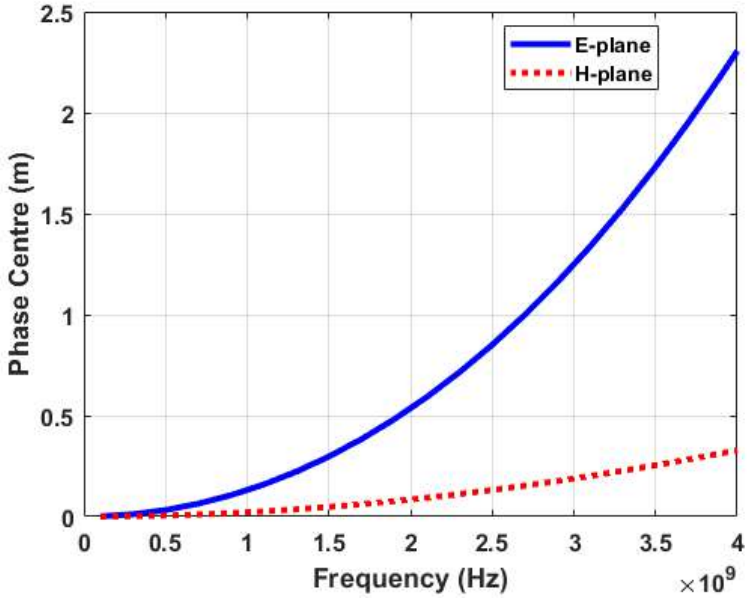


Figure C.2: Calculated distance of the phase centre in the E-plane from the antenna aperture for a pyramidal horn antenna. The phase centre moves way from the aperture

## C.2 Near-Field Gain Correction Factor

For a pyramidal horn antenna with the same waveguide and aperture dimensions as the DRGH fabricated, the gain correction factor can be determined using guidelines provided by Semplak and Chu [42]. The dimensions shown in figure C.3 for a pyramidal horn antenna similar to DRGH, a=0.6 , b=0.43 m, c = 0.26 m, d = 0.1219 m and horn axial length, $L$, of 0.6 m. $L_E$ and $L_H$ are calculated as

$$L_E = \frac{a}{\sin\left[\tan^{-1}\frac{a-c}{L}\right]} = 0.9413m$$

$$L_H = \frac{b}{\sin\left[\tan^{-1}\frac{b-d}{L}\right]} = 1.2173m$$

and the parameters M, H, N and P at different frequencies are given in Table C.1.

$$M = 8\lambda L_E/b^2$$

$$H = 8\lambda R/b^2$$

$$N = 8\lambda L_H/a^2$$

$$P = 8\lambda R/a^2$$

By calculation using the equations for E-plane and H plane correction factors in [42], the required gain correction required for this pyramidal horn antenna because of the near field gain measurements are calculated and shown in Table C.1. For measurements done at 3 m, the gain correction factor, $C$, for this pyramidal horn antenna at 200 MHz is 0.01 dB but increases up to 2.41 dB at 4 GHz.

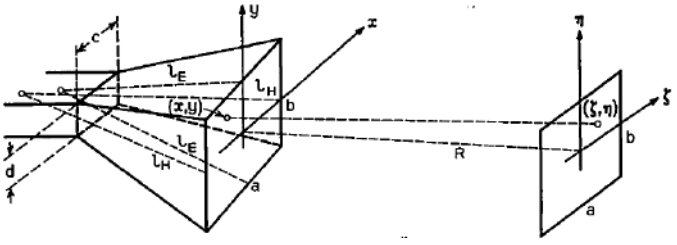


Figure C.3: Pyramidal horn dimensions [42]

Table C.1: Calculated parameters for gain correction

| **Frequency (GHz)** | **M** | **H** | **N** | **P** | $C_E$ **(dB)** | $C_H$ **(dB)** | **C(dB)** |
|---|---|---|---|---|---|---|---|
| 0.20 | 78.67 | 193.92 | 31.25 | 99.60 | 0.0034 | 0.0067 | 0.01 |
| 1.00 | 15.73 | 38.78 | 6.25 | 19.92 | 0.085 | 0.16 | 0.245 |
| 2.00 | 7.86 | 19.39 | 3.13 | 9.96 | 0.33 | 0.55 | 0.88 |
| 3.00 | 5.24 | 12.93 | 2.08 | 6.64 | 0.69 | 0.98 | 1.67 |
| 4.00 | 3.93 | 9.70 | 1.56 | 4.98 | 1.12 | 1.29 | 2.41 |

# Appendix D

# Waveguide Theory

Some modes that can propagate in a waveguide are the Transverse Electric (TE), the Transverse Magnetic (TM) and the Transverse Electric and Magnetic (TEM). For a TE mode, all the Electric field components are transverse to the direction of propagation. If $\vec{z}$ is the direction of propagation, then $E_z$ is equal to zero.

Similiarly for a TM mode the components of Magnetic field are transverse to the direction of propagation, $H_z$ is zero.

For a TEM mode, both the electric and the magnetic field components are transverse to the direction of propagation. There is no cutoff frequency required for this propagation mode. At least two separate conductors are needed for waves propagating in TEM mode. Some types of waveguides that support TEM waves are: coaxial cable, parallel plate waveguide, stripline and microstrip.

### D.0.1 Ridged Waveguide Impedance Analysis

Waveguide impedance is known as wave impedance. For Transverse Electric waves the wave impedance is given by

$$Z_{TE} = \frac{\omega\mu}{\beta} \tag{D.1}$$

for Transverse Magnetic, it is defined as,

$$Z_{TM} = \frac{\beta}{\omega\epsilon}, \tag{D.2}$$

where $\beta$ is the imaginary part of the propagation constant. The characteristic impedance of a ridged waveguide can be adjusted by varying the height of the ridges. The impedance can be varied between that of a regular rectangular waveguide and a coaxial cable. To see this effect, we model a section of the ridged waveguide in CST and analyze the effect of varying the separation distance of the ridges on wave impedance.

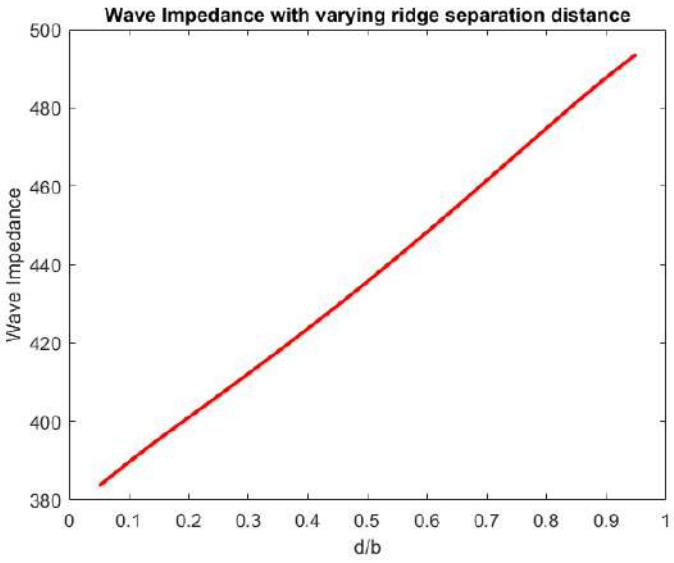


Figure D.1: Wave Impedance with varying ridge separation distance

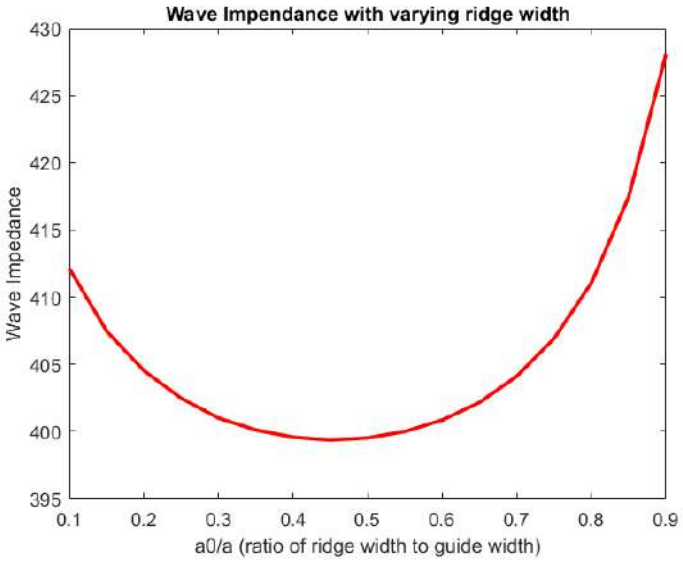


Figure D.2: Wave impedance with varying ridge width

# Appendix E

# 3D Radiation Patterns

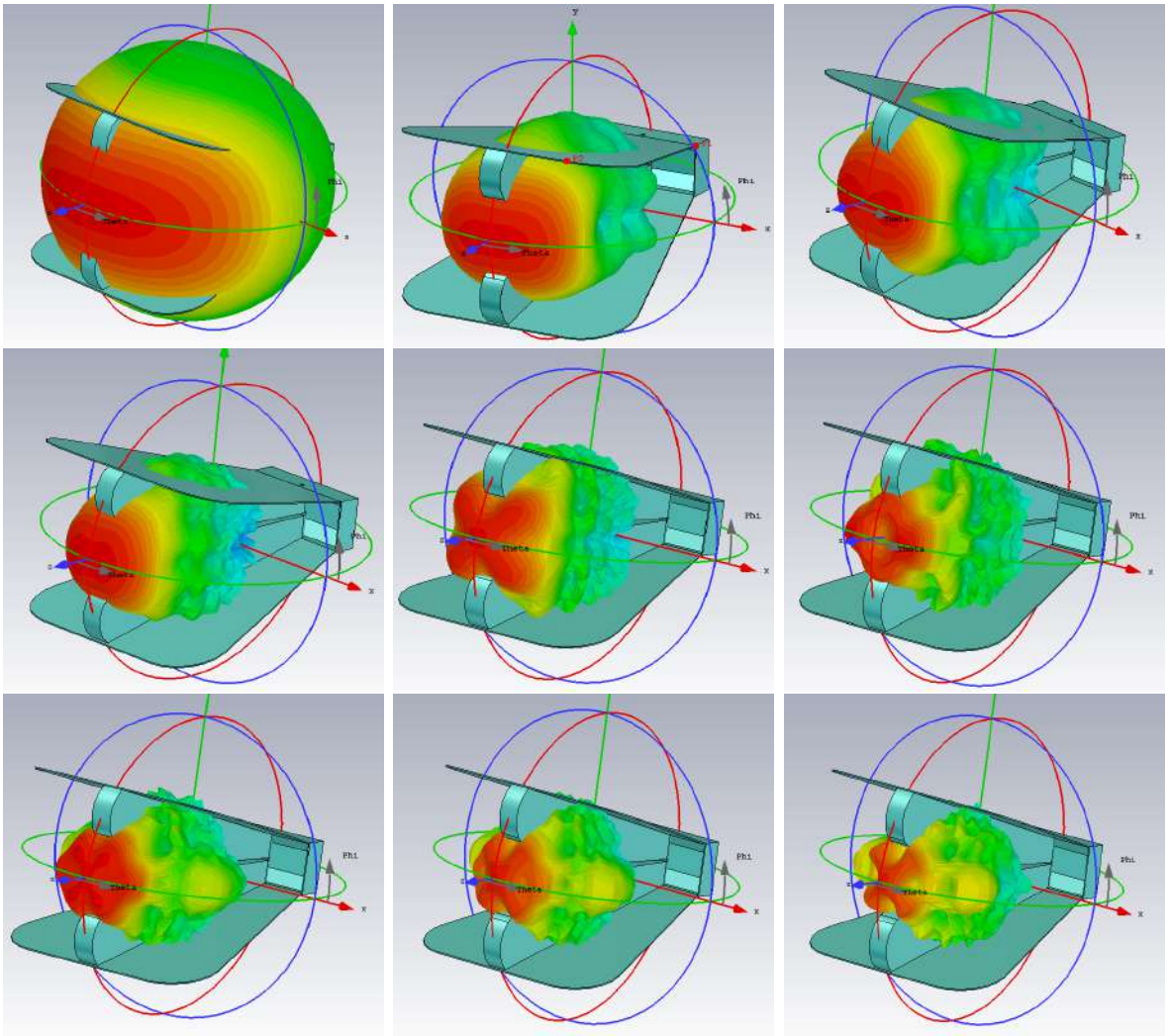

Figure E.1: 3D radiation patterns of the DRGH antenna at 0.2 GHz, 1.2 GHz,1.8 GHz 2.4 GHz,2.6 GHz, 2.9 GHz, 3.4 GHz, 3.6 GHz and 4 GHz. The radiation pattern beyond 2.6 GHz is no longer a single main lobe like at the lower frequencies. At 4 GHz the beam splits into four.

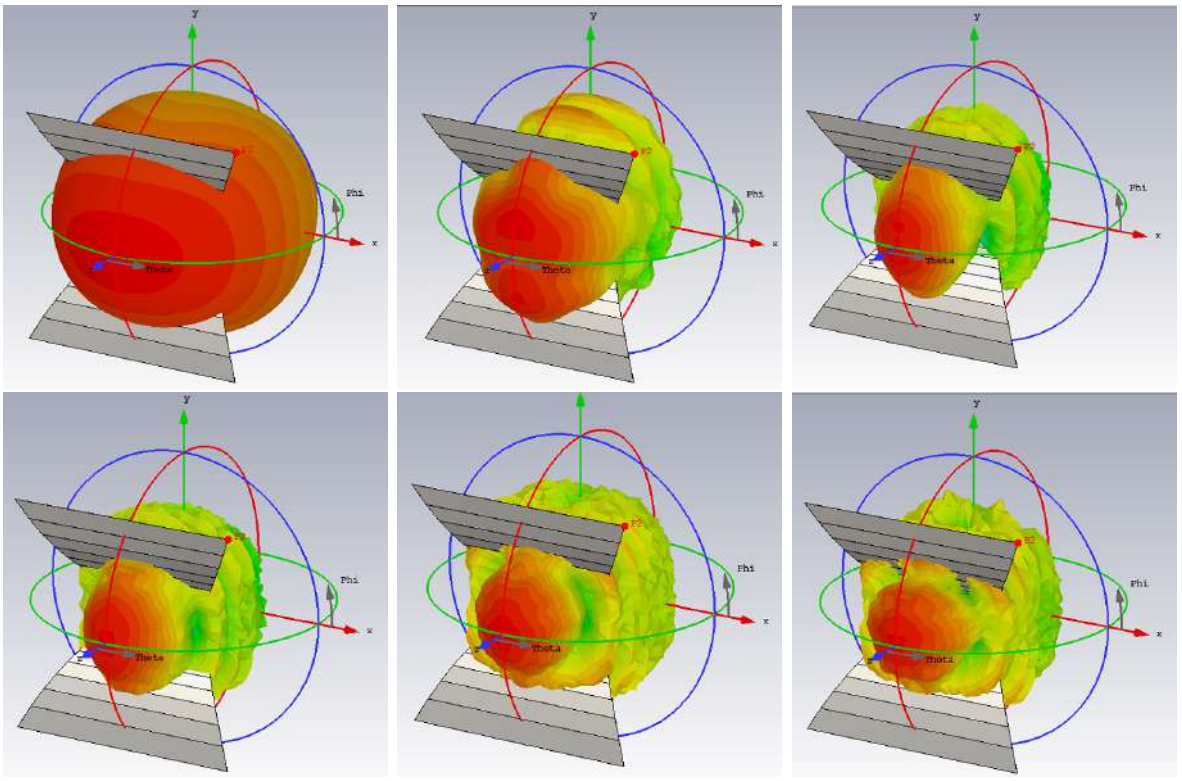

Figure E.2: 3D radiation patterns of the TEM horn antenna at 0.2 GHz, 1.2 GHz, 2.6 GHz, 2.9 GHz, 3.4 GHz and 4 GHz. The radiation pattern does not split at high frequencies.

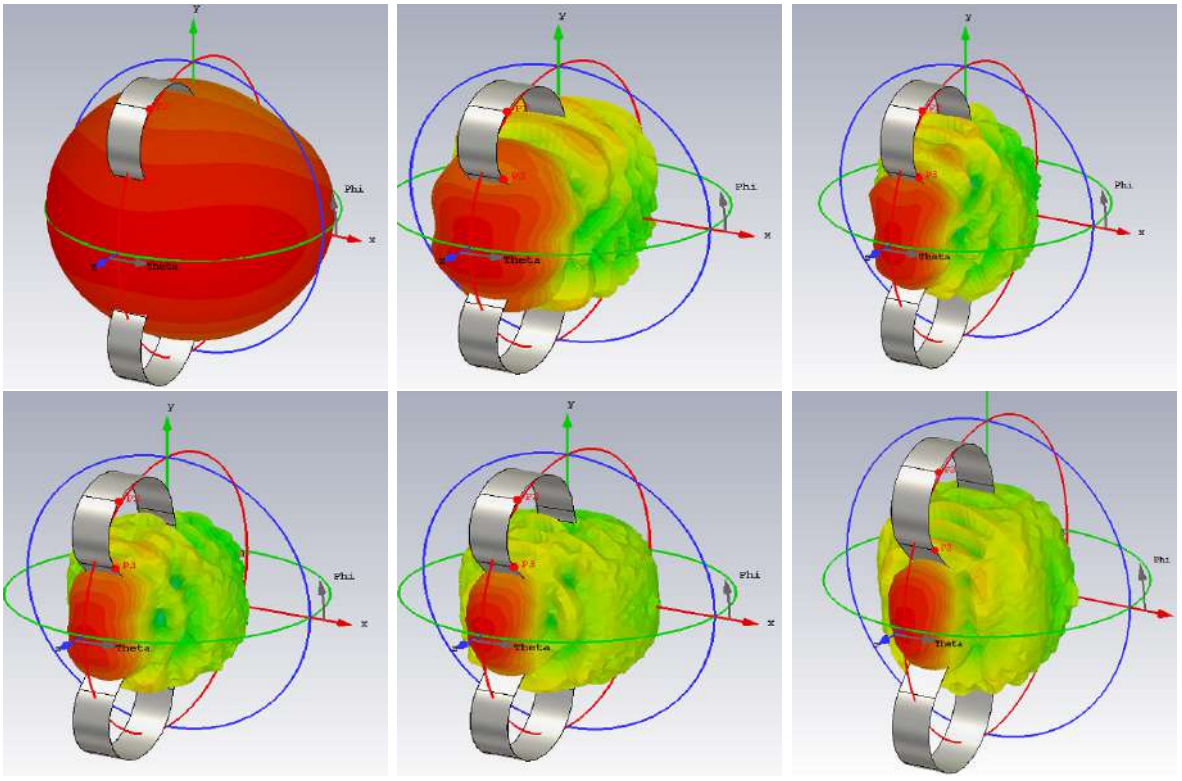

Figure E.3: 3D radiation patterns of the Valentine antenna at 0.2 GHz, 1.2 GHz, 2.6 GHz, 2.9 GHz, 3.4 GHz and 4 GHz. The radiation pattern does not split at high frequencies.

# References

[1] SKA, "Square Kilometre Array." [Online]. Available: https://www.skatelescope.org/

[2] MeerKat, "About MeerKAT." [Online]. Available: https://www.ska.ac.za/science-engineering/meerkat/about-meerkat/

[3] A. R. Mallahzadeh and A. Imani, "Double-ridged antenna for wideband applications," *Progress In Electromagnetics Research*, vol. 91, pp. 273–285, 2009.

[4] K. Chung, S. Pyun, and J. , "Design of an ultrawide-band TEM horn antenna with a microstrip-type balun," *IEEE Transactions on Antennas and Propagation*, vol. 53, no. 10, pp. 3410–3413, Oct 2005.

[5] J. C. Diot, P. Delmote, J. Andrieu, M. Lalande, V. Bertrand, B. Jecko, S. Colson, R. Guillerey, and M. Brishoual, "A novel antenna for transient applications in the frequency band 300 MHz - 3 GHz: The Valentine antenna," in *IEEE Transactions on Antennas and Propagation*, vol. 55, no. 3 II, Mar 2007, pp. 987–990.

[6] D. Systemes, "CST Studio Suite 3D EM Analysis Software." [Online]. Available: https://www.3ds.com/products/-services/simulia/products/cst-studio-suite/

[7] C. A. Balanis, *Modern antenna handbook*, 1st ed. Wiley Interscience, 2007.

[8] C. A. Balanis, *Antenna theory : analysis and design*, 3rd ed. Wiley Interscience, 2005.

[9] G. Abhignya, B. Yogita, C. Abhinay, and B. Balaji, "Design, fabrication and testing of pyramidal horn antenna," in *Inter. Journal of Engin. & Applied Sci*, vol. 2, no. 24, 2015, pp. 2394–3661.

[10] S. S. B. Cohn, "Properties of ridge wave guide," *Proceedings of the IRE*, vol. 35, no. 8, pp. 783–788, Aug 1947.

[11] S. Hopfer, "The Design of Ridged Waveguides," *IEEE Transactions on Microwave Theory and Techniques*, vol. 3, no. 5, pp. 20–29, Oct 1955.

[12] A. Mehrdadian, H. Fallahi, M. Kaboli, and S. A. Mirtaheri, "Design and implementation of 0.7 to 7 GHz broadband double-ridged horn antenna," *7'th International Symposium on Telecommunications (IST'2014)*, pp. 250–255, Sep 2014.

[13] D. M. Pozar, *Microwave Engineering.*, 4th ed. Wiley, 2012.

[14] A. Genc, I. B. Basyigit, T. Goksu, and S. Helhel, "The comparison of the characteristics of the double-ridged horn antennas depending the geometry of ridge profiles for wideband application," in *2017 Progress In Electromagnetics Research Symposium - Spring (PIERS)*. IEEE, May 2017, pp. 1553–1557.

[15] A. Mallahzadeh and A. Imani, "Modified double-ridged antenna for 2-18 GHz," *Applied Computational Electromagnetics Society Journal*, vol. 25, no. 2, pp. 137–143, 2010.

[16] M. Abbas-Azimi, F. Arazm, and J. Rashed-Mohassel, "Design of a new broadband EMC double ridged guide horn antenna," *2006 First European Conference on Antennas and Propagation*, pp. 1–5, Nov 2006.

[17] M. Ghorbani and A. Khaleghi, "Double ridged horn antenna designs for wideband applications," *2011 19th Iranian Conference on Electrical Engineering*, no. January 2011, pp. 1–4, May 2011.

[18] J. Kerr, "Short axial length broad-band horns," *IEEE Transactions on Antennas and Propagation*, vol. 21, no. 5, pp. 710–714, Sep 1973.

[19] Zhongxiang Shen and Chao Feng, "A new dual-polarized broadband horn antenna," *IEEE Antennas and Wireless Propagation Letters*, vol. 4, pp. 270–273, 2005.

[20] M. Puri, P. K. Mishra, S. S. Dhanik, and H. Khubchandani, "Design and simulation of double ridged horn antenna operating for UWB applications," *2013 Annual IEEE India Conference, INDICON 2013*, vol. 1, 2013.

[21] K. B. Steghafner H.,Leugner D, "Horn Antenna," *U.S. Patent 2011/7969376 B2*, 2011.

[22] V. Rodriguez, "Recent improvements to dual ridge waveguide horn antennas: The 200 MHz to 2000 MHz and 18 GHz to 40 GHz models," in *2009 IEEE International Symposium on Electromagnetic Compatibility*. IEEE, Aug 2009, pp. 24–27.

[23] S. Demirel, A. Çaliskan, M. T. Mersin, A. S. Türk, M. A. Belen, and P. Mahouti, "Design of dielectric lens loaded double ridged horn antenna for millimetre wave application," *2016 21st International Conference on Microwave, Radar and Wireless Communications, MIKON 2016*, 2016.

[24] Vicente Rodriguez-Pereyra, "New broadband EMC double-ridge guide horn antenna," *RF Design*, pp. 44–47, 2004.

[25] P. L. C. Bruns and R. Vahldieck, "Analysis and simulation of a 1-18-GHz broadband double-ridged horn antenna," *IEEE Transactions on Electromagnetic Compatibility*, vol. 45, no. 1, pp. 55–60, Feb 2003.

[26] B. Jacobs, J. W. Odendaal, J. Joubert, S. Member, and J. Joubert, "An improved design for a 1 to 18 GHz double-ridged guide horn antenna," *IEEE Transactions on Antennas and Propagation,*, vol. 60, no. 9, pp. 4110–4118, 2012.

[27] R. H. A. Di Maria, A. Kość , M. Limbach and A. Reigber, "Design and measurements of a Double Ridged Guide Horn feed for P-Band direct path measurements," in *2013 7th European Conference on Antennas and Propagation (EuCAP)*. IEEE, 2013, pp. 2436–2439.

[28] K. Harima, "Numerical estimation for TEM horn antennas with transmission line taper shapes," *IEICE Communications Express*, vol. 6, no. 9, pp. 560–565, 2017.

[29] R. Lee and G. Smith, "A design study for the basic TEM horn antenna," *IEEE Antennas and Propagation Magazine*, vol. 46, no. 1, pp. 86–92, Feb 2004.

[30] M. Kanda, "The effects of resistive loading of "TEM" horns," *IEEE Transactions on Electromagnetic Compatibility*, vol. EMC-24, no. 2, pp. 245–255, May 1982.

[31] A. A. Jamali and R. R. Marklein, "Design and optimization of ultra-wideband TEM horn antennas for GPR applications," *2011 URSI General Assembly and Scientific Symposium*, pp. 1–4, Aug 2011.

[32] A. A. H. Ameri, G. Kompa, and A. Bangert, "Study about TEM horn size reduction for ultrawideband radar applications," *2011 German Microwave Conference*, 2011.

[33] B. Cadilhon, B. Cassany, P. Modin, J.-C. Diot, V. V. Bertrand, L. Barp, E. Technopole, L. Pécastaing, and L. Pecastaing, "Ultra Wideband Antennas for High Pulsed Power Applications," Aug 2010.

[34] E. Ben-Ari, "Design of an Ultra-Wideband High-Power-Microwave Traveling-Wave Antenna," *CST Application Article*, pp. 1–8, 2014.

[35] J. Duncan and V. Minerva, "100:1 Bandwidth balun transformer," *Proceedings of the IRE*, vol. 48, no. 2, pp. 156–164, Feb 1960.

[36] H. D. O. Ascama, R. K. Hiramatsu, A. M. de Oliveira, C. R. P. Dionisio, S. T. Kofuji, A. M. De Oliveira, C. R. P. Dionisio, S. T. Kofuji, A. M. de Oliveira, C. R. P. Dionisio, and S. T. Kofuji, "Simulation and manufacturing of a miniaturized exponential

UWB TEM horn antenna for UWB radar applications," *Journal of Microwaves, Optoelectronics and Electromagnetic Applications*, vol. 12, no. 2, pp. 655–665, Dec 2013.

[37] K. Chung, S. Pyun, and J. Choi, "The design of a wideband TEM horn antenna with a microstrip-type balun," *IEEE Antennas and Propagation Society Symposium*, vol. 2, pp. 1899–1902.

[38] F. Karshenas, A. R. Mallahzadeh, and A. Imani, "Modified TEM horn antenna for wideband applications," *2009 13th International Symposium on Antenna Technology and Applied Electromagnetics and the Canadian Radio Science Meeting*, pp. 1–5, Feb 2009.

[39] C. A. Balanis, *Advanced engineering electromagnetics*, 2nd ed. John Wiley & Sons, 2012.

[40] J. C. Koech, P. G. Wiid, and D. I. de Villiers, "Hyperband Antenna Design for RFI Testing," in *2019 International Conference on Electromagnetics in Advanced Applications (ICEAA)*. IEEE, Sep 2019, pp. 0280–0285.

[41] "IEEE recommended practice for near-field antenna measurements," *IEEE Antennas and Propagation Society/IEEE Std 1720-2012*, 2012.

[42] T. S. Chu and R. A. Semplak, "Gain of Electromagnetic Horns," *Bell System Technical Journal*, vol. 44, no. 3, pp. 527–537, Mar 1965.

[43] K. HARIMA, "Numerical simulation of far-field gain determination at reduced distances using phase center," *IEICE Transactions on Communications*, vol. E97.B, no. 10, pp. 2001–2010, 2014.

[44] H. Shakhtour, R. Cornelius, and D. Heberling, "Three antenna gain determination method in compact antenna test ranges," *2013 Loughborough Antennas & Propagation Conference (LAPC)*, pp. 392–396, Nov 2013.

[45] "IEEE standard test procedures for antennas," *ANSI/IEEE Std 149-1979*, 1979.

[46] L. Hemming and R. Heaton, "Antenna gain calibration on a ground reflection range," *IEEE Transactions on Antennas and Propagation*, vol. 21, no. 4, pp. 532–538, Jul 1973.

[47] T. Julies and P. Wiid, "Time-domain antenna characterization," B.S. Thesis, Stellenbosch University, 2018.

[48] B. R. Mahafza, *Radar systems analysis and design using MATLAB*, 3rd ed. CRC Press, 2013.

[49] E. Muehldorf, "The phase center of horn antennas," *IEEE Transactions on Antennas and Propagation*, vol. 18, no. 6, pp. 753–760, Nov 1970.

[50] "SUrrogate MOdeling (SUMO) Matlab Toolbox." [Online]. Available: http://www.sumo.intec.ugent.be/SUMO

[51] A. I. J. Forrester, S. Andras, and A. J. Keane, *Engineering design via surrogate modelling: a practical guide*. Chichester, UK: John Wiley & Sons, Ltd, Jul 2008.

[52] I. Couckuyt, F. Declercq, T. Dhaene, H. Rogier, and L. Knockaert, "Surrogate-based infill optimization applied to electromagnetic problems," *International Journal of RF and Microwave Computer-Aided Engineering*, vol. 20, no. 5, pp. 492–501, Sep 2010.

[53] D. R. Jones, M. Schonlau, and W. J. Welch, "Efficient global optimization of expensive black-box functions," *Journal of Global Optimization*, vol. 13, no. 4, pp. 455–492, 1998.

[54] Katsushige Harima, "Determination of gain for EMC antennas using phase center," *Journal of the National Institute of Information and Communication Technology*, vol. 63, no. 1, pp. 117–125, 2016.